Assessment of Small Unmanned Aircraft Systems for Pavement Inspections

May 2023

Final Report

U.S. Department of Transportation
Federal Aviation Administration

NOTICE

This document is disseminated under the sponsorship of the U.S. Department of Transportation in the interest of information exchange. The United States Government assumes no liability for the contents or use thereof. The United States Government does not endorse products or manufacturers. Trade or manufacturer's names appear herein solely because they are considered essential to the objective of this report. The findings and conclusions in this report are those of the author(s) and do not necessarily represent the views of the funding agency. This document does not constitute FAA policy. Consult the FAA sponsoring organization listed on the Technical Documentation page as to its use.

This report is available at the Federal Aviation Administration William J. Hughes Technical Center's Full-Text Technical Reports page: actlibrary.tc.faa.gov in Adobe Acrobat portable document format (PDF).

1. Report No. DOT/FAA/TC-23/39	2. Government Accession No.	3. Recipient's Catalog No.
4. Title and Subtitle ASSESSMENT OF SMALL UNMANNED AIRCRAFT SYSTEMS FOR PAVEMENT INSPECTIONS		5. Report Date May 2023
		6. Performing Organization Code
7. Author(s) Drishti Valecha*, David Hall*, Ethan Schreuder*, Sheldon Menezes*, Aaron Lawrence*, and Russell Knieriem**		8. Performing Organization Report No. DOT/FAA/TC-23/39
9. Performing Organization Name and Address Woolpert, Inc* 600 Aviation Research Boulevard Egg Harbor Township, NJ 08234 Applied Research Associates** 2628 Fire Road, Egg Harbor Township, NJ 08234		10. Work Unit No. (TRAIS)
		11. Contract or Grant No. 692M15-20-T-00034
12. Sponsoring Agency Name and Address Department of Transportation Federal Aviation Administration Office of Airports Safety and Standards 800 Independence Avenue S.W. Washington, DC 20591		13. Type of Report and Period Covered Final Report
		14. Sponsoring Agency Code AAS-100
15. Supplementary Notes The FAA Airport Technology Research and Development Branch Contracting Officer Representative (COR) is Matthew Brynick.		

16. Abstract

Pavement inspections play an integral role in ensuring airport safety. The FAA Airport Technology Research and Development (ATR) branch performed research to assess the integration of small Unmanned Aircraft Systems (sUAS) into an airport's Pavement Management Program (PMP). To conduct sUAS-based pavement inspections, the research team tested across five different airports between 2020 and 2022. The objective was to provide a repeatable set of processes and procedures for data collection, analysis, and reporting for sUAS-based pavement inspections. This report presents sUAS data collection parameters, data processing techniques, and data analysis, as well as workflows associated with each inspection. A summary of distresses identifiable via sUAS is also provided.

17. Key Words small Unmanned Aircraft System (sUAS), Pavement inspections	18. Distribution Statement This document is available to the U.S. public through the National Technical Information Service (NTIS), Springfield, Virginia 22161. This document is also available from the Federal Aviation Administration William J. Hughes Technical Center at actlibrary.tc.faa.gov.		
19. Security Classif. (of this report) Unclassified	20. Security Classif. (of this page) Unclassified	21. No. of Pages 187	22. Price

Form DOT F 1700.7 (8-72)   Reproduction of completed page authorized

TABLE OF CONTENTS

LIST OF FIGURES

LIST OF TABLES

LIST OF ACRONYMS

3D	Three-dimensional
AAC	Asphalt overlay over asphalt concrete
AASHTO	American Association of State Highway and Transportation Officials
AC	Asphalt concrete
AEI	Architectural Engineering Institute
AGL	Above ground level
AI	Artificial Intelligence
ANSI	American National Standards Institute
APC	Asphalt overlay over Portland cement concrete
ARA	Applied Research Associates
ASCE	American Society of Civil Engineers
ASPRS	American Society for Photogrammetry and Remote Sensing
ASR	Alkali-silica reactions
ASTM	American Society for Testing and Materials
AT	Aerial Triangulation
ATRD	Airport Technology Research and Development
AUVSI	Association for Unmanned Vehicle Systems International
BET	Best estimate of trajectory
CFR	Code of Federal Regulations
CI	Construction Institute
CVG	Cincinnati / Northern Kentucky International Airport
DEM	Digital Elevation Model
DOT	Department of Transportation
DRBA	Delaware River and Bay Authority
DSLR	Digital Single-Lens Reflex
DSV	Digital Survey Vehicle
FAA	Federal Aviation Administration
FHWA	Federal Highway Administration
FOD	Foreign object debris
FOG	Foot-on-ground
GA	General aviation
GCP	Ground control point
G-I	Geo-Institute
GIS	Geographical Information Systems
GNSS	Global Navigation Satellite System
GPR	Ground-penetrating radar
GSD	Ground sampling distance
HAMR™	Hybrid Advanced Multi-Rotor
ICC	International Cybernetics Connect
IMU	Inertial measurement unit
L&T	Longitudinal and transverse
LCMS	Laser crack measurement system
LiDAR	Light detection and ranging
M&R	Maintenance and rehabilitation
MOA	Memorandum of Agreement

MSL	Minimum service level
NDVI	Normalized Difference Vegetation Index
NHDOT	New Hampshire Department of Transportation
NIOSH	National Institute of Occupational Safety and Health
NN	Neural networks
ONZ	Grosse Ile Municipal Airport
PCC	Portland cement concrete
PCI	Pavement Condition Index
PMP	Pavement Management Program
PPK	Post-processing kinematic
QA	Quality assurance
QC	Quality control
RAM	Random-access memory
RGB	Red, green, blue
RTK	Real-time kinematic
SAV	Savannah/Hilton-Head International Airport
SBET	Smooth Best Estimated Trajectory
SME	Subject matter expert
sUA	Small unmanned aircraft
sUAS	Small Unmanned Aircraft System
SWOT	Strengths, weaknesses, opportunities, and threats
T&DI	Transportation and Development Institute
TTF	Custer Airport
UESI	Utility Engineering and Surveying Institute
USRD	Unmanned Systems and Robotics Database
VRS	Virtual reference station
VTOL	Vertical takeoff and landing
WWD	Cape May County Airport

TERMINOLOGY

Aerial Triangulation. Aerial Triangulation software packages determine the corrected exterior orientation of each image so they can be compiled into a well-ordered and controlled set. The exterior orientation of an image refers to its position and orientation related to an exterior coordinate system.

Airframe. The airlifting component of a small Unmanned Aircraft System (sUAS); does not include the sensor.

Asphalt Concrete. Aggregate mixture with an asphalt cement binder.

Capture Area. A buffered area around the intended test area in which the sUAS captures imagery.

Distress Severity Levels. Pavement distresses are most commonly categorized as high, medium, or low severity, depending on the extent and/or depth of the damage.

Ground Control Points. Specific, identifiable points on the ground that are used as reference points for creating or verifying mapping or surveying data.

Ground Sampling Distance. The distance, as measured along the ground, between adjacent pixels in an image. Ground sampling distance (GSD) governs how much information can be inferred about features from image measurements. With smaller GSDs, finer features are able to be resolved. The GSD and image resolution determine the footprint size of the image captured by the sensor. GSD represents the ideal mathematical distance on the ground as measured between pixels and as such might not always describe the smallest visible feature.

High-Severity Distress. High-severity pavement distress refers to when the pavement is in very poor condition and needs to be repaired or replaced as soon as possible. High-severity distresses are typically characterized by large areas of total or near-total surface disintegration, severe rutting, and extensive cracking that can lead to safety hazards for aircraft and increase the likelihood of pavement failure.

Low-Severity Distress. Low-severity pavement distress can be defined as surface irregularities and imperfections that are not considered critical to the pavement's overall structural integrity. These defects can include cracks, potholes, and raveling, and typically occur in areas with low traffic volume or weight. While they might not pose an immediate safety threat, they can impact the function and appearance of the pavement and should be corrected as soon as possible.

Medium-Severity Distress. Medium-severity pavement distress refers to a level of damage significant enough to require corrective action but not so severe that the pavement cannot be used safely. These defects can be caused by a number of factors, such as wear and tear from aircraft traffic or weather conditions. Treatment for medium-severity airport pavement distress can vary depending on the specific cause but might involve patching or resurfacing the affected area.

Orthoimagery. A form of remotely sensed imagery that has been orthorectified.

Orthomosaic. A digital image composed of individual photos of a scene or surface that have been stitched together through orthorectification. An orthomosaic contains distance measurements that are consistent across the entire image. This imagery is commonly used in mapping and surveying applications.

Overlap. Forward overlap is the amount of coverage between consecutive images along the same flight line, as measured in percentages. Side overlap is the amount of coverage between images in adjacent flight lines, as measured in percentage.

Pavement Condition Index. A numerical rating of pavement condition ranging from 0 to 100, with 0 being the worst possible condition and 100 being the best possible condition.

Pavement Distress. External indicators of pavement deterioration caused by loading, environmental factors, construction deficiencies, or a combination thereof.

Portland Cement Concrete. Aggregate mixture with Portland cement binder, including nonreinforced and reinforced jointed pavement.

Random Sample. A sample unit of the pavement section selected for inspection by random sampling techniques, such as a random number table or systematic random procedure.

Sample Unit. A subdivision of a pavement section that has a standard size range: 20 contiguous slabs for PCC airfield pavement and 5,000 contiguous square feet for AC airfield pavement and porous friction surfaces.

Sensor. A light-sensitive chip that records an image as a pattern of tiny squares, called pixels. The more photosites a sensor has, the higher the resolution of the image will be.

Small Unmanned Aircraft System. A small, unmanned aircraft and its associated elements (including attachments, communication links, and the components that control the small, unmanned aircraft) that are required for the safe and efficient operation of the small, unmanned aircraft in the national airspace system.

Spatial Alignment. The process of ensuring that all aspects of an image are in proper alignment with one another.

Spatial Resolution/Resolving Power. Like GSD, resolving power describes the amount of detail visible in an image. The higher the resolving power of an image, the more accurately it can reproduce the details of the original scene. The amount of detail actually resolved is influenced by the size of the image sensor, the quality of the lens, and the digital processing capabilities of the camera. The relationship between the resolving power and GSD is inverse; an image with a small GSD (each pixel represents a small area) is said to have a high spatial resolution.

Test Area. The intended area for pavement distress analysis.

Units of conversion. GSD values can be represented in millimeters (mm), centimeters (cm), or inches (in.). GSD values and the ability to see finer details in an image are inversely proportional, i.e., a 2-mm GSD will reveal finer details in an image than a 25.4-mm GSD. GSD values can be represented as follows:

GSD (mm)	GSD (cm)	GSD (in.)
2	0.20	0.08
3	0.30	0.12
4	0.40	0.16
4.9	0.49	0.19
7.9	0.79	0.311
8.0	0.80	0.315
10.8	1.08	0.43
13.7	1.37	0.54
25.4	2.54	1.00

EXECUTIVE SUMMARY

Recognizing the challenges and limitations of traditional methods for pavement condition inspections, the Federal Aviation Administration (FAA) Airport Technology Research and Development (ATR) branch performed research to assess the integration of small Unmanned Aircraft Systems (sUAS) into an airport's Pavement Management Program (PMP). The two overarching objectives of this research effort were to (1) develop a repeatable set of processes and procedures for data collection, analysis, and reporting; and (2) disseminate technical performance specifications of sUAS acceptable for use when conducting PMP inspections.

This research effort kicked off with a thorough assessment of relevant literature from academic, military, and industry sources followed by a strengths, weaknesses, opportunities, and threats (SWOT) analysis of existing airframes and sensors to set a baseline for the first phase of data collection. The analysis indicated that the multirotor sUAS was cost-efficient, presented improved imaging capabilities, and has the ability to fly low and slow to collect high-resolution imagery.

Phase 1 testing was executed at the Cape May County Airport (WWD) with successful data collection from 78 flights. The analysis of all processed orthoimagery revealed that 2-mm ground sampling distance (GSD) from a DJI M210 RTK v2 and X7-35mm sensor is effective in identifying a wide range of pavement distresses. The resulting Pavement Condition Index (PCI) from sUAS was in line with foot-on-ground (FOG) and digital survey vehicle (DSV) inspections; however, utilizing higher imagery overlaps for this phase resulted in longer data collection times for the sUAS. Further research was required to limit the imagery overlap, while maintaining data quality, to make sUAS data collection operationally feasible.

The recommendations and best practices established in Phase 1 were taken into consideration prior to Phase 2 testing. Phase 2 testing was executed at WWD, Savannah/Hilton Head International Airport (SAV), Cincinnati/Northern Kentucky International Airport (CVG), Grosse Ile Municipal Airport (ONZ), and Custer Airport (TTF) to perform several tests, such as increasing operational efficiency and testing new systems. The subject matter expert's (SME) reviews and analyses of orthoimagery in Phase 2 indicated that a minimum of 2-mm ground sampling distance (GSD) (or smaller) and overlap settings of 40/40 were required to evaluate PCI values using sUAS. The 2-mm GSD imagery at 40/40 overlap provided the maximum operational efficiency without compromising the data quality. The research team identified that multirotor systems were better suited for data collection, sUAS data collection was of better quality and resolution than that of the DSV-derived data, and processed imagery without surveyed ground control indicated negligible geographical shift with no impact on identifying and analyzing the pavement distresses.

Final validation data collection and analysis were performed on a full scale at WWD, including PCI surveys of Runway 10/28 and the airport's two primary aprons. Inspections were executed per ASTM D5340 and represent real-life application of PCI inspections for the use of managing airport pavements. Final products resulted in a geodatabase with 2-mm orthomosaic imagery with digitized pavement distresses as well as a PAVER pavement management database. This database can be directly imported into the FAA's PAVEAIR software for combined analysis with future data sets.

Analysis concluded that, while further research is required for detection of some vertical distresses, most asphalt concrete (AC) and Portland cement concrete (PCC) distresses can be identified, qualified, and quantified at a higher level of accuracy than what is traditionally completed during FOG inspections. This results in overall pavement conditions typically receiving lower PCI scores based on sUAS data collection as compared to FOG inspections.

1. INTRODUCTION

Airport pavements deteriorate continually due to aircraft loading and environmental exposure. This deterioration results in pavement distresses (e.g., longitudinal and transverse (L&T) cracking, rutting, increased roughness, potholes, weathering, raveling) that impact the serviceability of the pavement. The Federal Aviation Administration (FAA) recognizes that approximately 70% of its Airport Improvement Program (AIP) budgets are invested into maintaining airfield pavements. Currently, airfield pavement inspections are performed using one of two methods:

- **Foot-on-ground (FOG).** FOG inspections require inspectors to walk the pavement area and collect detailed distress data. These data include recording the type, severity, and quantity of distresses in the field, with manual geo-tagging of each.

- **Digital survey vehicle (DSV).** DSV inspections require inspectors to drive over the paved area and collect distress data. The DSV collects downward-facing video, photographs, and other data while traveling at speeds up to 60 miles per hour. Collected data are processed and developed into pavement inspection surveys.

These survey methods are subjective, time-consuming, risky, labor-intensive, and expensive, limiting the number of surveys an airport can conduct. Limitations are encountered when surveying sections such as fillets and small taxiways, or near elevated light fixtures. Spatial alignment also presents an issue for the DSV, as it is difficult to maintain passes that merge seamlessly to map the entire inspection area.

In recent years, airport stakeholders have experimented with using small Unmanned Aircraft Systems (sUAS) for pavement condition assessment. Use of sUAS has the potential to aid airport operators in conducting frequent inspections through increased time efficiency, improved cost-effectiveness, and increased safety for inspection personnel. Recognizing the challenges and limitations of traditional methods for pavement inspections, the FAA Airport Technology Research and Development (ATR) branch performed research on integration of sUAS into Pavement Management Program (PMP) inspections.

1.1 RESEARCH PURPOSE

The purpose of this research was to develop and recommend best practices and performance-based technical specifications for using sUAS to collect pavement data to supplement airport PMP inspections.

1.2 RESEARCH OBJECTIVES

The two overarching objectives of this research effort were to:

- develop a repeatable set of processes and procedures for data collection, analysis, and reporting.

- disseminate technical specifications for acceptable use of sUAS to conduct PMP inspections in an airport environment.

1.3 RESEARCH APPROACH

This research effort was executed using a five-step approach, breaking the data collection efforts down in three phases; Phase 1 and Phase 2 testing followed by Validation Testing. The research approach was as follows:

- Perform a comprehensive literature review and strengths, weaknesses, opportunities, and threats (SWOT) analysis of the technology to identify baseline parameters for initial testing of sUAS for pavement inspections.

- Plan, conduct, analyze, and document the operational tests for Phase 1 testing with multiple sUAS technologies at Cape May County Airport (WWD).

- Initiate Phase 2 testing with additional sUAS technologies, validate and refine Phase 1 testing parameters, and conduct testing at three additional airports with distinct pavement distresses and environmental conditions.

- Perform Validation Testing.

- Develop a final compilation of research, including a performance-based technical specifications report.

Figure 1 illustrates the research approach process.

| Literature Review and SWOT Analysis | Airport Test Procedures And Results – Phase 1 | Airport Test Procedures And Results – Phase 2 | Validation Testing | Research Findings and Performance Specifications |

Figure 1. Research Approach

1.4 APPLICABLE STANDARDS

Applicable standards for task-specific items were followed and are summarized in Table 1.

Table 1. Applicable Standards

Task	Applicable Standards/Regulations
Literature Review	N/A
Phase 1, Phase 2, and Validation Testing	
Site Selection	N/A
FOG Surveys	ASTM D5340-20—*Standard Test Method for Airport Pavement Condition Index Surveys*, FAA Advisory Circular 150/5380-7B—*Airport Pavement Management Program*
DSV Surveys	ASTM D5340-20—*Standard Test Method for Airport Pavement Condition Index Surveys*
sUAS Survey and Inspection	Airport Specific Certificate of Authorization, 14 CFR Part 107—Small Unmanned Aircraft Systems; ASTM D5340-20—*Standard Test Method for Airport Pavement Condition Index Surveys*
Analysis and Technical Brief	N/A

1.5 REPORT ORGANIZATION

Section 1 provides a high-level overview of the research background and methodology.

Section 2 summarizes the literature review along with relevant government and industry reference standards. An in-depth literature review is included in Appendix A.

Section 3 delivers an overview of sUAS technology available at the time the literature review was performed, along with a SWOT analysis that demonstrates its implementation capabilities and limitations for use in pavement inspections.

Section 4 discusses airport test procedures and results from Phase 1. This section details the research team's workflow, initial sUAS testing parameters, and evaluation of pavement imagery followed by recommendations for Phase 2.

Section 5 builds upon the findings from Phase 1 and discusses airport test procedures and results from Phase 2. This section introduces additional sUAS testing parameters while increasing operational efficiency in data collection workflow.

Section 6 validates the key findings from Phase 1 and Phase 2 and discusses full-scale Validation Testing with a different sUAS. A cost-benefit analysis between FOG and sUAS follows.

Section 7 highlights key conclusions and recommendations for further research.

2. LITERATURE REVIEW

Airport pavements require continual routine maintenance, rehabilitation, and upgrade, and the most effective means of preserving airside pavements is to implement a comprehensive PMP. The PMP should be updated routinely, and airports should make repairs and take preventive

measures to optimize pavement performance. Different agencies use different methods to collect, process, and report the data to be used in PMPs. Some agencies collect data in-house, while others hire consultants for FOG and/or DSV collection. Distress analysis is performed using manual, semi-automated, or fully automated methods. This has resulted in miscellaneous formats for data collection and development of proprietary software programs for data processing. Regarding airfield pavements, although the method to be used for condition surveys is not mandated by the FAA, the Advisory Circulars 150/5380-6C, *Guidelines and Procedures for Maintenance of Airport Pavements* and 150/5380-7B, *Airport Pavement Management Program* (FAA, 2014a and 2014b) recommend following the procedures documented in ASTM D5340 (ASTM International, 2020)*, Standard Test Method for Airport Pavement Condition Index Surveys*.

The American Society for Testing and Materials (ASTM) distress codes provide classification of pavement distresses, and each code corresponds to a specific type of distress. The distresses are categorized as high (H), medium (M), or low (L) severity, depending on the extent and/or depth of the damage. Table 2 lists distresses commonly found at airfields along with their respective codes.

Table 2. The ASTM Distress Codes

ASTM AC Distresses			ASTM PCC Distresses		
Distress Code	Distress Description	Severities	Distress Code	Distress Description	Severities
41	Alligator Cracking	L, M, & H	61	Blowup	L, M, & H
42	Bleeding	N/A	62	Corner Break	L, M, & H
43	Block Cracking	L, M, & H	63	Linear Crack	L, M, & H
44	Corrugation	L, M, & H	64	Durability Cracking	L, M, & H
45	Depression	L, M, & H	65	Joint Seal Damage	L, M, & H
46	Jet Blast	N/A	66	Small Patch	L, M, & H
47	Joint Reflection Crack	L, M, & H	67	Large Patch	L, M, & H
48	L&T Crack	L, M, & H	68	Pop-outs	N/A
49	Oil Spillage	N/A	69	Pumping	N/A
50	Patching	L, M, & H	70	Scaling	L, M, & H
51	Polished Aggregate	N/A	71	Faulting	L, M, & H
52	Raveling	L, M, & H	72	Shattered Slab	L, M, & H
53	Rutting	L, M, & H	73	Shrinkage Crack	N/A
54	Shoving	L, M, & H	74	Joint Spall	L, M, & H
55	Slippage Crack	L, M, & H	75	Corner Spall	L, M, & H
56	Swelling	L, M, & H	76	ASR	L, M, & H
57	Weathering	L, M, & H			

N/A = Not applicable
ASR = Alkali-silica reaction

The Pavement Condition Index (PCI) is a measure of the pavement condition that is used to help prioritize maintenance and rehabilitation needs. A PCI value is calculated by determining distress according to type, severity, and quantity, and ranges from 0 to 100, with 100 representing a new pavement and 0 representing a failed pavement. These rating scales are illustrated in Figure 2.

Figure 2. The PCI Rating Scale (ASTM International, 2020)

A gradient color scheme, as shown in Figure 3, was applied to each PCI summary table in Section 4 and Section 5 to further visualize where on the scale each sample unit was rated.

Figure 3. Color Scheme Applied to PCI Rating

In recent years, there have been efforts to use sUAS for pavement condition assessments. However, guidance on minimum technical specifications, such as airframe type, sensor type and capability, flight parameters, and safety and coordination with air traffic, are yet to be established. This section explores key pieces of organizational reference standards and literature on sUAS-based pavement inspections with the aim of establishing interim guidance for Phase 1 testing. Following the reference standards, key findings from the literature review are summarized. A detailed literature review is included in Appendix A.

2.1 REFERENCE STANDARDS

This section summarizes the identified reference standards specifically related to pavement management and sUAS operations.

2.1.1 The FAA Reference Standards

The FAA reference standards presented in Table 3 were applicable at the time this research was performed. The research team adhered to these standards to determine the baseline guidance as it pertains to airport pavement inspections.

Table 3. The FAA Reference Standards

FAA Advisory Circular	Reference
150/5200-18C	*Airport Safety Self Inspection*
150/5380-6C	*Guidelines and Procedures for Maintenance of Airport Pavements*
150/5380-7B	*Airport Pavement Management Program*

2.1.2 Professional/Industry Organizational Standards

The research team performed a thorough review of case studies, minimum standards, and best practices that have been developed by professional organizations that are related to remote sensing, sUAS operations, airport operations, and pavement management. The following are examples of professional organizations that the research team took into consideration.

2.1.2.1 American Society for Photogrammetry and Remote Sensing

The American Society for Photogrammetry and Remote Sensing (ASPRS) is an organization that promotes photogrammetry and remote sensing with divisions in Geographical Information Systems (GIS), Light Detection and Ranging (LiDAR), photogrammetric applications, primary data acquisition, professional practice, remote sensing applications, and sUAS. The sUAS division serves as a resource for mapping standards and industry insights. Table 4 presents these standards.

Table 4. The ASPRS Reference Standard

Document Number	Reference
Edition 1, Version 1.0, November 2014	*ASPRS Positional Accuracy Standards for Digital Geospatial Data*

2.1.2.2 American Society for Testing and Materials

ASTM is a globally recognized leader that develops and publishes technical standards for businesses, services, and other organizations. ASTM has issued multiple standards for terminology, definitions, and data collection techniques applicable to airfield, highway, road, and parking lot classifications. ASTM standards have also been adopted at federal and state levels. These standards are used to improve product quality, enhance health and safety, strengthen market access and trade, and build consumer confidence. Table 5 presents the applicable standards published by ASTM.

Table 5. The ASTM Reference Standards

Document Number	Reference
ASTM D5340-20 (2020)	*Standard Test Method for Airport Pavement Condition Index Surveys*
ASTM D6433-20	*Standard Practice for Roads and Parking Lots Pavement Condition Index Surveys*
ASTM E1778-98a	*Standard Terminology Relating to Pavement Distress*
ASTM E1777-09	*Standard Guide for Prioritization of Data Needs for Pavement Management*
ASTM WK29844	*New Guide for Classifying and Measuring Pavement Cracking from the Image Collected by Automated Pavement Condition Survey Equipment*
ASTM WK32849	*Standard Guide for Classification of Automated Pavement Condition Survey Equipment*

2.1.2.3 Association for Unmanned Vehicle Systems International

The Association for Unmanned Vehicle Systems International (AUVSI) is the world's largest non-profit organization that is dedicated to the advancement of unmanned systems and robotics. AUVSI represents corporations and professionals from more than 60 countries involved in industry, government, and academia. AUVSI maintains an Unmanned Systems and Robotics Database (USRD) that is the largest comprehensive and searchable database for all vehicles operating in civil, commercial, and military markets. This database was considered to assist with any sUAS performance or dimensional data needed in this research effort.

2.1.2.4 Federal Highway Administration

The Federal Highway Administration (FHWA) is an agency tasked with supporting state and local governments for the maintenance, construction, and design of the interstate highway system and federal and tribal-owned lands. FHWA acknowledges that the benefits of sUAS are wide-ranging and impact nearly all aspects of highway transportation, including FOG inspections, increased accuracy, quicker and more efficient data collection, and access to hard-to-reach locations. sUAS use is expanding across the state Departments of Transportation (DOTs), and the numbers of sUAS applications are increasing steadily. A 2019 survey by the American Association of State Highway and Transportation Officials (AASHTO) found that 36 states are already using high-definition cameras, LiDAR, and other sensors to enhance construction inspection, bridge inspection, and incident response operations (AASHTO, 2019). While state DOTs have used sUAS technology for survey and data mapping, no formal standard has been developed for either use case. However, FHWA shares best practices and technical guidance under Technical Briefs that are available to the public via online sources, such as the FHWA website. Table 6 presents the FHWA standards applicable to this research.

Table 6. The FHWA Publication Standards

FHWA Report Number	Publication
FHWA-HIF-11-11	*The Pavement Management Roadmap*
T5040.38	*Pavement Friction Management*
FHWA-PROJ-12-0016	*Pavement Structural Evaluation at the Network Level*
FHWA-RC-20-004 2020	*Calibration, Certification, and Verification of Transverse Pavement Profile Measurements*
FHWA-HIF-20-085 2020	*Interstate Highway Pavement Sampling Final Phase 2 Report*
November 2017	*Developing Transportation Asset Management Financial Plans*
June 2018	*Guidelines for Development and Approval of State Data Quality Management Programs*
FHWA -2013-0053	*National Performance Management Measures; Assessing Pavement Condition for the National Highway Performance Program and Bridge Condition for the National Highway Performance Program*
FHWA-HRT-13-092	*Distress Identification Manual for the Long-Term Pavement Performance Program*
HIF-11-026	*Local Calibration of the MEPDG Using Pavement Management Systems*
Tech Brief	*Use of sUAS for Land Survey*
Tech Brief	*Use of sUAS for Construction Inspection*
Tech Brief	*Use of sUAS for Bridge Inspection*
Tech Brief	*Use of sUAS for Emergency Management of Flooding*

2.1.2.5 American Association of State Highway and Transportation Officials

AASHTO establishes guidelines for highway design and construction throughout the United States. A 2018 survey by AASHTO found that, of the 50 states, 20 use sUAS in their day-to-day business (AASHTO, 2018). Historically, there has been a lack of uniformity in collecting surface distress imagery data. However, there have been efforts in recent years to standardize definitions of distress types and severities, and measurement procedures. Table 7 provides the standards developed by AASHTO and adopted by multiple agencies around the country.

Table 7. The AASHTO Publication Standards

Standard	Reference
AASHTO R55	*Quantifying Cracks in Asphalt Pavement Surfaces*
AASHTO PP67	*Standard Practice for Quantifying Cracks in Asphalt Pavement Surfaces from Collected Pavement Images Utilizing Automated Methods*
AASHTO PP68	*Collecting Images of Pavement Surfaces for Distress Detection*
AASHTO PP70	*Collecting the Transverse Pavement Profile*

Standard	Reference
AASHTO R48	*Determining Rut Depth in Pavements*
AASHTO R36	*Standard Practice for Evaluating Faulting of Concrete Pavements*

2.1.2.6 American Society of Civil Engineers

The American Society of Civil Engineers (ASCE) works towards the advancement of civil engineering and enhancement of human welfare. ASCE serves professionals within specified fields of civil engineering that include, but are not limited to, the Architectural Engineering Institute (AEI), Geo-Institute (G-I), Construction Institute (CI), Utility Engineering and Surveying Institute (UESI), and Transportation and Development Institute (T&DI). Table 8 presents documentation found in the ASCE library applicable to this research effort.

Table 8. Applicable ASCE Documentation

Source	Reference
ASCE Library	*Pavement Surface Permanent Deformation Detection and Assessment Based on Digital Aerial Triangulation*

2.1.2.7 American National Standards Institute

The American National Standards Institute (ANSI) facilitates uniform solutions and standards and conformity assessment activities in the United States. ANSI encompasses every industry and has the mission of facilitating the development of American National Standards by accrediting the procedures of standards-developing organizations and approving their documents. Table 9 presents the documentation published by ANSI related to this research effort.

Table 9. Applicable ANSI Documentation

Source	Reference
ANSI Unmanned Aircraft Systems Standardization Collective, June 2020	*Standardization Roadmap for Unmanned Aircraft Systems*, Version 2.0

2.1.3 Small Unmanned Aircraft System Operational Reference Standards

The 14 Code of Federal Regulations (CFR), Part 107 outlines regulations for the operation of sUAS or drones. These regulations include requirements for registration and pilot certification and limitations for aircraft operations. The purpose of these regulations is to ensure the safety of both crewed and unmanned aircraft operators and the general public. Table 10 presents the applicable regulations at the time of this research.

Table 10. Applicable sUAS Reference Standards

Standard	Reference
14 CFR Part 107	*Small Unmanned Aircraft Systems*
14 CFR Part 77	*Safe, Efficient Use and Preservation of the Navigable Airspace*
Advisory Circular 107-2	*Small Unmanned Aircraft Systems (sUAS)*

2.2 LITERATURE REVIEW SUMMARY

An extensive industry and academia literature review identified that, although a standardized methodology does not exist, sUAS technologies have been successfully used in various applications related to pavement, roadways, railroads, bridges, construction, monitoring, and inspection. Table 11 demonstrates the following key findings, which were taken into consideration when planning for Phase 1 testing.

Table 11. Overall Findings from Literature Review

	Using multirotor systems for data collection led to improved imaging capabilities and cost efficiency.
	The spatial resolution appeared to be the most important factor in analyzing data for use in PMP inspections. It was identified that testing should initiate with a minimum altitude of 50 feet (ft) above the ground, then increase gradually to ascertain a ceiling for best practices.
	Point clouds generated from a sUAS-based LiDAR system or stereo-matching photogrammetry is effective in identifying vertical pavement distresses.
	Thermal infrared imagery could provide insight on pavement deterioration and condition.
	While thermal and multispectral sensors exist for fixed-wing sUAS, the minimum safe flying height would yield resolutions that are too low for usable data.
	Manufacturer limitations for the thermal sensor on fixed-wing sUAS prevent flight plans from being developed based on the sensor specifications. (The eBee thermal camera is combined with a color camera into a single sensor package, however, the flight planning is only based on color camera.)
	The ability to fly low and slow was deemed critical in successful acquisition of high-resolution imagery. Operating a fixed-wing in a low-altitude airport environment has the potential for extremely high risks and could deem fixed-wing operations unrealistic for this application.

3. TECHNOLOGY REVIEW

The research team tested and evaluated a variety of airframes and sensors as part of this research effort. The study of small, unmanned aircraft (sUA) airframes and sensors investigated the repeatability and integration of the technology under diverse climatic and geographic conditions for both asphalt concrete (AC) and Portland cement concrete (PCC) pavements.

3.1 AIRFRAME TYPES FOR sUA

Multirotor: Multirotor, also known as rotary-wing, platforms are equipped with lift-generating rotors to achieve vertical takeoff and landing (VTOL) capabilities and to sustain flight. In principle, multirotor platforms operate like helicopters. These platforms can have a single, multiple, coaxial, or even tiltrotor configuration with capabilities to hover, and are commonly operated in smaller areas.

Fixed-wing: Fixed-wing sUASs resemble more traditional-looking aircraft made up of a central body, two wings, and a propulsion source. Fixed-wing platforms can have a variety of wing shape layouts, such as rectangular, tapered, or rounded straight-wing configurations; high-, medium-, or low-swept wing configurations; and delta wing configurations. Typically, these platforms can sustain long flight times and carry heavy payloads.

Hybrid: Hybrid sUASs offer the advantages of both multirotor and fixed-wing airframe operational characteristics. These systems typically use a lift-generating rotor to achieve VTOL and have fixed wings to sustain flight.

Each type of sUA airframe can have a variety of sensors, and each has unique capabilities and limitations. Some key attributes to consider when selecting an airframe are as follows:

- Aircraft navigation
- Geotagging accuracy
- Operational endurance
- Speed
- Situational awareness
- Sensor integration and capabilities

A detailed guide on airframe performance specifications and attributes can be found in *Performance Report for sUAS Based Pavement Inspections* (Woolpert, Inc., 2023), which offers direction on selecting the appropriate airframe.

3.2 SENSOR TYPES FOR sUA

Red, Green, Blue (RGB): RGB imagery captures specific bands of light in the visible spectrum (red, green, and blue) and converts them to a color image replicating standard human vision.

LiDAR: Topographic LiDAR sensors use a near-infrared laser to measure distance and generate precise, three-dimensional (3D) information about the terrain and its surface characteristics by developing a point cloud data set.

Thermal: A thermographic sensor creates an image that depicts temperature differences by collecting and analyzing long-wave and medium-wave wavelengths of infrared radiation.

Hyperspectral: Hyperspectral sensors are capable of collecting a continuous portion of the electromagnetic spectrum which can be converted into pixels and can be viewed in various band combinations as an image.

GPR: Ground-penetrating radar (GPR) sensors use a non-intrusive method of emitting radar pulses to develop an image of the sub surface condition.

Airframes can be equipped with sensors that collect a variety of data types, and the characteristics of the sensor can affect the quality of the data collected. Physically larger sensors can deliver higher dynamic range but offer shallower depth of field than smaller sensors, while higher resolutions can provide increased detail and clarity to captured images. The key attributes to consider when selecting a sensor are as follows:

- Camera system characteristics
- Shutter type
- Focus
- Metering mode
- Exposure modes
- Mounting
- Gimbal

A detailed guide on sensor performance specifications and attributes can be found in *Performance Report for sUAS Based Pavement Inspections* (Woolpert, Inc., 2023), which offers direction on selecting the appropriate sensor for desired results.

3.3 STRENGTHS, WEAKNESSES, OPPORTUNITIES, AND THREATS ANALYSIS

The research team developed recommendations for the most viable sUAS solutions that support and meet both operational and technical requirements. These recommendations were determined by analyzing the SWOT of different types of sUAS.

3.3.1 Small Unmanned Aircraft Airframes SWOT Analysis

Table 12 highlights the SWOT analysis performed by the research team on fixed-wing, rotary, and hybrid airframes. Conclusions from the SWOT analysis are presented in Section 3.3.3.

Table 12. Airframes SWOT Analysis

	S	W	O	T
Fixed-Wing	Longer flight endurance than multirotor. Increased data collection speed.	Requires linear space for launch and recovery. Requires additional space to perform turns. Higher minimum flight speed.	Long flight durations could increase operational efficiency.	Constant forward flight limiting maneuverability is not ideal during an emergency.
Multirotor	Smaller footprint required for takeoff and landing. More precise maneuverability.	Shorter flight endurance.	Ability to better constrain flights over smaller areas.	More takeoffs and landings increase operational time. A loss of a motor entails a loss of control.
Hybrid	Smaller footprint required for takeoff and landing. Longer flight endurance than multirotor. Increased data collection speed.	Requires additional space to perform turns. Higher minimum flight speed. Typically, the most expensive hardware.	Long flight durations could increase operational efficiency.	Propulsion failure can lead to a loss of VTOL capabilities.

3.3.2 Small Unmanned Aircraft Sensors SWOT Analysis

Table 13 highlights the SWOT analysis performed by the research team on RGB, thermal, LiDAR, hyperspectral, and GPR sensors. Conclusions from the SWOT analysis are presented in Section 3.3.3.

Table 13. Sensors SWOT Analysis

	S	W	O	T
RGB	Most commonly available technology, and typically the least expensive. Ability to acquire high-resolution imagery.	Unless turned into point cloud or Digital Elevation Models (DEMs), imagery only produces a two-dimensional data set.	Similarity of product to FOG observations enables faster analysis with minimal retraining requirements. Higher resolution sensors will allow for increase in efficiency.	If not combined with a 3D technology, RGB cannot quantify vertical distresses.
LiDAR	Produces a 3D point cloud data set. Can successfully collect data regardless of lighting conditions.	Limited horizontal resolving power, even at high point densities.	3D data allow detection of elevation or vertical distresses. Can be combined with other sensors to derive more accurate colorized point clouds than 3D imagery auto correlation.	If not combined with high-resolution imagery, some distresses could be harder to identify.
Thermal	Allows visualization of temperature variances.	Unless turned into point cloud or DEMs, imagery only produces a two-dimensional data set. Lower spatial resolution than RGB. Limited collection window to maximize the visibility of temperature variances.	Seeing thermal variances might help identify surface and subsurface characteristics not visible to other sensor technologies.	Cannot quantify vertical distresses. If not combined with a high-resolution technology, some distresses could be harder to identify.
Hyperspectral	Ability to detect a surface's chemical and mineral properties.	Unless turned into point cloud or DEMs, imagery only produces a two-dimensional data set. Lower spatial resolution than RGB. Large data files and high processing power requirements.	Hyperspectral imagery might help identify surface and subsurface characteristics, such as settlement/faulting and joint reflection cracking, which are not as visible to other sensor technologies.	Cannot quantify vertical distresses. If not combined with a high-resolution technology, some distresses could be harder to identify.

	S	W	O	T
GPR	Ability to determine subsurface conditions through nondestructive testing.	Low horizontal resolution. Not a surface condition detection technology. High complexity of use.	GPR might help identify subsurface characteristics, such as rooting, substrate cracking, and infrastructure penetrations, which are not as visible to other sensor technologies.	Air-coupled GPR antennas are potential sources of interference to both radar and communications equipment. This technology is best suited for subsurface analysis.

3.3.3 Conclusions of the SWOT Analysis Conclusions

As a conclusion of SWOT analysis, the research team selected all the airframes for testing due to their unique capabilities and advantages. While all identified sensor types demonstrated research/implementation in various applications, it was determined that hyperspectral and GPR were not applicable to conduct PCI analysis and were therefore removed from testing consideration.

The RGB sensor was chosen due to its high resolution and common availability. RGB imagery is the closest analog to FOG inspections. While RGB imagery does not natively enable the measurement of vertical distresses, the team believed that the majority of pavement distresses could be adequately detected and rated without vertical information.

The research team anticipated that the 3D point clouds generated by LiDAR would allow for detection and rating of vertical distresses that might be missed with an RGB imagery analysis. It was believed that LiDAR's lower resolving power would not negatively impact the research because it would be paired with the high-resolution RGB imagery.

Thermal was chosen for investigation due to its ability to capture temperature variances that are not visible in RGB imagery. The research team believed these temperature variances might reveal distresses not otherwise visible to the human eye. Similar to LiDAR, it was hypothesized that thermal's lower resolving power would not hinder the research when paired with RGB data sets.

The application potential of hyperspectral imagery and GPR for PCI analysis was unknown at the time of this research and was therefore removed from testing consideration. While these sensors might help identify pavement characteristics, the research team deemed that their challenges outweighed their potential benefits. Further research is recommended to understand their application in PCI analysis.

4. AIRPORT TEST PROCEDURES AND RESULTS—PHASE 1

Phase 1 testing was conducted at WWD, located in Rio Grande, New Jersey. sUAS data collection for Phase 1 was broken up into two stages: Stage 1 and Stage 2. The data collection

and processing were conducted during the months of December 2020 and January/February 2021 for FOG, DSV, and sUAS.

4.1 AIRPORT SELECTION

The research team selected WWD, an uncontrolled Class G airspace, as the initial testing site. WWD offered several key advantages ideal for initial testing: accessibility to both AC and PCC pavement surfaces; a wide variety of pavement distresses (as indicated in the 2020 survey); and a minimal level of additional coordination required due to an existing Memorandum of Agreement (MOA) between the FAA's ATR branch and the Delaware River and Bay Authority (DRBA) to safely execute FOG-, DSV-, and sUAS-based pavement inspections.

4.2 SMALL UNMANNED AIRCRAFT AIRFRAMES AND SENSORS

The research team tested a variety of airframes and sensors during Phase 1. Airframes can be equipped with sensors that collect a variety of data types, and the characteristics of the sensor can affect the quality of the data collected. Physically larger sensors can deliver higher dynamic range but offer shallower depth of field than smaller sensors, while higher resolutions can provide increased detail and clarity to captured images.

The airframes and sensors that were selected for initial testing represent the most used surveying and mapping platforms at the time this research was performed. The Mavic 2 Pro platform represents a consumer-grade platform, while other airframes and sensors used are all commercially available. Table 14 summarizes airframes, sensors, ground sampling distances (GSDs), data types, and software packages used in Phase 1.

Table 14. Summary of Systems and Software Used in Phase 1

Airframe	Sensor	GSD (mm)	Data Type	Image Processing	Data Analysis
DJI M210 RTK v2	X7-16mm, 24mm, 35mm	2, 4.9, 7.9, 10.8, 13.7, 25.4	RGB	Pix4D	Esri ArcMap, FAA PAVEAIR
	XT2 13mm	25.4	Thermal		
	X5S	2, 4.9, 7.9, 10.8, 13.7, 25.4	RGB		
DJI Mavic 2 Enterprise Dual	M2ED	2, 13.7, 25.4	RGB		
DJI Mavic 2 Pro	Mavic 2 Pro	2, 13.7, 25.4	RGB		
SenseFly eBee X RTK	S.O.D.A 3D	13.7	RGB		

DJI M210 RTK v2, shown in Figure 4, utilized the DJI Zenmuse X7 (RGB), X5S (RGB), and Zenmuse XT2 (thermal) payloads. This airframe, RGB cameras, and thermal camera were

identified to be used during Phase 1. The DJI Zenmuse X7 (24-megapixel) and DJI X5S (16-megapixel) cameras are commonly used in the surveying industry. The Zenmuse XT2 is a 13mm thermal camera, commonly used in a variety of applications. While the XT2 also has an RGB sensor, it was not evaluated in this research. The DJI M210 RTK v2 will herein be referred to as M210.

| (a) | (b) | (c) | (d) |
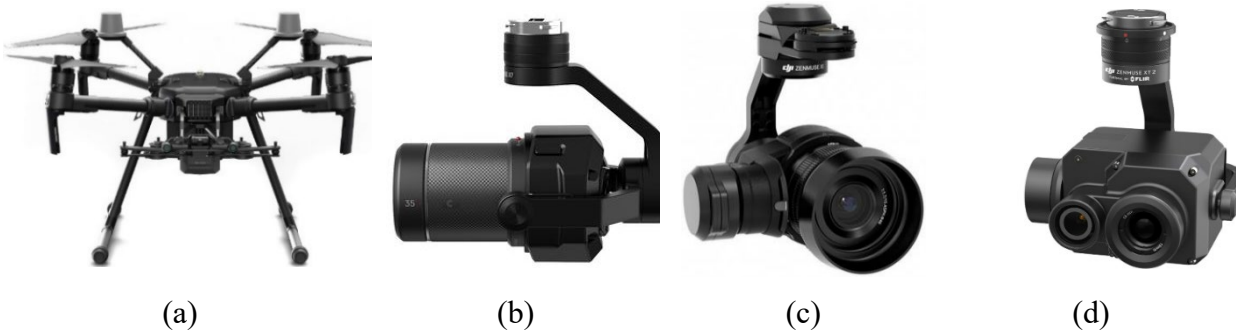
Figure 4. DJI M210 RTK v2 (a) with (b) Zenmuse X7, (c) Zenmuse X5S, and (d) Zenmuse XT2

DJI Mavic 2 Enterprise Dual, shown in Figure 5, was selected as it is a commonly used system in many industrial applications. This airframe utilized an onboard camera with RGB and thermal sensors. The onboard camera contains a 12-megapixel RGB, and a 0.30-megapixel thermal sensor, but the RBG was the only sensor evaluated in this research. The DJI Mavic 2 Enterprise Dual will herein be referred to as M2ED.

(a)   (b)

Figure 5. DJI Mavic 2 Enterprise Dual (a) with Onboard Camera (b)

DJI Mavic 2 Pro, shown in Figure 6, was selected due to it being a commonly used system in many industrial applications. This airframe utilized a 20-megapixel onboard RGB camera. The DJI Mavic 2 Pro will herein be referred to as M2P.

<div align="center">(a)   (b)</div>

Figure 6. DJI Mavic 2 Pro (a) with Onboard Camera (b)

SenseFly eBee X RTK, shown in Figure 7, was selected because it is a fixed-wing system capable of long endurance flight for data collection, thereby increasing operational efficiencies by eliminating the need for repeated landings. This system was equipped with a senseFly S.O.D.A. 3D, a 1-in., 20-megapixel camera that can achieve high resolutions even at a high altitude. The senseFly eBee X RTK will herein be referred to as eBee.

<div align="center">(a)   (b)</div>

Figure 7. SenseFly eBee X RTK (a) with SenseFly S.O.D.A. 3D (b)

4.3 TESTING METHODOLOGY

Before mobilizing field crews to the test areas, the research team developed a comprehensive testing methodology. Test areas at WWD allowed the team to perform initial testing, test a variety of airframes and sensors, collect data across several GSDs, and assess identifiable ASTM pavement distresses. Table 15 shows a breakdown of the testing rationale performed across the five test areas.

Table 15. Phase 1 Testing Methodology

Phase	Airport	Test Rationale	Test Area
1	WWD	Test variety of airframes and sensors, collect data across several GSDs, collect data across different pavement surfaces, assess identifiable pavement distresses	Runway 10/28
			General Aviation (GA) Asphalt Apron
			GA Concrete Apron
			Asphalt Taxiway
			Concrete Taxiway

Phase 1 evaluated the minimum acceptable GSD for using sUAS-derived data for pavement inspections. The research team initially tested 2-mm, 13.7-mm, and 25.4-mm GSDs in Stage 1 to create a low, medium, and high threshold. GSDs of 4.9 mm, 7.9 mm, and 10.8 mm were later added in Stage 2 to further polish the minimally acceptable standard.

4.4 STAGE 1 AND STAGE 2—WWD

This section details the initial testing performed at WWD including test areas, control data, sUAS data collection parameters, data processing workflows, and data analysis for PCI.

4.4.1 Test Areas

The pavement surfaces at WWD include a range of material types, as illustrated in Figure 8. The green shading represents AC surfaces, blue represents an asphalt overlaid over asphalt concrete (AAC) surface, and the red shading indicates PCC pavement types.
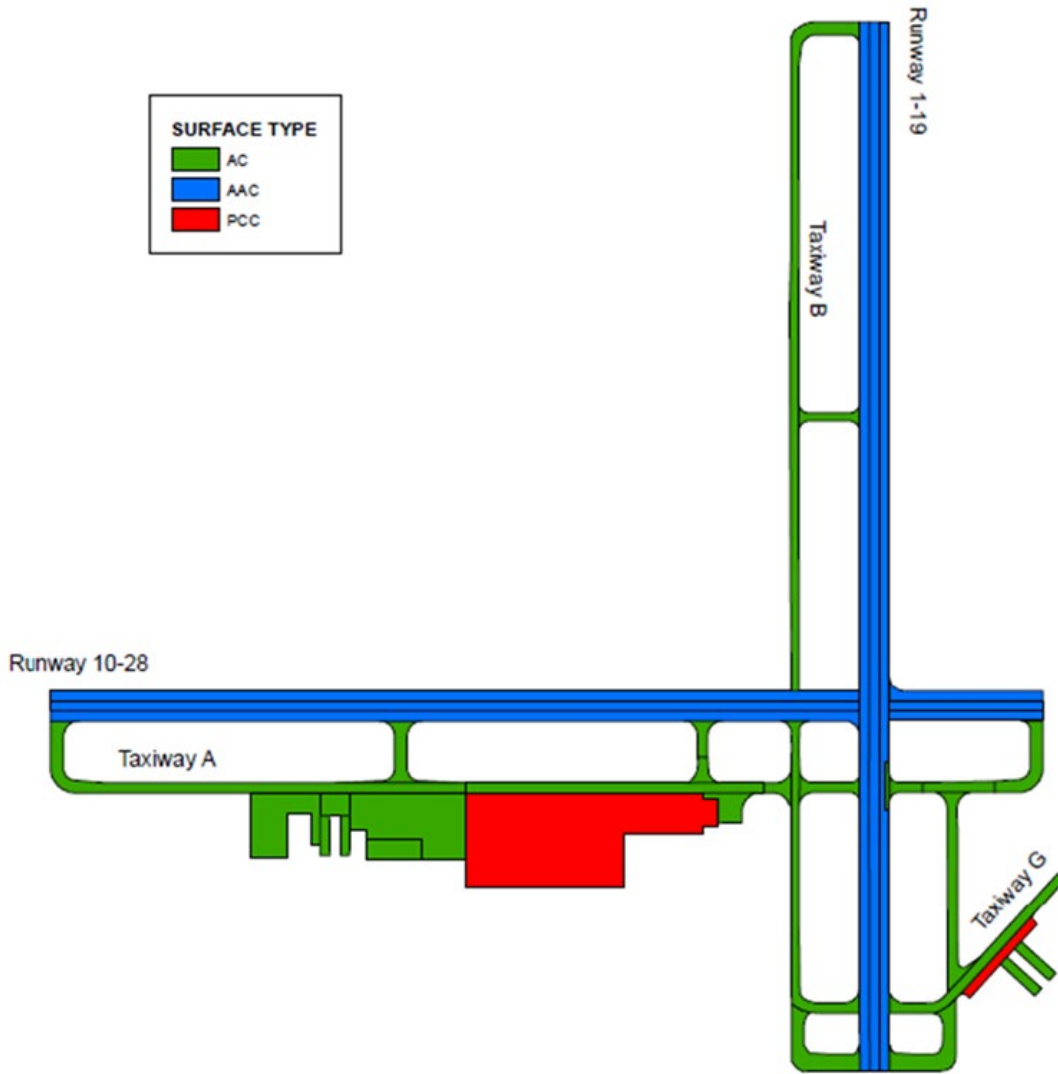
Figure 8. Pavement Surfaces at WWD

In June 2019, Applied Research Associates (ARA), a surveying company, conducted a conventional FOG PCI survey of the entire WWD airfield under a PMP update for the DRBA. This PCI survey was considered as a preliminary approach to the test area selection. Figure 9 illustrates section-specific pavement condition ratings for the entire airfield as reported in the 2019 survey.
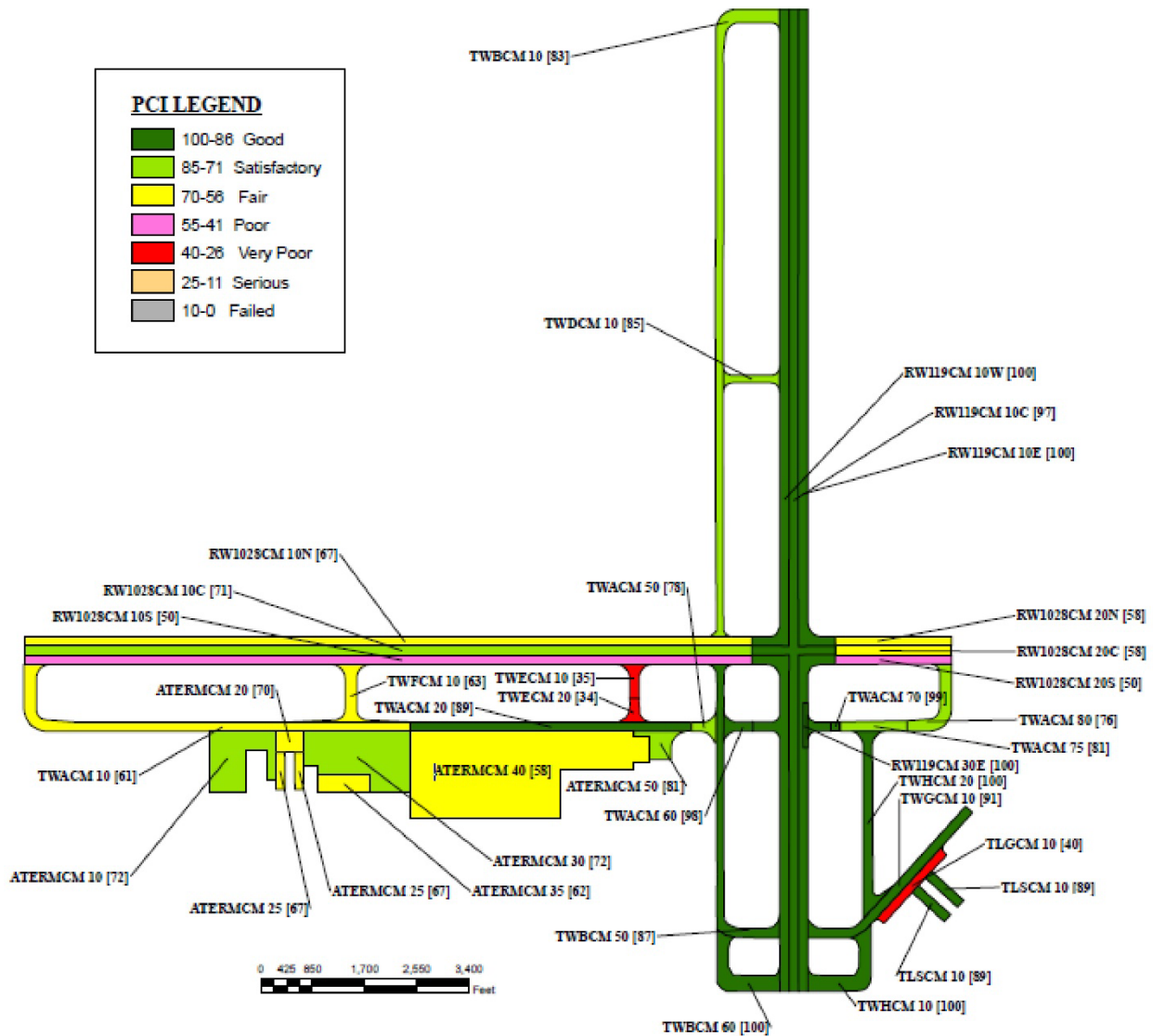
Figure 9. Pavement Condition Rating at WWD, June 2019

The average PCI rating for the airfield was found to be 71. The two runways had an average PCI of 79 and were above the minimum service level (MSL) of 70. MSL designates the minimum PCI threshold to trigger maintenance and/or rehabilitation. The MSL benchmarks for the runway, taxiway, and apron (or ramps) were documented to be 70, 65, and 60, respectively. Taxiways (including taxilanes) had an average inspected PCI of 72, and aprons had an average PCI of 62. Based on the ASTM D5340 PCI rating (ASTM International, 2020), the runways and taxiways were in "Satisfactory" condition, whereas the aprons were determined to be in "Fair" condition due to the higher severity of distresses identified during the survey.

Figure 10 illustrates the five test areas selected for comparative sUAS, FOG, and DSV testing. PCC areas were designated as 1A and 1B, whereas the AC test areas were marked with 2A, 2B, and 2C.

Figure 10. Test Areas at WWD

Each test area was further broken up into individual sample units. Table 16 presents the number of sample units to be inspected within those test sites.

Table 16. Sample Units at WWD

Test Area	Airfield Infrastructure	Type of Surface	Samples Inspected
1A	Apron	PCC	10 samples, 01–10
1B	Taxiway	PCC	2 samples, 01–02
2A	Runway	AC	8 samples, 01–08, 10S 8 samples, 09–16, 10C 8 samples, 17–24, 10N
2B	Taxiway	AC	2 samples, 01–02
2C	Apron	AC	8 samples, 01–08

4.4.1.1 Portland Cement Concrete Pavement

Test Area 1A

Test area 1A is a concrete apron located near the airport terminal on the southern side of Taxiway A. The 2019 PCI survey indicated that the rigid pavement in the apron area was in poor condition, with a PCI value of 58. This apron sees routine movement of most of the airport's traffic and parking. Typical aircraft operating on this apron are single engine, transient, and local general aviation (GA) traffic. The research team observed multiple severities of faulting, small patching, large patching, joint spalling, and corner spalling during the site visit. Linear cracking, shrinkage cracking, and replacement slabs were also observed. Most of the linear cracking had been saw cut with joint seal applied. This was an ideal survey site, as it contained the most common concrete distresses observed in an airfield. Figure 11 illustrates Site 1A along with its corresponding representative sample units.
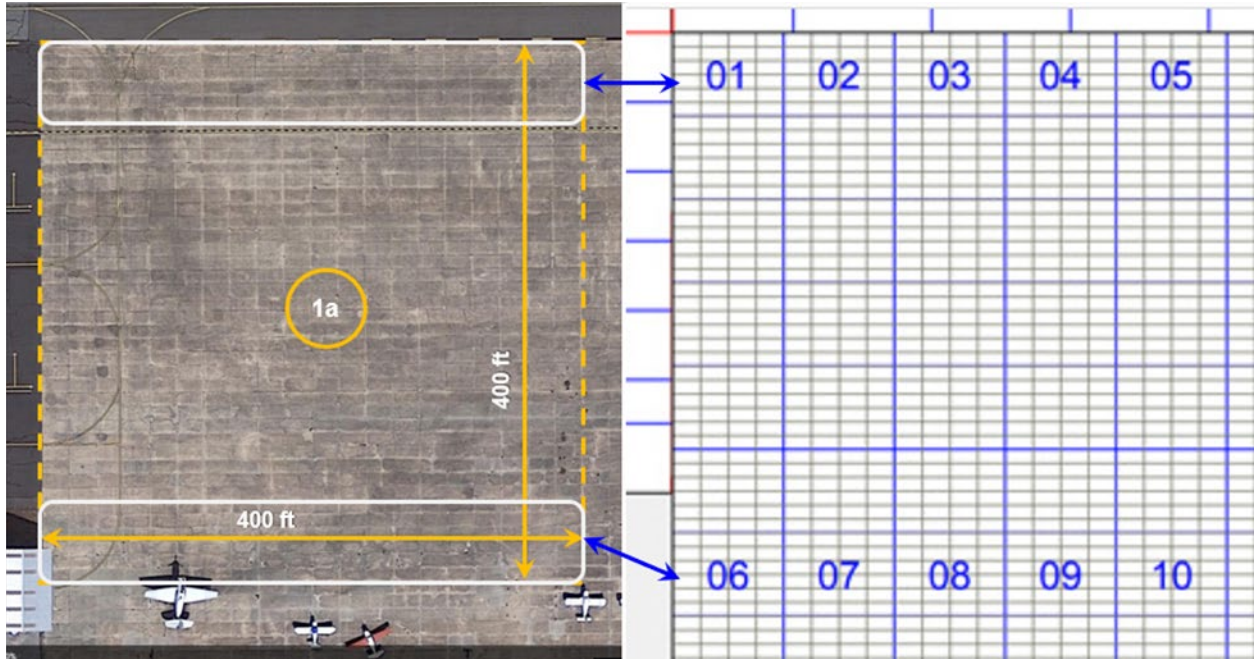
Figure 11. Test Area 1A at WWD

This test area was divided into representative sample units, each consisting of 24 10-ft x 20-ft slabs. Figure 12 (a) through (d) shows some of the distresses found in this.

| a | Small patch | b | Joint spalling |
| c | Large patch | d | Joint and corner spalling |
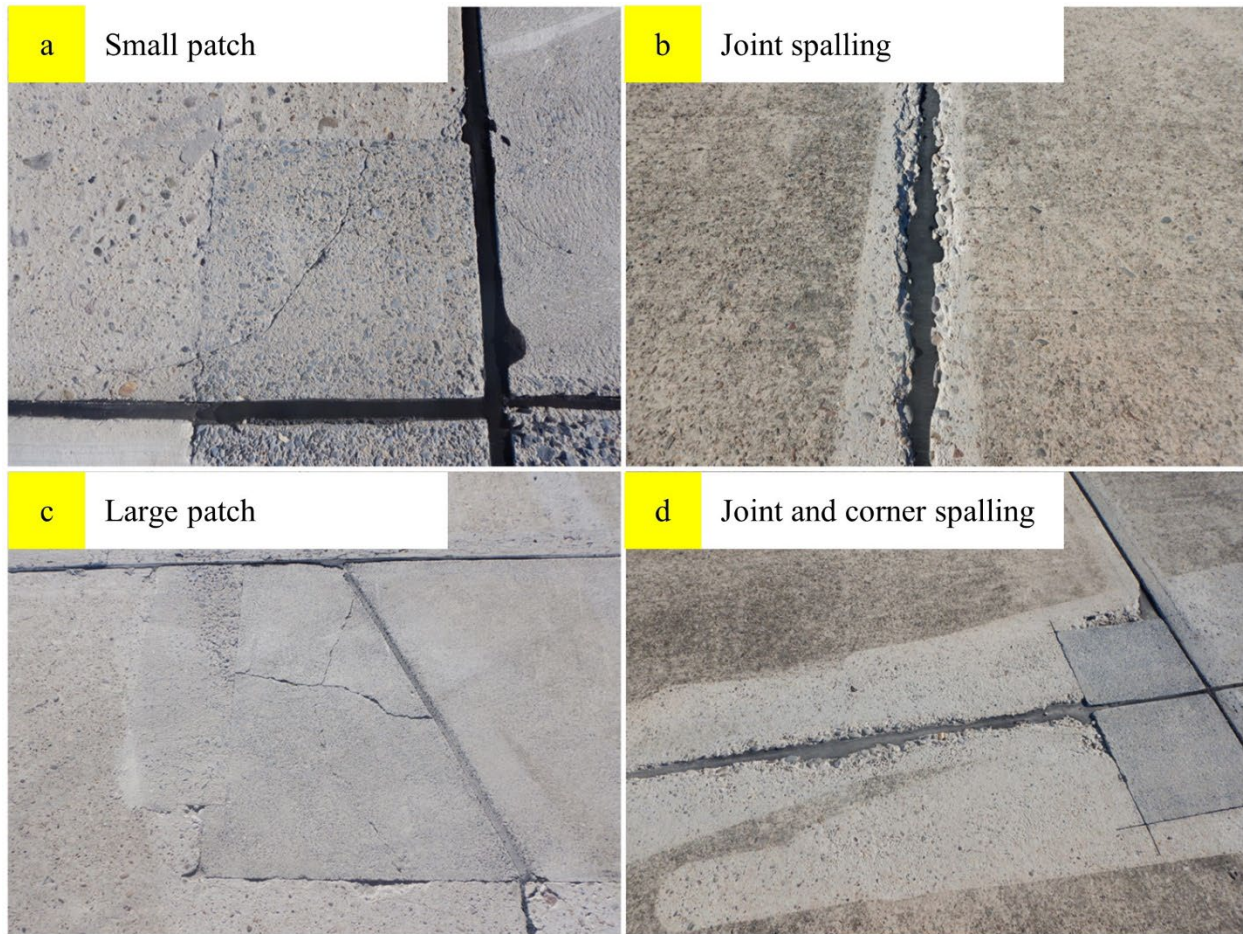
Figure 12. Distresses Observed on 1A at WWD

Test Area 1B

As illustrated in Figure 13, Test Area 1B is a concrete apron located at the southeast corner of the airfield, near Taxiway G. The 2019 PCI data showed the PCC pavement in this test area to be in very poor condition, with a PCI of 40. While the research team did not observe this test area during the site visit, the low PCI suggested that this area might have some unique distresses, such as shattered slabs and corner breaks.
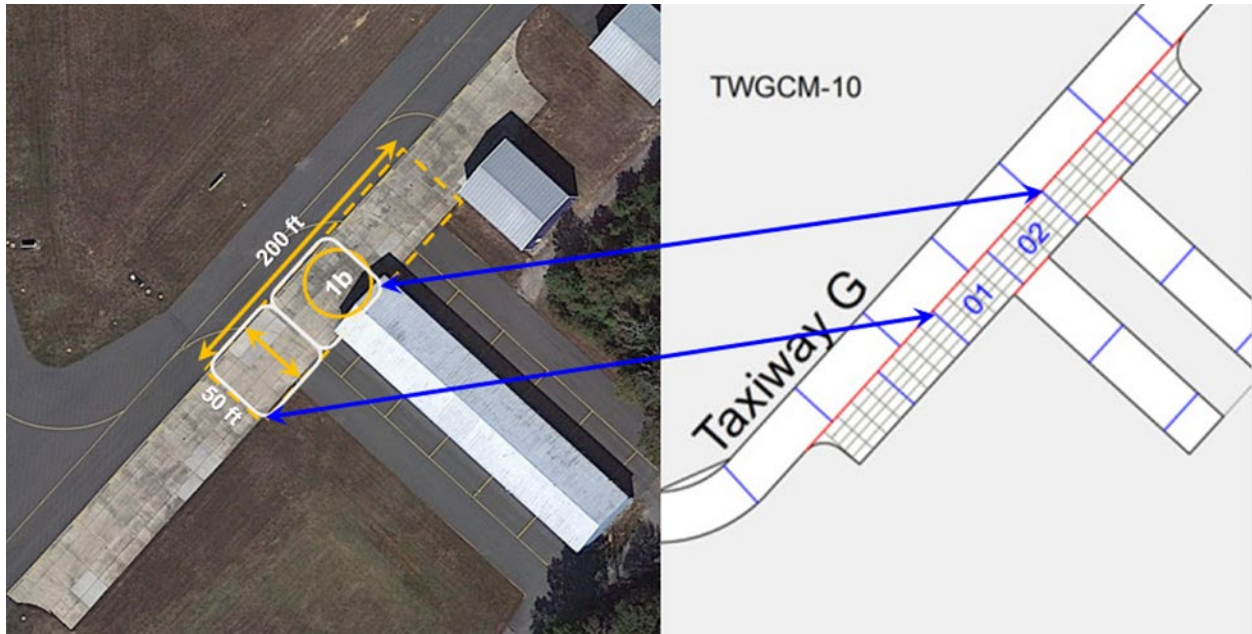
Figure 13. Test Area 1B at WWD

4.4.1.2 AC Pavement

Test Area 2A

Test Area 2A is situated at the west end of Runway 10/28, as illustrated in Figure 14. This runway, which was scheduled for complete reconstruction in 2021, had an aged asphalt pavement (non-grooved) with aged crack sealant and a PCI averaging approximately 65. Due to multiple distress severities of longitudinal and transverse cracking, weathering, and block cracking, the research team selected it as the primary asphalt test area. The entire runway was observed as part of the November 2020 site visit. Figure 15 highlights the observed block cracking and the longitudinal and transverse cracking.

The AC runway is 150 ft wide. This transverse width was divided into three equal stretches of 50 ft in accordance with the PCI section width. The middle 50-ft stretch represented the keel area where the AC pavement is subjected to most of the aircraft traffic. The other two transverse segments fall outside the keel area of the runway. These segmented widths were longitudinally divided every 100 ft to constitute a sample unit having an area of 5,000 square feet (sq ft) (50 ft x 100 ft).
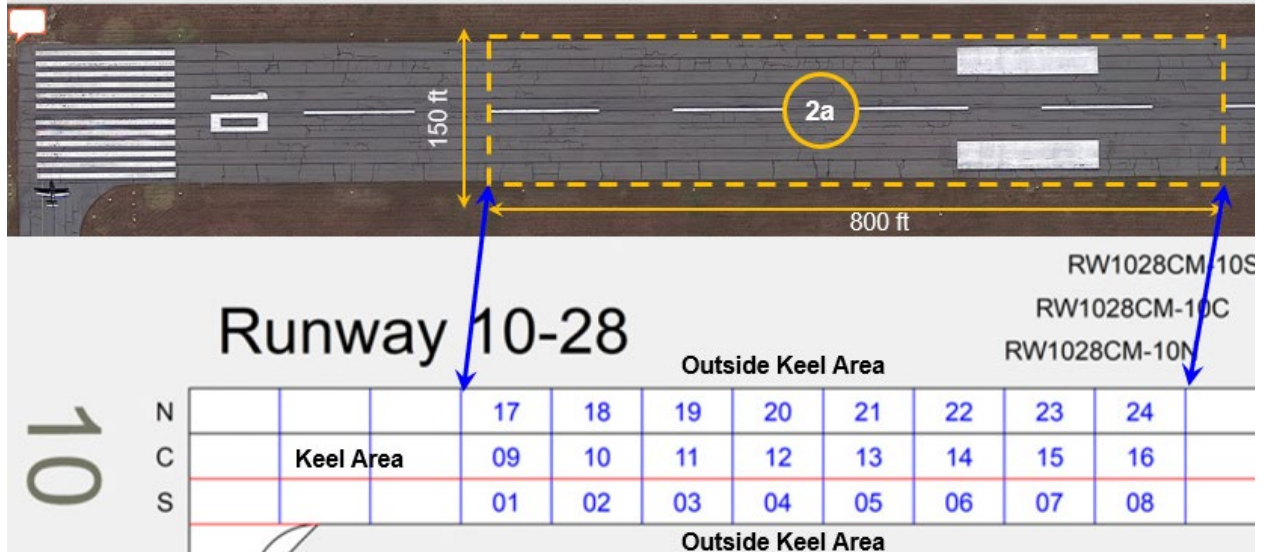
Figure 14. Test Area 2A at WWD
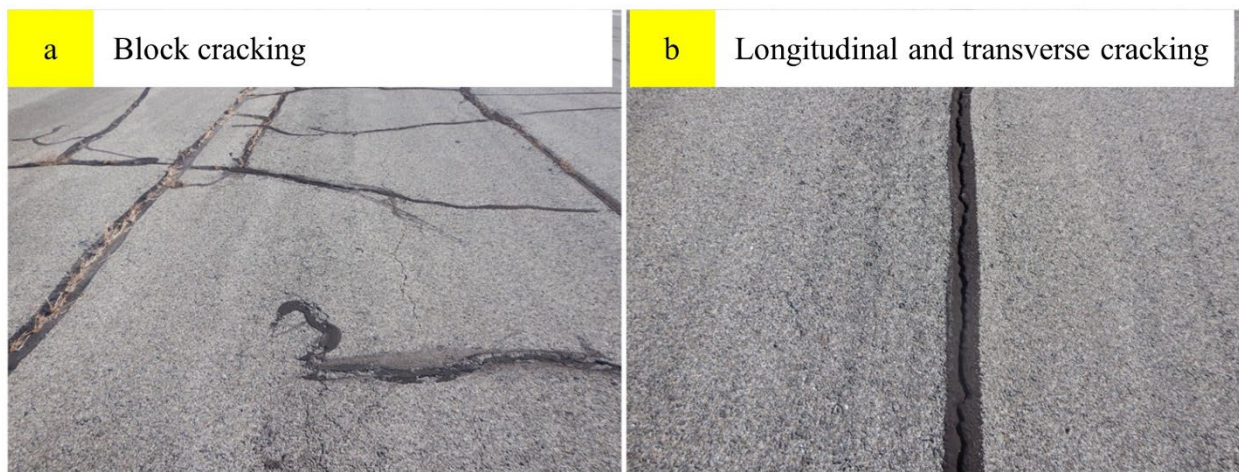
Figure 15. Distresses Observed on Test Area 2A at WWD

Test Area 2B

Figure 16 illustrates Test Area 2B, located on Taxiway E. It is an asphalt taxiway with some medium-severity alligator cracking that was observed during the site visit (see Figure 17). The 2019 PCI for Area 2B was 34, indicating that the pavement was in very poor condition. The 70-ft-wide taxiway was segmented into two 80-ft-long sample units. Thus, sample units 11 and 12 had an area of 5,600 sq ft, slightly larger than the Runway 10/28 and apron sample unit areas.
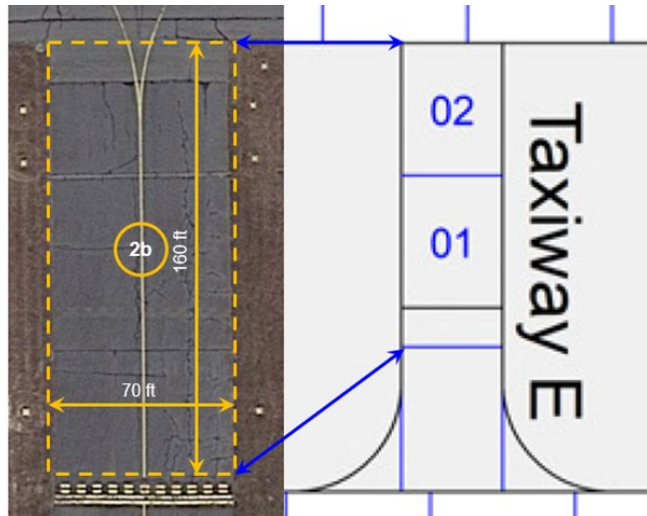
Figure 16. Test Area 2B at WWD

Figure 17. Alligator Cracking Observed on Test Area 2B at WWD

Test Area 2C

Figure 18 illustrates the AC surface in Test Area 2C. This aged asphalt apron area is adjacent to the PCC Area 1A. The research team selected it as a complementary test location due to three unique distresses that were not observed on Runway 10/28: shoving near the adjacent PCC apron, raveling due to loss of an aged surface seal, and an oil spillage. Like the Runway 10/28 sample units, these samples also had an area of 5,000 sq ft. Figure 19 depicts the shoving, and the oil spillage between the AC and PCC apron interface.
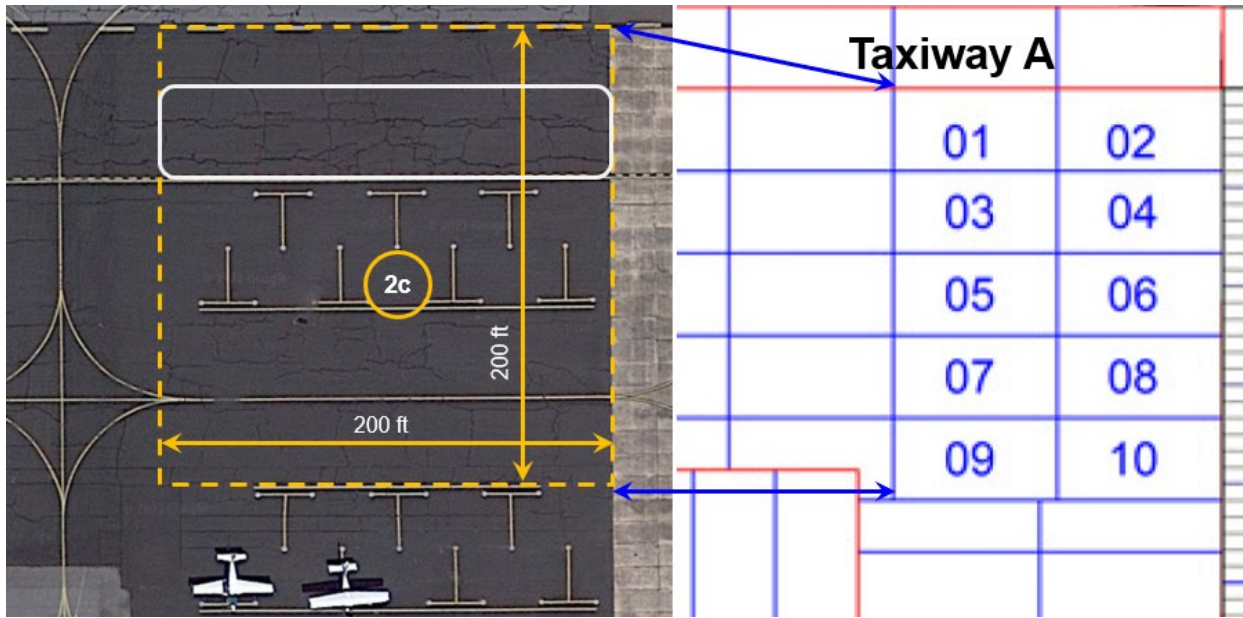
Figure 18. Test Area 2C at WWD
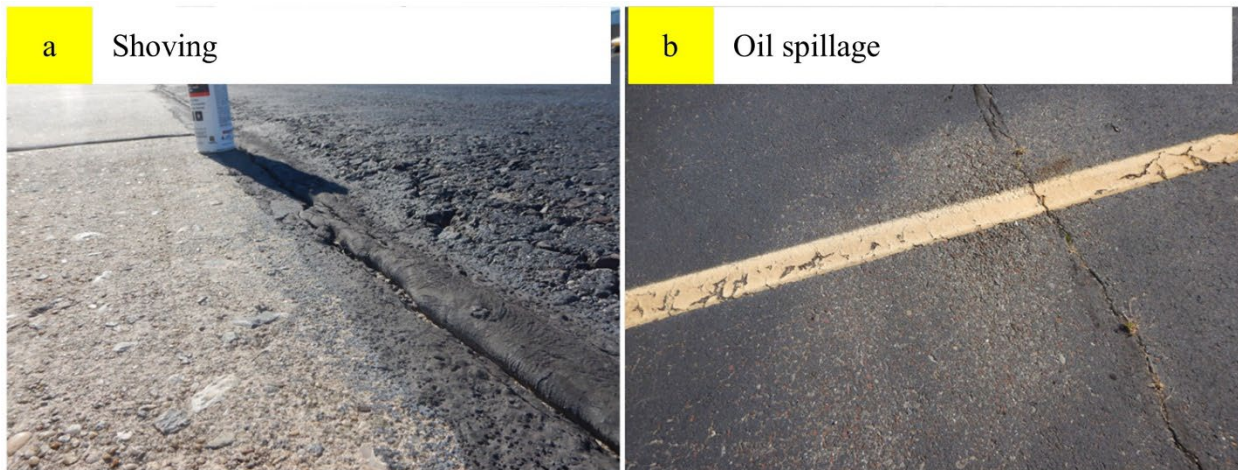
Figure 19. Distresses Observed on Test Area 2C at WWD

Appendix B includes the specific distresses recorded during the November 2020 site visit. Associated PCI values from the 2019 survey are also presented alongside the prominent distress description and ASTM standardized numerical identifiers.

4.4.2 Control Data—FOG and DSV

Control data sets were collected through FOG and DSV surveys. This section discusses FOG and DSV workflows for pavement inspections.

4.4.2.1 Foot-on-Ground Data Collection and Processing

Experienced pavement technicians from ARA conducted FOG PCI evaluations for all five test areas at WWD in December 2020. Figure 20 shows ARA technicians on site.

Figure 20. Collection of FOG Data at WWD

The FOG data collection team employed the following workflow, illustrated by Figure 21.
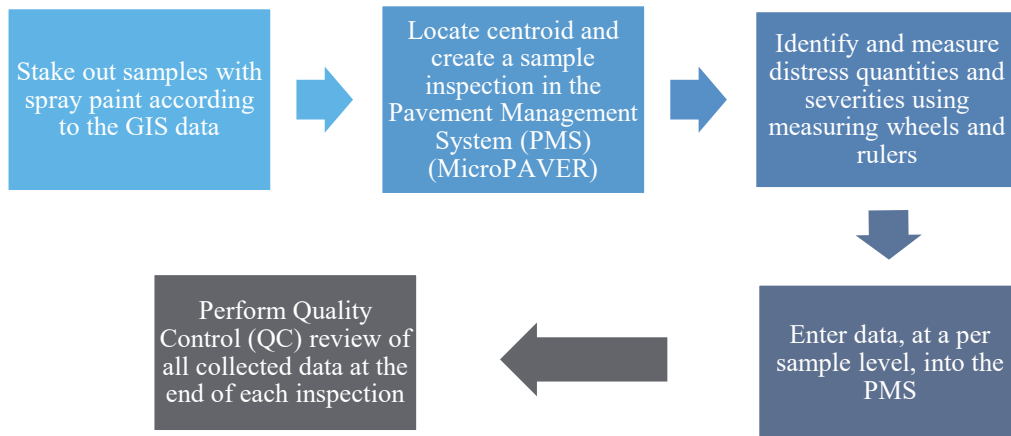
Note: MicroPAVER was used with current GIS and tag image file format (TIFF) information and with active Global Positioning System (GPS) on handheld tablets.

Figure 21. Workflow for FOG Data Collection

Table 17 summarizes the distresses that technicians observed at WWD during the FOG survey conducted as part of this research effort.

Table 17. Distresses Observed During FOG Survey at WWD

AC Distresses			PCC Distresses		
Distress Code	Distress Description	Severities	Distress Code	Distress Description	Severities
41	Alligator Cracking	L, M, & H	63	Linear Crack	L, M, & H
43	Block Cracking	L, M, & H	66	Small Patch	L, M, & H
48	L&T Crack	L, M, & H	67	Large Patch	L, M, & H
49	Oil Spillage	N/A	71	Faulting	L, M, & H
52	Raveling	L, M, & H	73	Shrinkage Crack	N/A
54	Shoving	L, M, & H	74	Joint Spall	L, M, & H
57	Weathering	L, M, & H	75	Corner Spall	L, M, & H

The FOG data processing team implemented the following workflow (illustrated in Figure 22) upon completing the field data collection.

Figure 22. Processing Workflow for FOG Data

To ensure research and testing for a full range of pavement distresses, the remaining distresses— some of which are rarely encountered in an airfield—were specifically sought when developing Testing Methodologies for data collection at other airports in Phase 2 testing.

4.4.2.2 Data Collection and Processing for DSV

The survey team collected DSV data for all five test areas at WWD in December 2020. Temperatures experienced on these days were in the mid-30s to low 40s °Fahrenheit, which is the optimal operating temperature for a DSV.

The DSV data collection workflow was as follows:

- Panoramic imagery was captured via a 360° camera on the vehicle roof.
- A Pavemetrics proprietary Laser Crack Measurement System (LCMS) was deployed on the pavement surface scans to map and quantify the pavement distresses.
- Ride quality (roughness), macrotexture (raveling), and transverse profile (rutting and defect depth) data were also collected with the same LCMS system.

- Geolocation and linear distance data for each data element were recorded.
- Four onboard computers, shown in Figure 23, collected and stored each data set.
- Using a triple monitor workstation (also shown in Figure 23), the operator observed and reviewed data as they were collected.
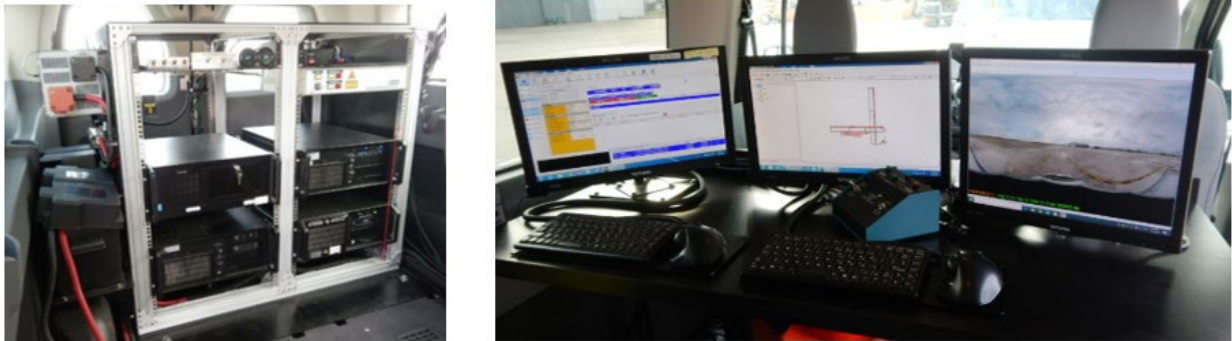
Figure 23. Computers Onboard DSV

- Prior to collection, a routing plan was developed in-office by utilizing the airport's GIS and its predefined sectioning system for FOG PCI survey.
- The DSV traversed along 10 evenly spaced transverse offsets over the full length of the runway to ensure optimal coverage of the entire length and width.
- The photographic scans were overlapped such that no area of the runway was omitted from subsequent distress mapping.
- For PCC sections that were 10-ft wide, one pass was made in the center of each longitudinal set of slabs with the DSV. The DSV's capture range from center is 6.5 ft.
- To ensure that the operator maintained a straight pass, lines were measured and marked with spray paint (shown in Figure 24) at the beginning, middle, and end of each sample.

Figure 24. Collection of DSV Data at WWD

- All AC DSV data were collected from west to east.
- An initial pass was made centered 6 ft from the north side of each test area with each sequential pass shifted 12 ft south to allow for partial imagery overlap.

The routing plan ensured the most efficient survey route while providing full coverage of all pavements requiring evaluation. When collecting data over wide pavements, such as airport runways and taxiways, the survey plan included an overlap of approximately 2 to 4 ft for each pass to ensure no areas of pavement were missed. Following the DSV survey, all raw data were sent for immediate quality assurance (QA) review, imagery extraction, data archival, and editing for the evaluation process.

The DSV used was a first-generation LCMS and was constructed by International Cybernetics Connect (ICC). The data processing was completed via ICC workstations via the workflow illustrated in Figure 25.

| Digital data were overlaid on the airfield's PMS data, utilizing the shapefile layer and events recorded by the DSV operator to assign the data to the correct section of pavement. | → | Data were manually analyzed to quantify the distresses for the entire pavement section. | → | Random "samples" were extracted from the data set. |

| Intensity and depth imagery were analyzed by a pavement inspector to conduct a manual distress takeoff of the pavement sections as each type of imagery accentuates certain distresses. | ← | The processing technique was then adjusted for comparison with the FOG and sUAS data sets. This technique sectioned each sample into their own individual sections and properly aligned the data with the samples from the FOG and sUAS. |

Figure 25. Processing Workflow for DSV Data

4.4.3 Data Collection Parameters for sUAS

sUAS data collection efforts were carried out in two stages at WWD. Stage 1 was executed in December 2020 and Stage 2 was executed in January and February 2021. Each of these sUAS data collection days represents a range of weather, from cloudy, overcast skies to bright, sunny days, and calm to gusting wind conditions. Weather conditions for each flight were logged in flight cards that were completed before and after each operation. Adverse weather resulted in the

delayed execution of Stage 2, but separating the sUAS operations into two stages allowed the research team to review and implement lessons learned during Stage 1 and further refine the execution of Stage 2.

Figure 26 presents the workflow followed by the data collection team.
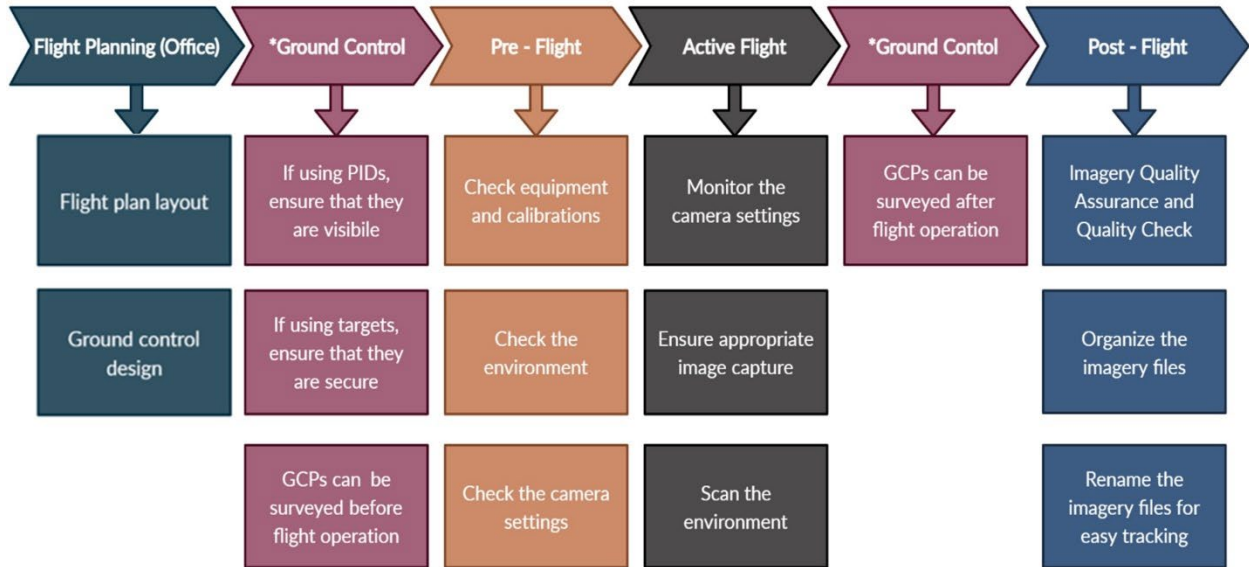
Figure 26. Raw Data Collection Workflow for sUAS

4.4.3.1 Stage 1 Data Collection Parameters

Initial testing during Stage 1 was aimed at conducting 30 sUAS operations over test areas 1A and 2C. These parameters focused on testing a wide variety of systems at several GSDs ranging from 2 mm to 25.4 mm.

A summary of the sUAS flights executed as part of Stage 1 (and actual flight time and total number of photos captured in each test area) is presented in Appendix C, Table C-1. All flights with a dual-frequency-enabled system were connected to a real-time kinematic network during flight. Real-time kinematic (RTK) and post-processing kinematics (PPK) are techniques that enable greater accuracy than autonomous global navigation satellite system (GNSS) positioning. They are accomplished by having a GNSS base receiver set at a point with a known position, and a rover (aircraft) GNSS receiver at the unknown point. This allows for accurate determination of the rover's position relative to the base.

Flights crossed out in red in Appendix C, Table C-1 could not be executed, as they were operationally incapable or posed a safety concern due to extremely low altitudes flown or proximity to buildings. Table 18 summarizes these flights.

Table 18. Field Flight Cancellations During Stage 1 Data Collection

Flight Number	Field Flight Cancellation Reason
8	Very low to buildings and would cross Runway 10/28 safety area.
9	Very low to buildings and would cross Runway 10/28 safety area.
13	Cannot plan for flight lower than 40 ft above ground level (AGL).
23	Very low to buildings/vegetation, area was very small for fixed-wing.
24	Very close to Runway 10/28 safety area, area was very small for fixed-wing.
28	Cannot plan for flight lower than 40 ft AGL.

All other sUAS missions summarized in Appendix C, Table C-1 were executed successfully, but several modifications to flight plans were made to allow the sUAS to complete the data collection. Table 19 summarizes modifications made in the field to the Stage 1 flight plans.

Table 19. Field Modifications During Stage 1 Data Collection

Flight Number	Field Modifications & Justification
1	Revised to 35mm sensor at 75/60 overlap and switched into continuous flying data capture setting to allow sUAS to operate at 61.5 ft AGL.
5	Revised to 74/60 overlap and switched into continuous flying data capture setting to allow sUAS to operate at 30 ft AGL.
10	Revised to 74/60 overlap and switched into continuous flying data capture setting to allow sUAS to operate at 30.4 ft AGL.
16	Revised to 35mm sensor at 75/60 overlap and switched into continuous flying data capture setting to allow sUAS to operate at 61.5 ft AGL.
20	Revised to 74/60 overlap and switched into continuous flying data capture setting to allow sUAS to operate at 30 ft AGL.
25	Revised to 74/60 overlap and switched into continuous flying data capture setting to allow sUAS to operate at 30 ft AGL.

In addition to the flight modifications listed in Table 18, the sUAS data collection team made and documented several observations that needed to be taken into consideration for future sUAS data collection efforts. These in-flight findings are as follows:

- **"Hover and Capture" vs "Continuous Flying" data capture mode**

  For 2-mm GSD, the flight operations team found that DJI systems fail to maintain their gimbal settings (i.e., pitch, yaw, roll) when the sUAS is commanded to hover at each photo center. During "hover and capture," the sUAS quickly pitches hard forward to gain speed and then commands a stop by performing a hard-backwards pitch. The flight team found that this appears to confuse the onboard computer into drifting out of its zero point. To mitigate this system limitation, the flights were revised to follow the "continuous flying" mode with the "equal distance capture interval" method. Additionally, to collect

data at the 2-mm GSD, four of the flights required the overlap settings to be reduced by a small margin—from 75 forward overlap down to 74.

- **Surface brightness of collection area effects data consistency**

  Similar to a human eye being blinded when a light turns on in a dark room, sUAS sensors can also be "blown out" when collecting imagery of pavement. All the tested systems allow the user to set and use "automatic" settings that allow the camera to adjust the ISO, aperture, and shutter speed, but this does not always occur quickly enough relative to the sUAS's speed, which leads to inconsistent exposure levels. For the purposes of this testing, all payloads testing on multirotor airframes were set to "Shutter Priority Mode," where the pilot locks the shutter speed, and the camera adjusts the ISO and aperture to decrease the likelihood of motion blur during image capture. The flight team found two major conditions that could cause sUAS sensors to incorrectly expose an image, potentially leading to issues with data consistency:

  1. Transitions between different pavement materials (concrete vs asphalt)
  2. Transitions between buildings (such as a highly reflective tin roof) and the target concrete/asphalt

  The research team considered this finding during data processing and analysis.

- **DJI—Focus issues at low altitudes**

  The flight team discovered that the DJI systems used to collect high-resolution imagery at low altitudes sometimes struggled with autofocusing. When using best practices such as focusing on features with high contrast, this issue was mostly mitigated.

- **M210—Gimbal drift**

  The flight team found that the gimbals used on the M210 drifted over time. Drift was most commonly observed during "hover and capture" mode and with an increased number of flight lines. Both scenarios resulted in excessive aircraft movement. The most common axis of drift was yaw. Halfway through data collection, remote pilots observed (through the live camera feed) that the camera was drifting a yaw of up to 10 degrees from the correct orientation. Data were collected with the sensor's widest section perpendicular to the flight line. When the camera fails to maintain the proper orientation, issues with image overlap could occur. When utilizing best practices, such as manually adjusting the yaw during flight, this issue was mostly mitigated.

4.4.3.2 Stage 2 sUAS Data Collection

Data collection for Stage 2 aimed at conducting a total of 58 sUAS operations over Test Areas 1B, 2A, 2B, and 2C. Three additional GSDs between 2 mm and 13.7 mm were evaluated as an attempt to collect sufficient image quality while introducing operational efficiencies. A summary of the sUAS flights executed, as actual flight times, and total number of photos captured in each test area are presented in Appendix C, Table C-2.

Flights crossed out in red could not be executed, as they were operationally incapable or posed a safety concern due to extremely low altitudes flown or proximity to buildings. Table 20 summarizes these flights.

Table 20. Field Flight Cancellations During Stage 2 Data Collection

Flight Number	Field Flight Cancellation Reason
77	Hangar obstruction—flight altitude too low
82	Hangar obstruction—flight altitude too low
87	Equipment limitations prevented operating at lower AGLs, and intrusion into RWY 01 safety area.

RWY = Runway

The sUAS missions summarized in Appendix C, Table C-2 that were executed successfully were then sent to the data processing team for orthomosaic generation.

4.4.4 Stage 2 sUAS Data Processing

After data collection was complete, the data processing team used Pix4Dmapper to stitch unedited images together for orthomosaic generation. The data processing team organized and established a workflow for data collected from each flight card listed in Stage 1 and Stage 2 data collection parameters. Figure 27 illustrates the workflow followed by the processing team.
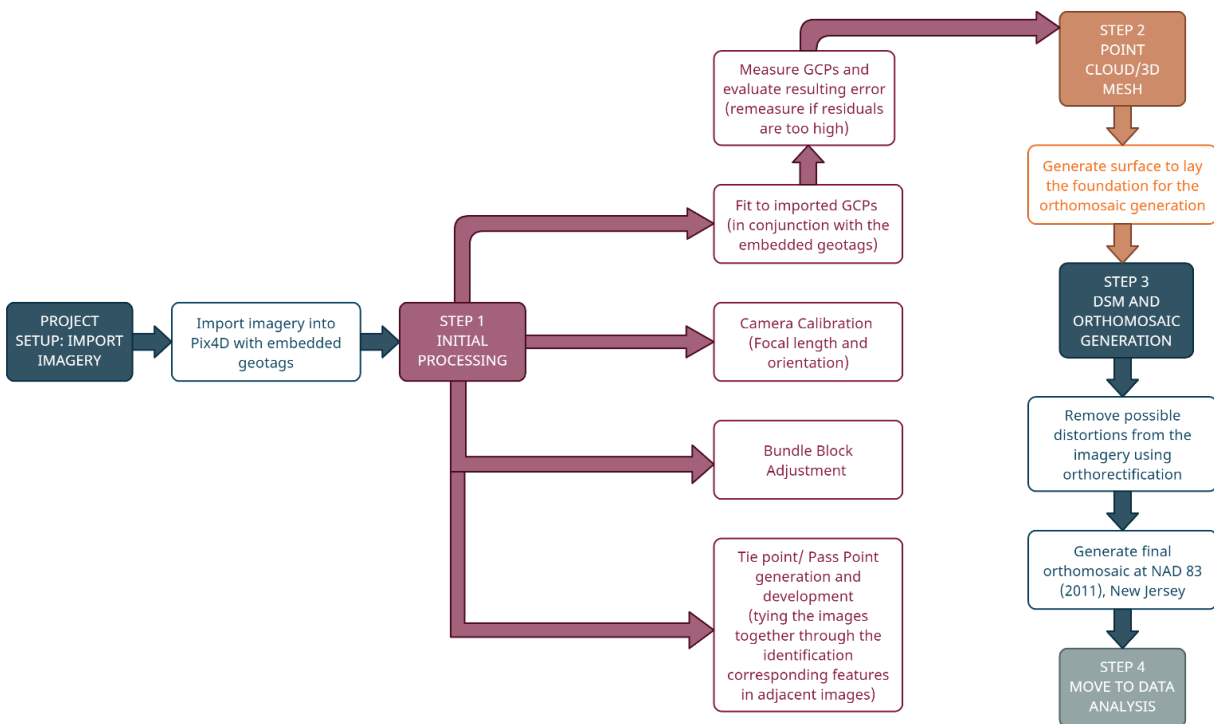
Figure 27. The sUAS Raw Data to Orthomosaic Processing Workflow

The processed orthomosaics were carefully reviewed for anomalies before they were delivered for pavement analysis. Any anomalies identified were documented and evaluated for reprocessing.

Figure 28 illustrates the images generated in different steps of the processing workflow illustrated in Figure 27.
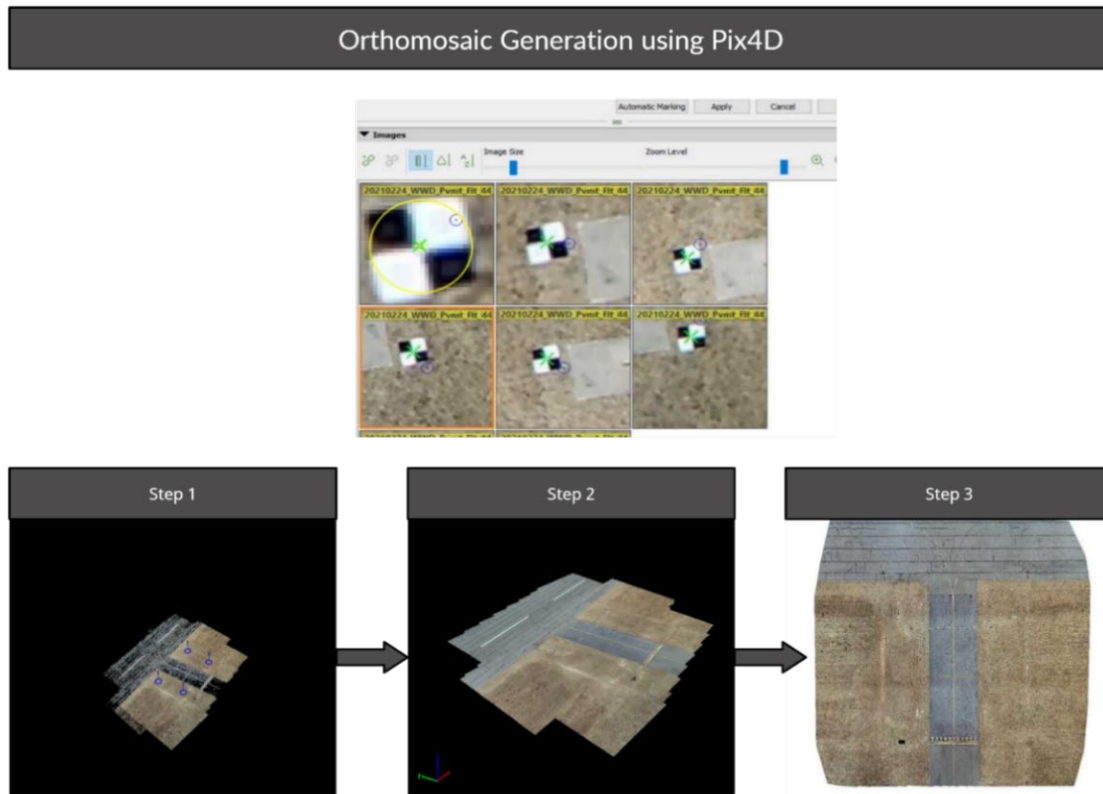
Figure 28. The sUAS Raw Data to Orthomosaic Processing Workflow

4.4.5 Data Analysis and Evaluation for sUAS

After orthomosaic generation, the subject matter experts (SMEs) performed both an automated and a manual distress analysis to assess the pavement health. The aim of this step was to identify the types and severity of pavement distresses that are recognizable in both the automated and the manual workflows.

The SMEs reviewed the orthomosaics, with the initial review indicating that the 2-mm GSD imagery was the most effective for identifying pavement distress. Therefore, 2-mm GSD imagery was chosen to perform the manual analysis.

Figure 29 represents examples for the quality of sUAS imagery acquired with the same sensor across several GSDs. It was apparent that the 2-mm GSD was the most effective when used for pavement condition assessment due to its ability to capture low-severity distresses. As the GSD increased, the ability to digitally identify low-severity distresses decreased.
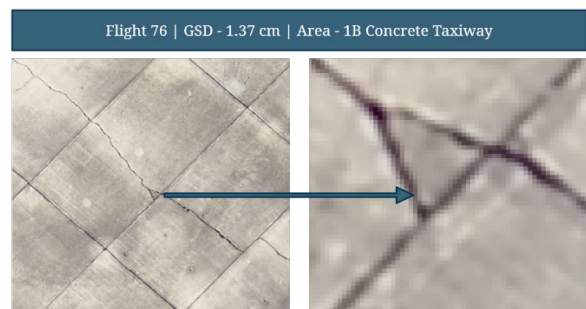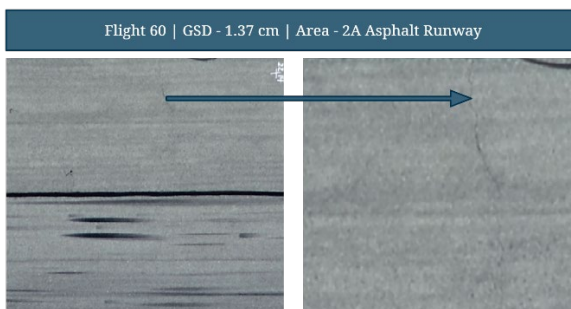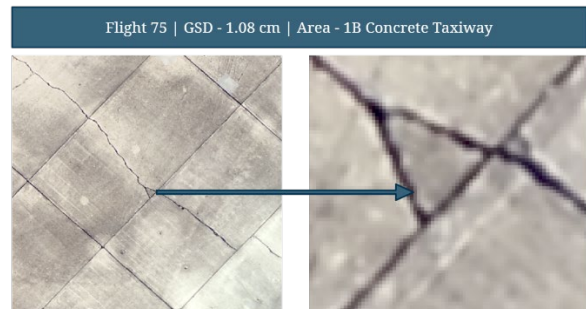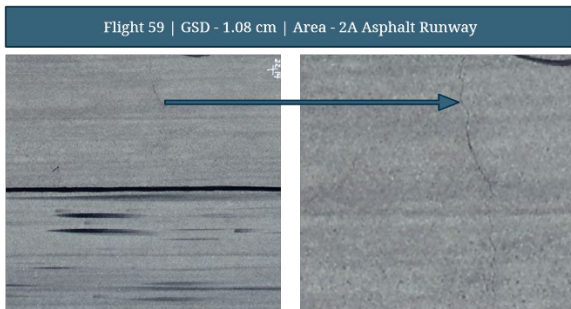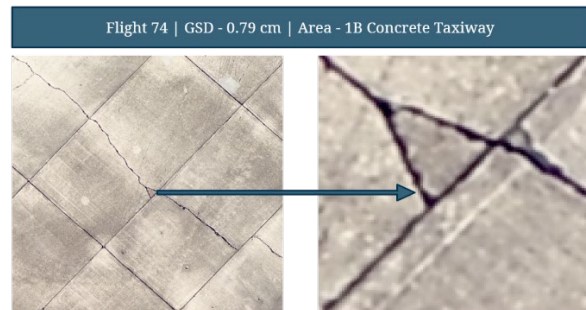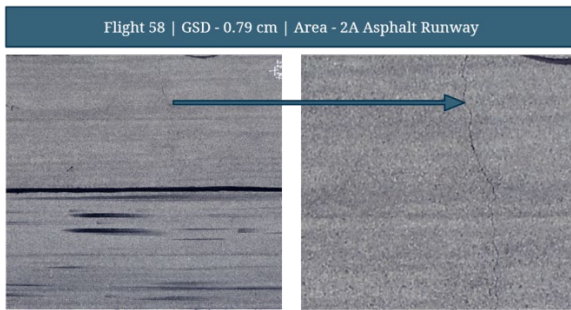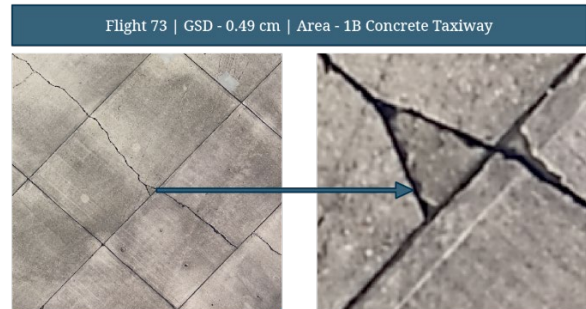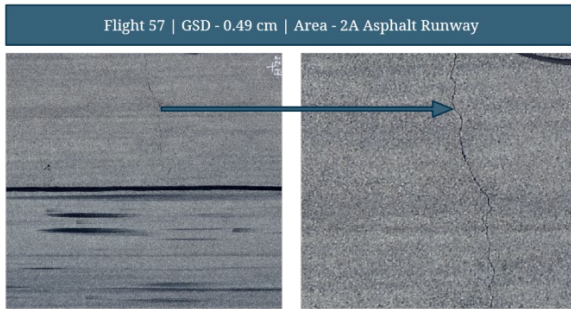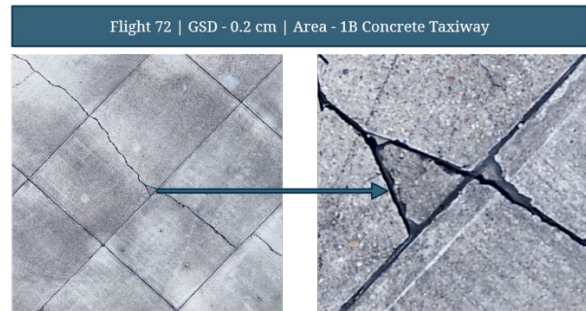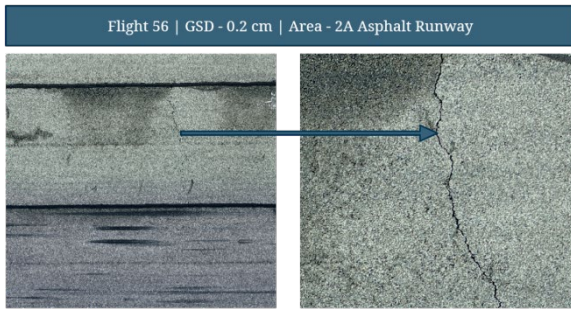
Figure 29. Comparison of GSD on AC and PCC Pavement

It should be noted that the 2-mm GSD imagery varied in quality when captured with a range of sensors. Figure 30 shows a comparison of the same distress at 2-mm GSD across the variety of sensors tested.

(a) DJI M210 X7-35mm

(b) DJI M210-X5S

(c) DJI Mavic 2 Pro

Figure 30. Sensor Comparison at 2-mm GSD

4.4.5.1 Automated Distress Analysis

Based on the recommendations from the initial review of the processed orthomosaics, a 2-mm GSD orthomosaic from Flight 14 (M210) was processed in eCognition to test workflows

associated with the automated extraction of pavement distress. To reduce processing time, this orthomosaic was tiled out into 50 smaller individual data sets. Figure 31 illustrates the workflow for automated distress analysis.
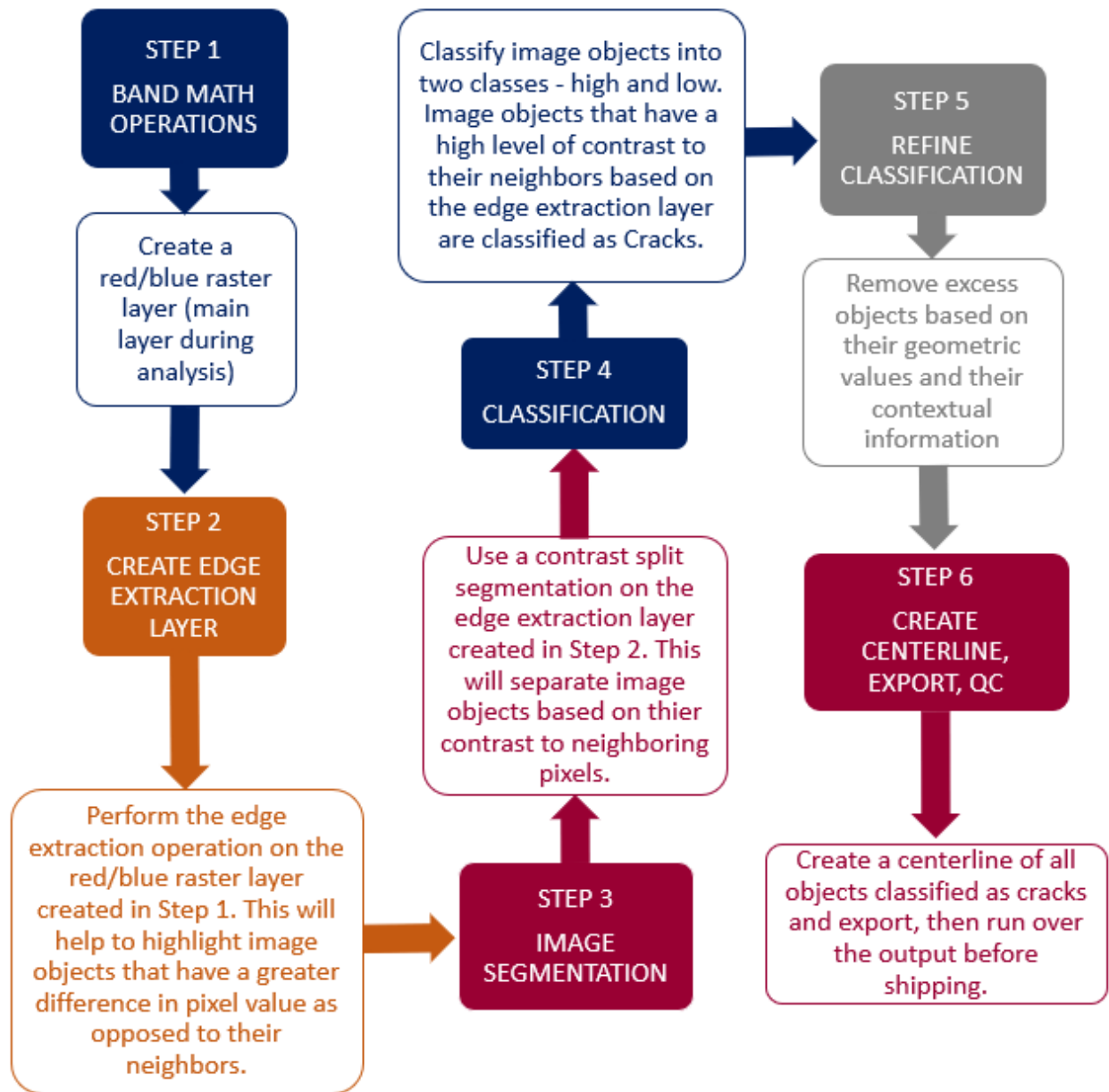
Figure 31. Automated Distress Analysis Workflow

The following methods were used within eCognition to extract pavement distresses. This workflow was developed to assess concrete data sets and only extract cracking distresses. The methods developed are sensor-specific, and the extraction algorithms will need to be adjusted when being used on another sensor.

Band Math and Edge Extraction

At a finer resolution, edge extraction methods were a viable option and were incorporated into the analysis in combination with simple band ratios. eCognition has different edge extraction processes; for crack analysis, the best option is the Lee Sigma Edge Extraction[1] method as depicted in Figure 32. Before the output layer from this process could be used, the research team utilized a convolutional layer to get rid of noise and pixilation.

(a)   (b)   (c)
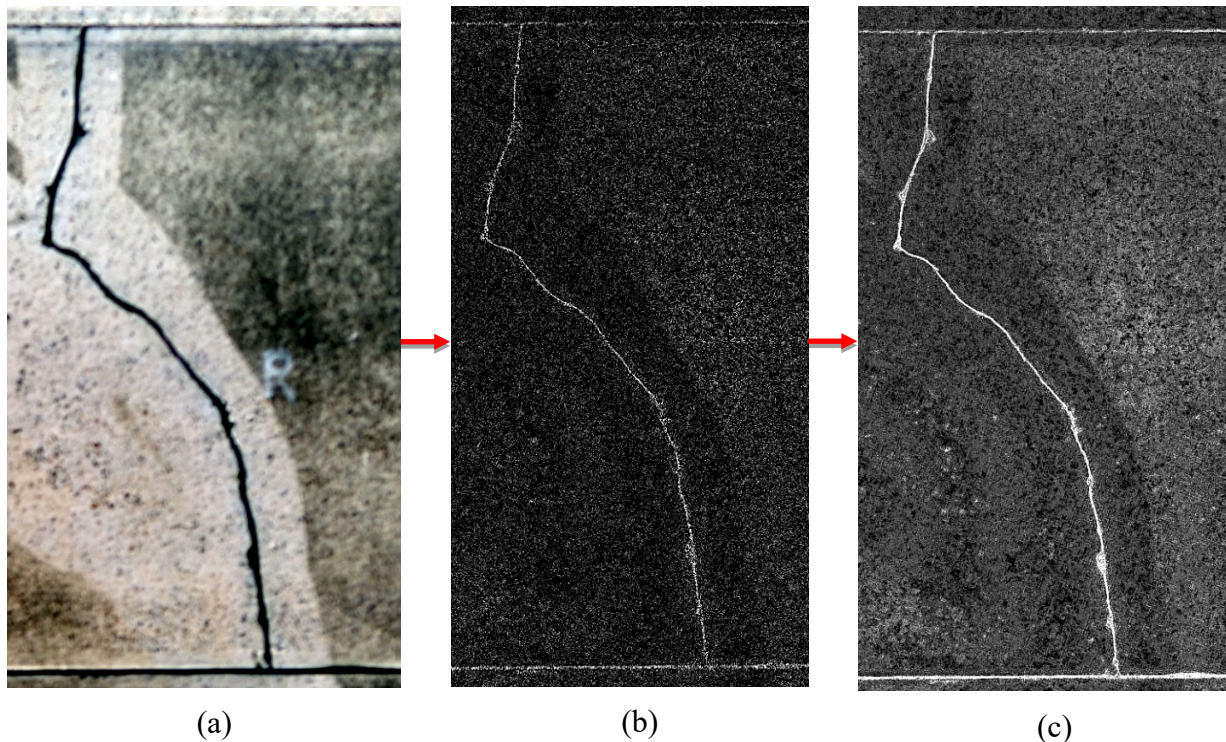
Figure 32. Lee Sigma Edge Extraction Showing the Original Image (a), with Convolutional Layer Added (b), and Incorporated Image Segmentation (c)

In Figure 32, the original RGB image (a) shows cracking. The Lee Sigma operation was utilized, and a convolutional layer was applied to smooth out the image, which reduces noise and helps define cracking (b). This layer was then incorporated into the image segmentation,[2] creating more defined image objects (c).

The Lee Sigma extraction method can only ingest a single image at a time. So, finding the correct band or combination of bands to maximize the potential of the edge extraction methods

---

[1] Lee Sigma Edge Extraction is a technique for extracting features from a digital image. It uses a mathematical algorithm to identify and extract edges in the image.

[2] Segmentation is the process of dividing an image into meaningful parts. This can be done manually by identifying regions of interest and then separating them from the rest of the image, or it can be done automatically using a variety of algorithms.

was a pivotal step. For the purpose of this research, the research team chose to use the red band as the input for the edge extraction, as this provided the best information in terms of single-band usage. The edge extraction layer was used as the primary layer for segmentation. After the creation of the edge layer, a contrast split segmentation was implemented. This segmentation method created image objects based on their dissimilarity to neighboring pixels, which was perfect for implementation on an edge layer. Figure 33 displays the final product.
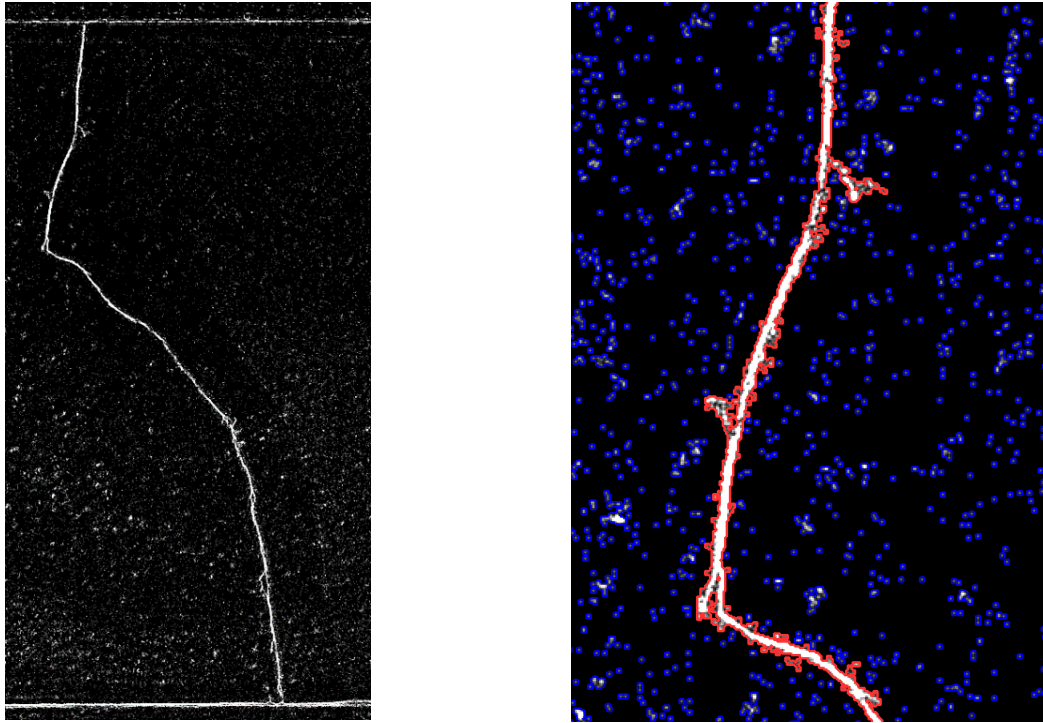
Figure 33. Contrast Split Segmentation

The contrast split segmentation resulted in a rough image object that represented cracking. Image objects were classified according to their values and refined further. During classification, only the previously created edge layer was used, since it was the layer used during segmentation. While the specific value used in classification might change slightly between different areas, the crack distresses had a significantly larger value compared to surrounding features. To refine classification, a contrast split segmentation was performed for a second time to remove excess over capture.

This first classification was a broad operation and was refined further due to over-capture. Cracks have distinct geometric features that can be used to distinguish between darker objects that might have also been picked up during the classification. First, cracks often display asymmetrical values with a large perimeter value. Second, cracks will be smaller objects when compared to their homogenized surroundings. Cracks will be present in relation to large slabs of concrete. Once classification is complete, eCognition allows for the extraction of centerlines depicted in Figure 34.
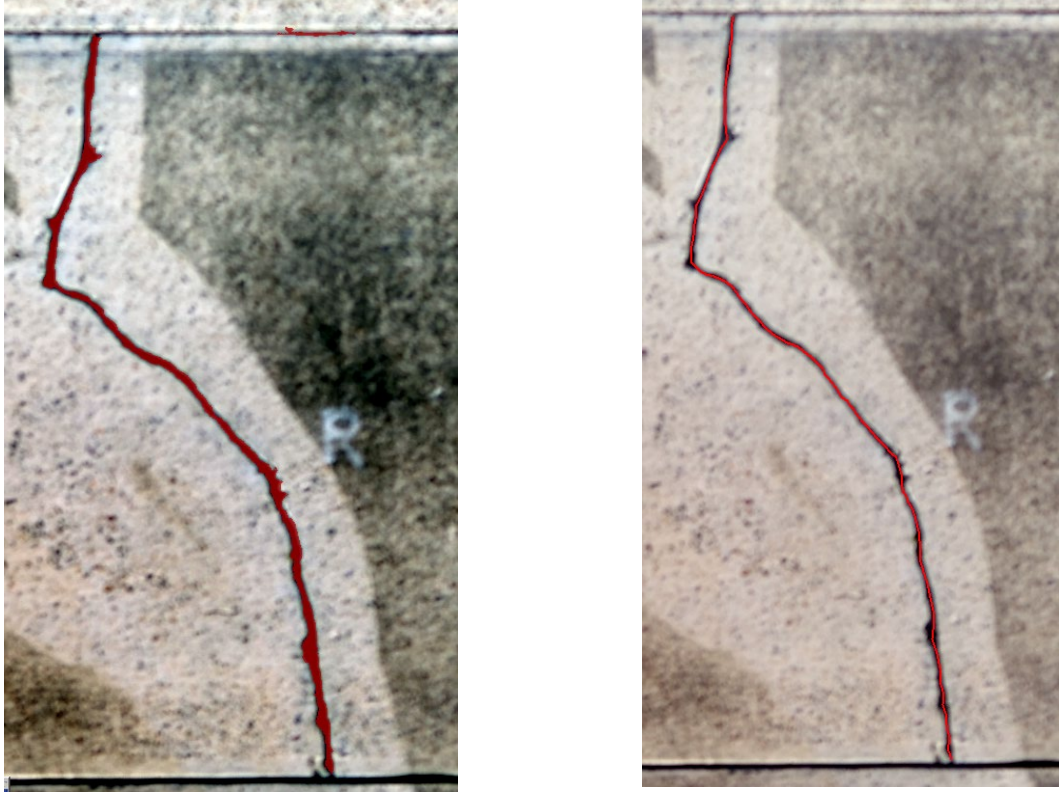
Figure 34. Shapefile Export

Missed Classifications and Partial Classifications

Unfortunately, not all cracks will be classified using this method, and manual cleanup will be necessary. Cracks that are not defined enough by image contrast are difficult to detect by this form of automated analysis. This is likely because their pixel values are still somewhat similar to their surrounding neighbors. When this happens, the whole crack is lost during classification. Also, there are cracks that have been partially sealed. It is impossible for this automated method to extract these instances of cracking without the help of a technician. Figure 35 displays both types of missed classification. Overall, out of the 34 cracks present in this subset, the automated process was able to fully extract 25 cracks, with 5 partial classifications and 4 missed classifications.
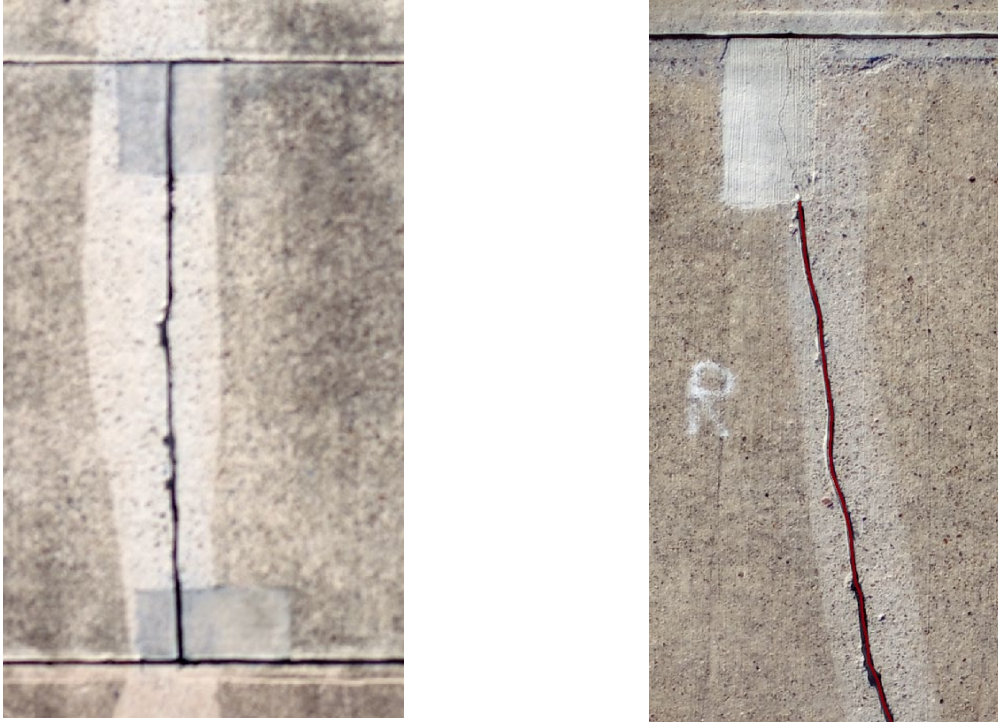
Figure 35. Missed Classification on Left, Partial on Right

4.4.5.2 Manual Distress Analysis

The research team's initial evaluation of the data revealed that the imagery collected with the M210 at 2-mm GSD was most efficient in identifying a multitude of distresses as compared to all other airframes and sensors used for data collection. This led the research team to conduct manual distress analysis of all the test areas with the imagery captured at 2-mm GSD using ESRI's ArcGIS software.

The team followed similar steps to analyze the distresses for both AC and PCC pavements and referred to the ASTM D5340-20 and the handbook of distress categories to record the data accurately. Figure 36 represents the workflow followed for the manual analysis.
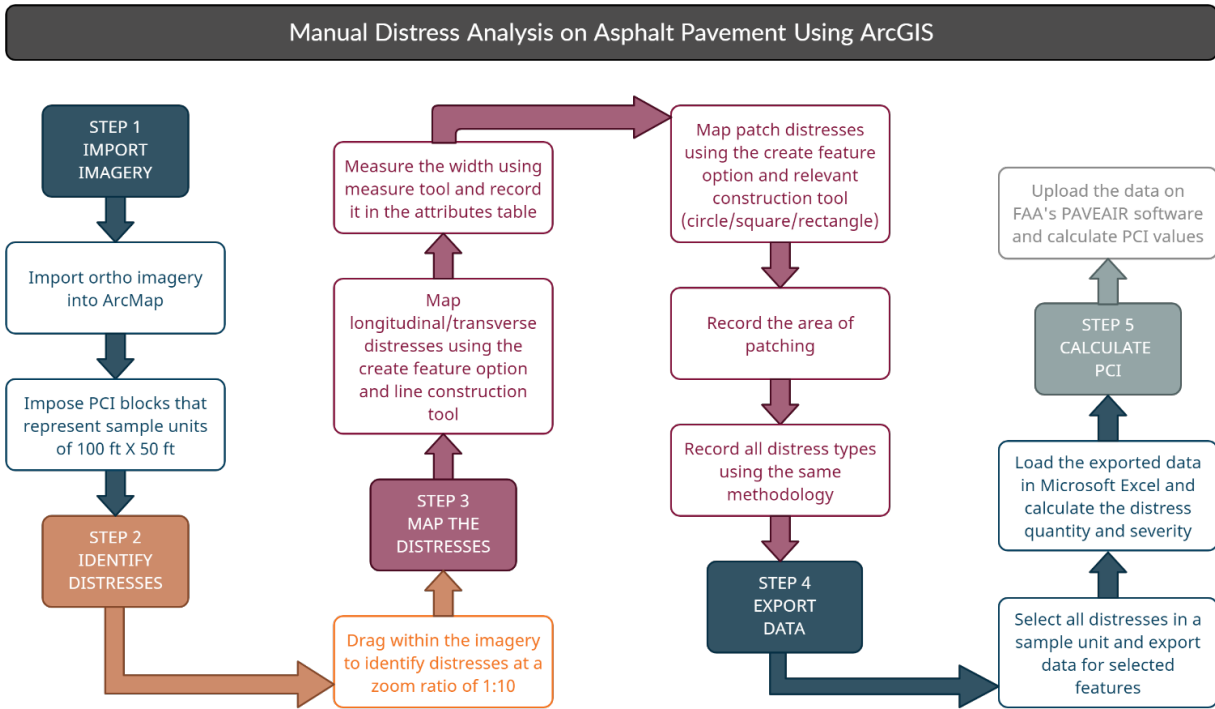
Figure 36. Manual Distress Analysis Workflow

Figure 37 shows workflow images followed from Step 1 through Step 5 of the manual analysis.
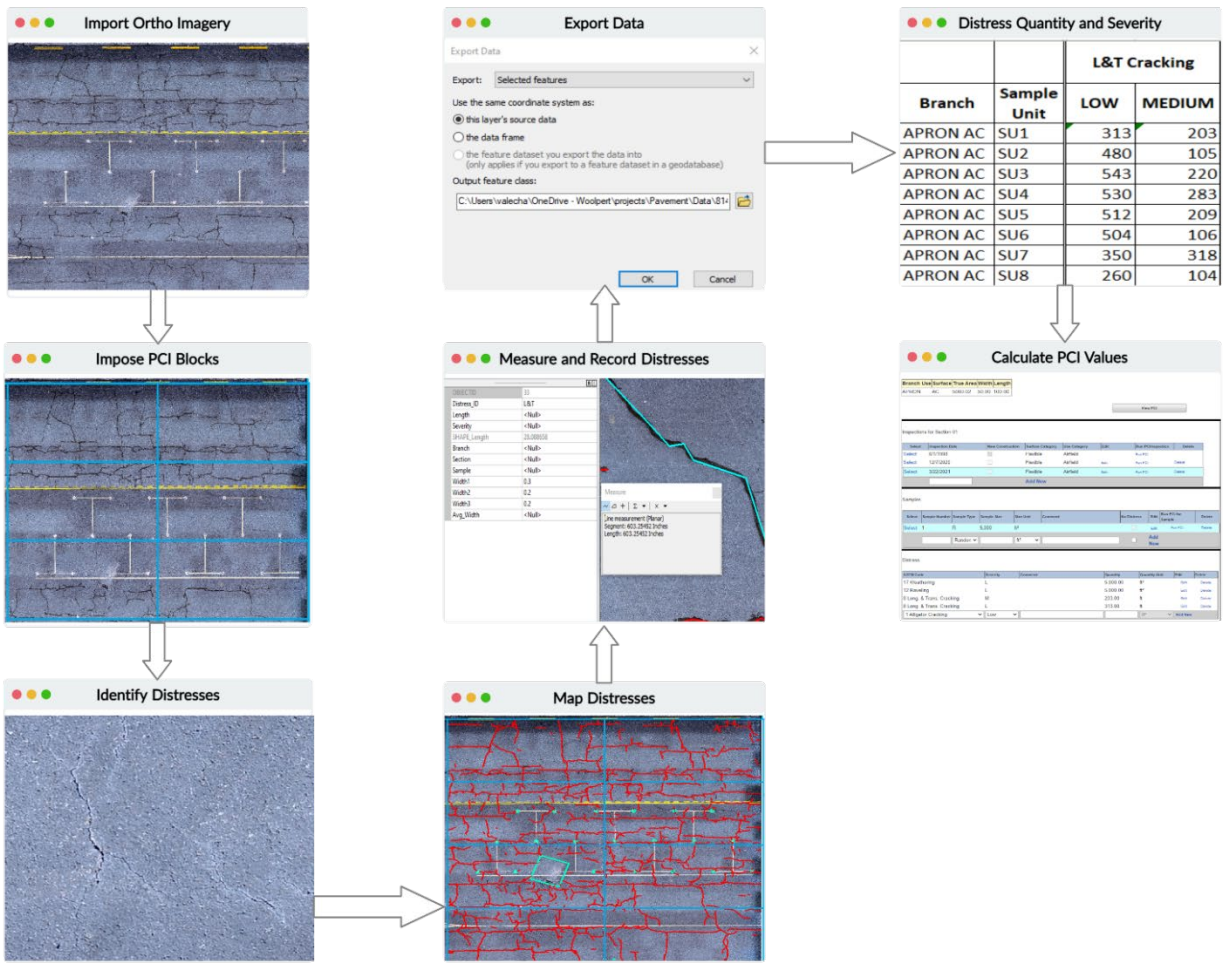
Figure 37. Manual Data Analysis Workflow Images

While the PCI rating color scheme is standard (following the PCI Rating Scale shown in Figure 2), for Tables 20 through 24, the resulting specific PCI values, as determined by FOG, DSV, and sUAS, are highlighted with a gradient (illustrated in Figure 3) to better visualize where within the limits each one rated.

Test Area 1A

For the manual analysis of Test Area 1A, which is the PCC apron, Flight 1 imagery was used. The sample size was 60 ft x 80 ft = 4,800 sq ft. The slab size was 10 ft x 20 ft = 200 sq ft. There was a total of 24 slabs in each sample unit (4 slabs across and 6 slabs down). Figure 38 illustrates these sample units.
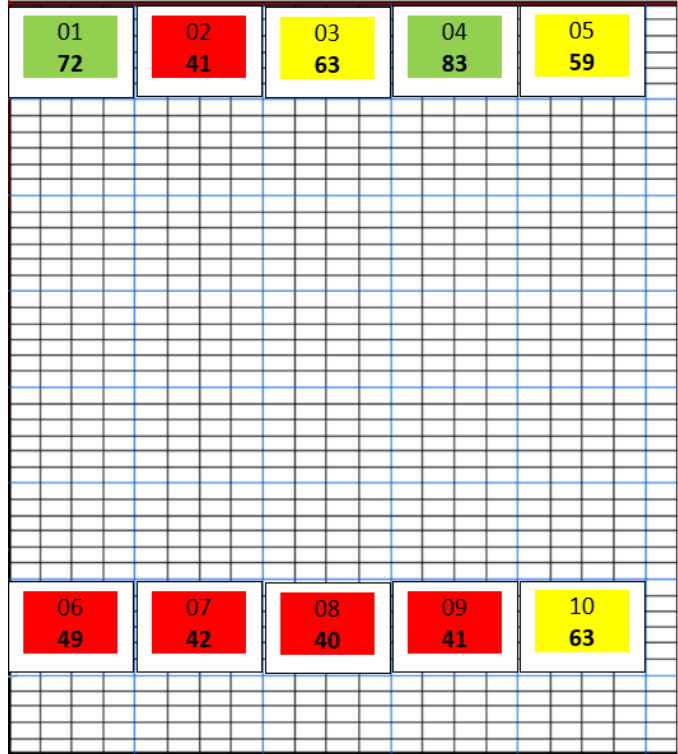
Figure 38. Sample Units of Test Area 1A at WWD (The sample units 9 and 10 were analyzed for 20 slabs [four slabs across and five slabs down] as opposed to 24 due to the missing imagery.)

Sample units illustrated in Figure 38 were analyzed, and their PCI values are shown in Table 21.

Table 21. The PCI Values of Test Area 1A at WWD

Test Area	Sample Number	FOG PCI	DSV PCI	sUAS PCI	FOG Section PCI	DSV Section PCI	sUAS Section PCI
1A	1	76	77	72	64	71	55
	2	68	82	41			
	3	72	76	63			
	4	78	81	83			
	5	72	70	59			
	6	60	78	49			
	7	46	61	42			
	8	59	53	40			
	9	59	68	41			
	10	50	62	63			

In Test Area 1A, the PCI values of FOG and DSV were greater than that of sUAS. One area of difference was joint seal damage, where the sUAS inspector reported high severity while the

FOG inspector reported low. If the sUAS severities were adjusted to low, then the PCI values would match.

Other differences include the sUAS reporting no faulting, unlike FOG, and the sUAS not reporting many shrinkage cracks, while the FOG inspection reported 24% coverage.

Test Area 1B

For the manual analysis of Test Area 1B, which is the PCC taxilane, Flight 72 imagery was used. The sample size was 50 ft x 80 ft = 4,000 sq ft. The slab size was 10 ft x 20 ft = 200 sq ft. There was a total of 20 slabs in each sample unit (4 slabs across and 5 slabs down). Figure 39 illustrates these sample units.
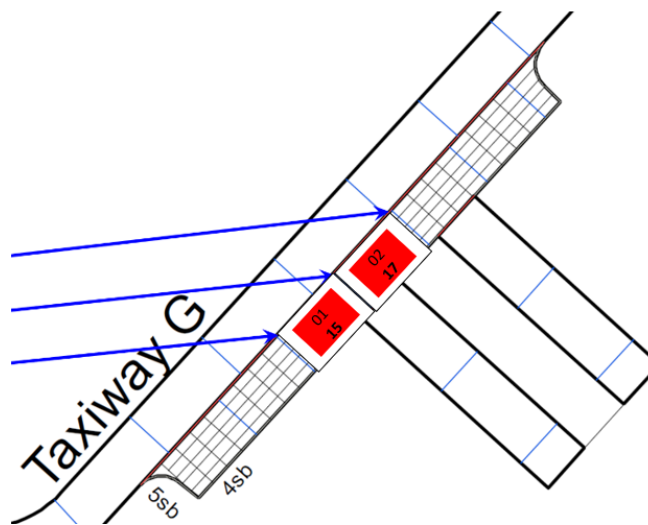
Figure 39. Sample Units of Test Area 1B at WWD

Each sample unit illustrated in Figure 39 was analyzed and their PCI values are shown in Table 22.

Table 22. The PCI Values of Test Area 1B at WWD

Test Area	Sample Number	FOG PCI	DSV PCI	sUAS PCI	FOG Section PCI	DSV Section PCI	sUAS Section PCI
1B	1	32	35	15	30	38	16
	2	29	42	17			

In Test Area 1B, the PCI values of FOG and DSV were greater than that of sUAS. Among the differences noted were that the FOG inspection did not report any high-severity linear cracking or pop-outs, while the sUAS did. In addition, the sUAS analysis reported 55% patching coverage, while the FOG analysis reported only 21% coverage.

Test Area 2A

For the manual analysis of Test Area 2A, which is the AC runway, Flight 56 imagery was used. The sample size was 50 ft x 100 ft = 5,000 sq ft. The runway sample units were divided into 10N, 10C, and 10S, with eight sample units each. Figure 40 illustrates these sample units.
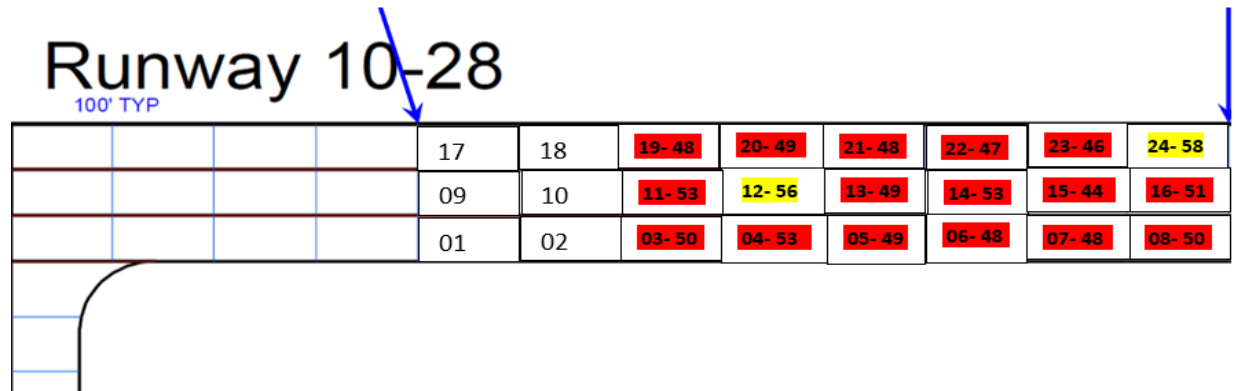
Figure 40. Sample Units of Test Area 2A at WWD (The sample units 1, 2, 9, 10, 17, and 18 were not analyzed due to the missing imagery.)

Sample units illustrated in Figure 40 were analyzed, and their PCI values are shown in Table 23.

Table 23. The PCI Values of Test Area 2A at WWD

Test Area	Sample Number	FOG PCI	DSV PCI	sUAS PCI	FOG Section PCI	DSV Section PCI	sUAS Section PCI
2A-10S	1	56	69	NA	61	70	50
	2	63	68	NA			
	3	64	71	50			
	4	66	73	53			
	5	67	73	49			
	6	65	70	48			
	7	58	67	48			
	8	47	67	50			
2A-10C	9	68	69	NA	69	67	51
	10	68	65	NA			
	11	71	67	53			
	12	71	67	56			
	13	67	64	49			
	14	68	66	53			
	15	69	66	44			
	16	70	67	51			
2A-10N	17	62	69	NA	63	66	49

Test Area	Sample Number	FOG PCI	DSV PCI	sUAS PCI	FOG Section PCI	DSV Section PCI	sUAS Section PCI
2A-10N	18	65	69	NA	63	66	49
	19	64	67	48			
	20	63	66	49			
	21	66	66	48			
	22	63	58	47			
	23	64	62	46			
	24	56	69	58			

In Test Area 2A, the sUAS PCI value was lower than both FOG and DSV. The PCI values between all three data sets would have been similar, but the sUAS analysis indicated more raveling. Section 10S showed about the same amount of L&T cracking in the FOG inspection as the sUAS. However, in Section 10C the sUAS showed more L&T cracking, while in Section 10N the FOG inspection showed more.

Test Area 2B

For the manual analysis of Test Area 2B, which is the AC taxiway, Flight 40 imagery was used. The sample unit was 70 ft x 93 ft = 6,510 sq ft. The actual sample size of the imagery was 68 ft x 91 ft = 6,188 sq ft. Figure 41 illustrates these sample units.
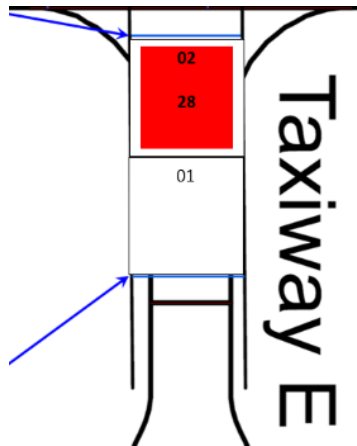
Figure 41. Sample Units of Test Area 2B at WWD
(The sample unit 1 was not analyzed due to half-missing imagery.)

Sample units illustrated in Figure 41 were analyzed, and their PCI values are shown in Table 24.

Table 24. The PCI Values of Test Area 2B at WWD

Test Area	Sample Number	FOG Sample PCI	DSV Sample PCI	UAS Sample PCI	FOG Section PCI	DSV Section PCI	UAS Section PCI
2B	1	46	55	NA	40	49	28
	2	33	44	28			

In Test Area 2B, the sUAS PCI value continued to be lower than both FOG and DSV. This was largely attributed to medium- and high-severity alligator cracking reported in the sUAS data set, where the FOG inspection rated the alligator cracking low or medium severity.

Test Area 2C

For the manual analysis of Test Area 2C, which is the AC taxiway, Flight 16 imagery was used. The sample size was 50 ft x 10 ft = 5,000 sq ft. Figure 42 illustrates these sample units.
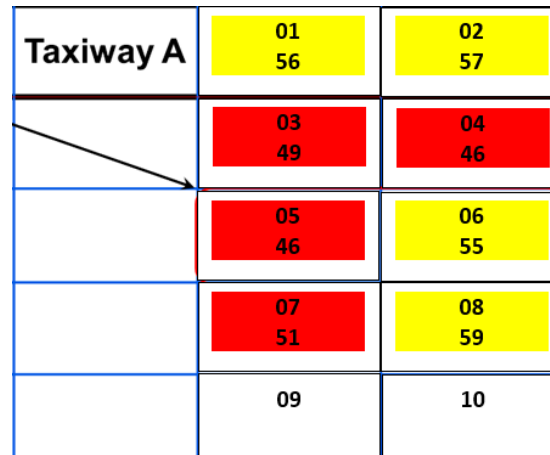
Figure 42. Sample Units of Test Area 2C at WWD (The sample units 9 and 10 were not analyzed due to half-missing imagery.)

Sample units illustrated in Figure 42 were analyzed and their PCI values are shown in Table 25.

Table 25. The PCI Values of Test Area 2C at WWD

Test Area	Sample Number	FOG Sample PCI	DSV Sample PCI	sUAS Sample PCI	FOG Section PCI	DSV Section PCI	sUAS Section PCI
2C	1	64	61	56	55	58	52
	2	41	50	57			
	3	63	64	49			
	4	53	54	46			
	5	58	62	46			

Test Area	Sample Number	FOG Sample PCI	DSV Sample PCI	sUAS Sample PCI	FOG Section PCI	DSV Section PCI	sUAS Section PCI
2C	6	54	55	55	55	58	52
	7	59	62	51			
	8	58	54	59			
	9	54	63	NA			
	10	46	53	NA			

In Test Area 2C, the sUAS PCI value was comparable to both the FOG and DSV. The FOG inspection reported no weathering. Should that distress be added, the FOG PCI value would be 51, similar to the sUAS. There were minor differences between the data sets in the reporting of cracking, with the sUAS reporting about 15% more than the FOG inspection. In addition, the sUAS did not report any shoving or swelling.

Table 26 presents a summary of PCI values of each test area/section.

Table 26. Summary of PCI Values at WWD

Test Area	FOG Section PCI	DSV Section PCI	sUAS Section PCI
1A	64.00	71.00	55.00
1B	30.00	38.00	16.00
2A–10C	69.00	67.00	51.00
2A–10N	63.00	66.00	49.00
2A–10S	61.00	70.00	50.00
2B	40.00	49.00	28.00
2C	55.00	58.00	52.00

While there were differences between FOG, DSV, and sUAS PCI results, they were not attributed to the data collection method. As the results indicate, distresses observed were the same across all platforms. Differences in PCI values were attributed to two factors: interpretation of the ASTM for PCI inspections and the method by which global distresses were observed.

During a FOG PCI inspection or a distress takeoff from digital imagery, there is room for interpretation on many of the ASTM distress severities. For example, Figure 43 displays a joint spall on the PCC apron at WWD.

Figure 43. Joint Spall at WWD

The spall depicted in Figure 43 is greater than 2 ft in length and is either a medium- or high-severity distress (ASTM International, 2020). Since there is no cracking associated with the spall, the determining factor for severity is the amount of foreign object debris (FOD) potential. The ASTM description for FOD potential for a medium-severity joint spall is "some FOD potential" and the description for high severity is "severely frayed." Depending on the pavement inspector, one might consider this spall to be high-severity due to the amount of fraying. However, another pavement inspector might consider the spall to be medium-severity because the spall has been swept and there does not appear to be a high potential for future FOD. Additionally, there is some amount of estimation occurring for other distresses. Figure 44 displays an example of the network of L&T cracking and a close-up image of one of those cracks on the AC apron at WWD.

Figure 44. Network of L&T Cracking at WWD

The L&T cracking illustrated in Figure 44 is low or medium severity; the deciding factor is whether the crack has been sealed or has a mean width less than or equal to ¼ in. for low severity and greater than ¼ in. for medium severity (according to the ASTM). During the FOG inspection, all cracks that were on the border between low and medium severity were measured with a ruler to determine if the mean width was greater than ¼ in. During the DSV and sUAS distress takeoff, all cracks were measured using an electronic measuring tool. Depending on what point a crack's width was measured and how often a crack was measured, severities for a crack could change from one inspection to the next. The FOG and sUAS inspection both resulted in an average of approximately 600 ft of L&T cracking per sample on the AC apron.

With such a large amount of cracking, efficiency and airfield exposure had to be considered during the FOG inspection, and crack width measurements had to be limited. Therefore, inspectors made estimations during FOG inspections. In the case of DSV processing, ICC allows a pavement inspector to measure the width of a crack. However, the depth and intensity images, along with a poor measuring tool, make it difficult to get an accurate measurement during DSV inspections. In many instances, the pavement inspector must rely on their experience in performing FOG inspections to visually estimate the severity of a crack. In contrast, the 2-mm GSD from the sUAS allows crack widths to be accurately measured, and more measurements can be made to better identify the distress severity.

Global distress ratings such as weathering, raveling, and joint seal damage also differ between data collection platforms. FOG inspectors can physically touch and test these distresses in the field, but producing a rating from digital imagery is more difficult. In the instance of the DSV, the pavement inspector used field notes to quantify global distresses that were collected by the DSV operator. An attempt to quantify these distresses was made from the sUAS imagery and is reflected in the analysis. Consequently, the distresses and severities differ from the FOG and

DSV. If field notes were used for the sUAS ratings, the standard deviation of PCI values between sUAS and FOG inspection was decreased.

In summary, the FOG, DSV, and sUAS distress takeoffs were all performed by different pavement inspectors. In instances when the pavement inspector provided judgement, the FOG and DSV inspectors leaned towards the lower severities, while the sUAS pavement inspector leaned towards higher severities. The examples given in Figures 43 and 44 would require the same maintenance and rehabilitation, regardless of their severity, and the differences in severities resulted in differences between PCI values.

4.5 PHASE 1 SUMMARY

The testing and research performed during Phase 1 across multiple areas at WWD led to the conclusions presented in Table 27.

Table 27. Summary Conclusions from Phase 1 Testing

	The M210 at 2-mm GSD was most efficient in identifying a multitude of distresses, as compared to all other airframes and sensors used for data collection. Therefore, any future 2-mm GSD data collected by the DJI M210 RTK v2 and X7-35mm sensor in this report will be referred to as M210. However, this platform—along with all the platforms tested during this research effort—had inherent limitations with collecting data at the recommended GSD.
	Slow shutter speeds could cause nadir imagery to appear blurry. Shadows from buildings could result in lost data if shutter speed is not fast enough, making the analysis and evaluation more difficult.
	Distresses observed were the same across all platforms. Differences in PCI values were attributed to two factors: interpretation of the ASTM for PCI inspections and the method by which global distresses were observed.
	Crack widths could be accurately measured using sUAS-derived imagery, and several measurements could be made to better identify the distress severity in an office setting.

4.5.1 Small Unmanned Aircraft Systems Data Capture Interim Recommendations

Based on the field findings at the conclusion of Phase 1 testing, the following recommendations were made to improve the efficiency and effectiveness of data capture practices:

- Extending the flight area boundaries beyond the edges of the test area will ensure full image coverage.

- DJI systems can "hover and capture" at low-altitude missions but need to be forced into "continuous capture" mode due to start-stop movements being too aggressive during "hover and capture."
- DJI sensors can drift on the yaw axis during missions; the pilot needs to be aware of this tendency and correct as needed.
- Camera yaw should be in line with aircraft orientation.
- The camera should be focused before the mission begins.
- Focus should be set and locked through the duration of the operation.
- Metering mode should be set to "Center Weighted Average" when able.
- Camera shutter speed should be fast enough to reduce motion blur.
- Camera feed and camera settings should be monitored throughout the mission.
- The live feed can lag and display a poor-quality image, therefore, the data must be validated in the field on a separate device, such as a laptop.
- Thermal imagery lacked the spatial resolution to accurately assess pavement distresses and was therefore dismissed from future testing.

4.5.2 Small Unmanned Aircraft Systems Data Processing Interim Recommendations

At the conclusion of Phase 1 testing, the recommendation for orthomosaic generation was to use a traditional three-step workflow as follows:

1. Tie point/pass point generation and development, a bundle block adjustment, camera calibration, and ground control measurement
2. Dense point cloud and mesh generation, setting the foundation for the orthomosaic
3. Orthomosaic generation and review

4.5.3 Small Unmanned Aircraft Systems Data Analysis and Evaluation Interim Recommendations

At the conclusion of Phase 1 testing, the recommendation for analyzing the processed orthomosaic images was to utilize the following workflow:

- Impose the PCI blocks on to the ortho before starting the analysis. These blocks represent the sample units in a section.
- Identify distresses with a zoom ratio of 1:10 within the desired software.
- Zoom in farther on imagery to identify the accurate widths of identified cracks.
- Record all the distress-related data (e.g., distress type, severity, width/area, sample unit, slab number) within the attributes for consistency. This also reduces the time required to clean up the data after exporting it.

4.6 RECOMMENDATIONS FOR PHASE 2 TESTING

In addition to the interim recommendations, the research team made the following recommendations for Phase 2 testing:

- Test upgraded systems that allow longer flight times while carrying more robust payloads for more efficient data capture.
- Validate that 2-mm GSD imagery is adequate for sUAS-based pavement distress analysis.
- Reduce overlap settings on 2-mm GSD imagery and assess the quality of the resulting orthomosaic to improve operational efficiencies.
- Test larger GSD imagery on more robust payloads to determine differences in resolution while introducing operational efficiencies.
- Reduce overlap settings on 3-mm GSD imagery and assess the quality of the resulting orthomosaic to improve operational efficiencies.
- Test the efficacy of reducing or removing the number of ground control points (GCPs).
- Test additional sensors (i.e., LiDAR) to identify distresses that cannot be captured with RGB or thermal sensors.
- Quantify the spatial resolution of the test platforms by evaluating resolving power.

5. AIRPORT TEST PROCEDURES AND RESULTS—PHASE 2

The recommendations made during Phase 1 were tested and validated in Phase 2. Phase 2 sought to implement operational efficiencies of the data collection to ensure practicality. Once the research team selected airports and test sites, FOG inspections were executed at each test site and used as control data. DSV inspections complemented the FOG inspections at WWD, Savannah/Hilton Head International Airport (SAV), and Cincinnati/Northern Kentucky International Airport (CVG), followed by sUAS data collection at all test sites. DSV inspections were not conducted at Grosse Ile Municipal Airport (ONZ) or Custer Airport (TTF).

5.1 AIRPORT SELECTION

Phase 2 testing was conducted at five airports: WWD, SAV, CVG, ONZ, and TTF. Airport selection during Phase 2 included locations that offer different pavement surface types, varying pavement ages, unique distresses (not previously identified), and differing accessibility to the airport. The selected airports also encountered diverse environmental conditions throughout the year. Airport selection was conducted in four stages:

Stage 1. WWD served as a continued testing location from Phase 1.

Stage 2. SAV was chosen due to the research team's existing relationship and approved airspace authorization with the airport. SAV is a Class C airspace and provided opportunity to identify additional pavement distresses that were not previously identified.

Stage 3. CVG is in close proximity to Woolpert headquarters, which allowed the research team to mobilize additional sensors for testing. CVG also has an established relationship with the research team and is located in Class B airspace.

Stage 4. ONZ and TTF were selected to validate operational efficiency parameters. ONZ and TTF also offered new distress types due to environmental conditions.

5.2 SMALL UNMANNED AIRCRAFT AIRFRAMES AND SENSORS

A variety of additional airframes and sensors were tested during Phase 2. Table 28 shows a summary of these additional airframes, sensors, GSDs, data types, and software packages used in Phase 2.

Table 28. Summary of Systems and Software Used in Phase 2

Airframe	Sensor	GSD Parameters (mm)	Test Location	Data Type	Image Processing	Data Analysis
M210	X7-35mm	2, 3	WWD, SAV, CVG, ONZ, TTF	RGB	Pix4D Mapper	Esri ArcMap, FAA PAVEAIR
Wingtra One	Sony RX1R-II	8	WWD			
HAMR	Cannon EOS 5DS	4	WWD			
M210	Rock R2A	N/A	CVG	LiDAR	Rock Cloud	Global Mapper, ESRI

HAMR = Hybrid Advanced Multi-Rotor

Rock Robotic R2A LiDAR, shown in Figure 45, can emit 240,000 pulses per second and is equipped with a Sony A5100 with a 16mm lens for point cloud colorization. This sensor can be carried by a number of airframes, but this study utilized the M210, as that airframe was already being used to test the Zenmuse X7.

Figure 45. Rock Robotic R2A

Wingtra WingtraOne, shown in Figure 46, was selected due to its unique hybrid system, which allows for VTOL operations for takeoff and landing and transitions into fixed-wing for flight. This system is equipped with a Sony RX1R-II; a full frame, 42-megapixel camera that can

achieve high resolutions even at high altitudes. The Wingtra WingtraOne will herein be referred to as Wingtra.

(a)   (b)

Figure 46. Wingtra One (a) with RX1R-II (b)

Hybrid Advanced Multi-Rotor (HAMR™), shown in Figure 47, uses a full-frame DSLR (Digital Single-Lens Reflex) camera, the Canon EOS 5DS with a 24mm lens. The HAMR system combines electric and combustion power sources to sustain flight. The HAMR airframe was chosen to evaluate the viability of using a large, heavier, fuel-powered aircraft capable of long endurance flight for data collection, thereby increasing operational efficiencies by eliminating the need for repeated landings.

Figure 47. The HAMR Airframe (a) with Canon EOS 5DS (b)

5.3 TESTING METHODOLOGY

The research team developed a comprehensive methodology for Phase 2 testing at WWD, SAV, CVG, ONZ, and TTF before mobilizing field crews to the test sites. Using the test areas at the airports selected for Phase 2, the research continued validation of previous findings, introduced operational efficiencies with data collection, and attempted to capture ASTM pavement distresses not previously identified during Phase 1. Table 29 shows a breakdown of the testing rationale performed at each airport.

Table 29. Phase 2 Testing Methodology

Phase	Airport	Test Rationale	Test Area
2.1	WWD	Operationally efficient system tests (HAMR/Wingtra)	Runway 10/28
		Operationally efficient low overlap tests (DJI)	WWD Area 2C (GA Asphalt Apron)
2.2	SAV	Validate 2-mm GSD imagery (M210) No RTK/standalone GPS, no ground control	West End Runway 10/28 and Taxiway GA4
2.3	CVG	Operationally efficient low-overlap tests (M210 2-mm GSD), no ground control	Remote Aircraft Parking and Apron 1 South
		Operationally efficient low-overlap tests and validation (M210 3-mm GSD), no ground control	
		LiDAR data collection, no ground control	
2.4	ONZ	Validation Testing of 2-mm GSD imagery derived via an M210, no ground control	North half of Runway 17/35 and Taxiway A
	TTF	Validation Testing of 2-mm GSD imagery derived via an M210, no ground control	Middle half of Runway 03/31 and Taxiway A, connector A2 and A3

5.4 STAGE 1—WWD

This section expands on the testing performed at WWD including test areas, control data, the use of ground control, sUAS data collection parameters, data processing workflows, and data analysis for PCI.

5.4.1 Test Areas

The test areas at WWD were the asphalt Runway 10/28 (4,998 ft x 150 ft) and a GA asphalt apron. These test areas were also previously evaluated as Test Areas 2A and 2C during Phase 1 of this research effort. When possible, the research team purposely overflew these test areas to ensure full coverage across the edges of the pavement. This practice was established as a lesson learned from Phase 1. Data collection during this best practice resulted in a minimal loss of data around the test area boundaries.

Figures 48 and 49 illustrate the two test areas selected for data collection.

Figure 48. Full Runway 10/28 at WWD (Capture limits in yellow, test limits in red.)
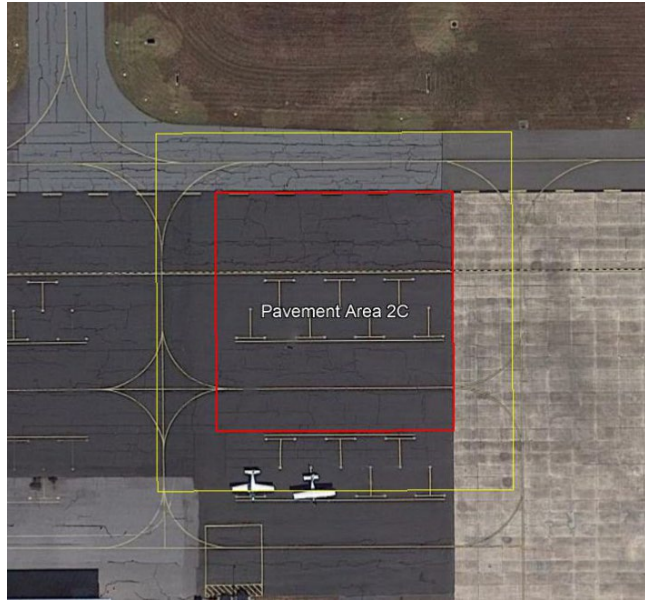
Figure 49. Asphalt Apron Area at WWD (Capture limits in yellow, test limits in red.)

5.4.2 Control Data—FOG and DSV

Control data sets were collected through FOG and DSV surveys. Phase 1 and Phase 2 sUAS data collections were performed within 2 months of one another, and the two test sections that were evaluated in Phase 2 were the same as two of the test sections evaluated in Phase 1. Therefore, there was no need for additional FOG or DSV data collection. Field notes of global and elevation distresses were used to supplement the DSV data.

The summary of field notes is as follows:

- Runway 10/28 (AC Pavement)—100% low-severity weathering.
- GA Apron (AC Pavement)—Low-severity raveling on entire apron. There is low-severity shoving within 2 ft of the PCC GA Apron joint. In this area, the raveling is medium severity.

Generally, FOG and DSV PCI data were close in comparison, with the DSV PCI being slightly higher than that of the FOG PCI. This was attributed to a minor loss in total quantity of cracking, difficulty in determining crack widths, and inability to observe global and elevation distresses while performing a distress takeoff from the DSV's intensity and depth imagery.

5.4.3 Ground Control

GCPs were RTK surveyed using a Trimble R8-3 GNSS receiver connected to a Virtual Reference Station (VRS). These data were used in the processing stage to ensure that the data sets were spatially accurate. Figures 50 and 51 show the numbers and locations of each point.

Figure 50. Eighteen GCP Locations over the Runway 10/28 at WWD

Figure 51. Four GCP Locations over the GA Apron at WWD

5.4.4 Small Unmanned Aircraft System Data Collection Parameters

During Phase 2 data collection at WWD, the research team used two additional systems to collect imagery over the runway: the Wingtra and the HAMR. The Wingtra flight utilized a dual frequency GNSS receiver and used PPK for accurate airframe positioning. The M210 flights utilized a dual frequency GNSS receiver and used RTK for accurate airframe positioning. The HAMR does not have RTK or PPK capabilities and it's autonomous GPS position was used. The data collected at GA Asphalt Apron area were refined from recommendations in Phase 1 and utilized an M210 at 2-mm GSD. While maintaining the minimum GSD requirements (2 mm) from Phase 1, Phase 2 testing introduced lower overlap settings to assess operational efficiencies. Table 30 presents the data collection parameters at WWD.

Table 30. Data Collection Parameters for sUAS at WWD

Flight #	Test Area	Airframe	Sensor	Data Type	Overlap (Forward/Side)	Altitude (ft)	GSD (mm)	Actual Flight Time (min.)	Actual # Photos
1	RWY 10/28	Wingtra	Sony RXIR-II	RGB	80/60	172	8	10	414

Flight #	Test Area	Airframe	Sensor	Data Type	Overlap (Forward/Side)	Altitude (ft)	GSD (mm)	Actual Flight Time (min.)	Actual # Photos
2	RWY 10/28	HAMR	Cannon EOS 5DS		80/60	75	4	30	1,323
3*	2C (GA Apron)	HAMR	Cannon EOS 5DS	RGB	80 / 60	N/A	2	0	0
4	2C (GA Apron)	M210	X7- 35mm		60/60	59.59	2	29	557
5	2C (GA Apron)	M210	X7- 35mm		50/50	59.59	2	15	336
6	2C (GA Apron)	M210	X7- 35mm		40/40	59.59	2	10	241
					Total Flying Time	(Minutes)		94	

Flight 3 was not collected due to equipment issues.

A total of five missions were successfully executed as part of data collection in Stage 1 at WWD. All flights collected RGB imagery. Operationally, the Wingtra could not fly lower due to manufacturer restriction; therefore, minimum GSD was 8 mm. The HAMR system appeared to have focus issues, which caused the imagery to be of insufficient quality. The integrated camera requires manual settings on the ground prior to flight. Therefore, the research team determined that a live view of the camera and in-flight camera adjustments are valuable assets while conducting sUAS-based pavement inspections.

5.4.5 Resolving Power Test

Throughout this research effort, the research team leveraged GSD values to compare the resolution of imagery collected by different sensors. GSD, however, is not the sole factor that indicates the resolving power of a sensor lens combination. The actual resolving power (the smallest feature able to be distinctly captured) of a camera system depends on many variables, including not only the GSD but also lens sharpness (or lack thereof), the camera's electronics (which can introduce image compression and gamma correction artifacts), missed focus, and the stability of the airframe and its sensor. Higher sensor pixel densities alone do not provide any added value if the system as a whole produces images that are not sharp enough to resolve fine features.

Early in the research, the team determined that a 2-mm GSD, as collected by the M210, was sufficient in identifying fine pavement surface features. For the purpose of repeatability and duplication of the results with a different airframe and sensor, the research team attempted to turn this GSD into a more objective number describing the resolving power of the imagery by using an ISO-12233:2000 high-contrast test chart. The research team printed the test chart (shown in Figure 52) at 24 in. x 48 in. and placed it on the ground during imagery acquisition.
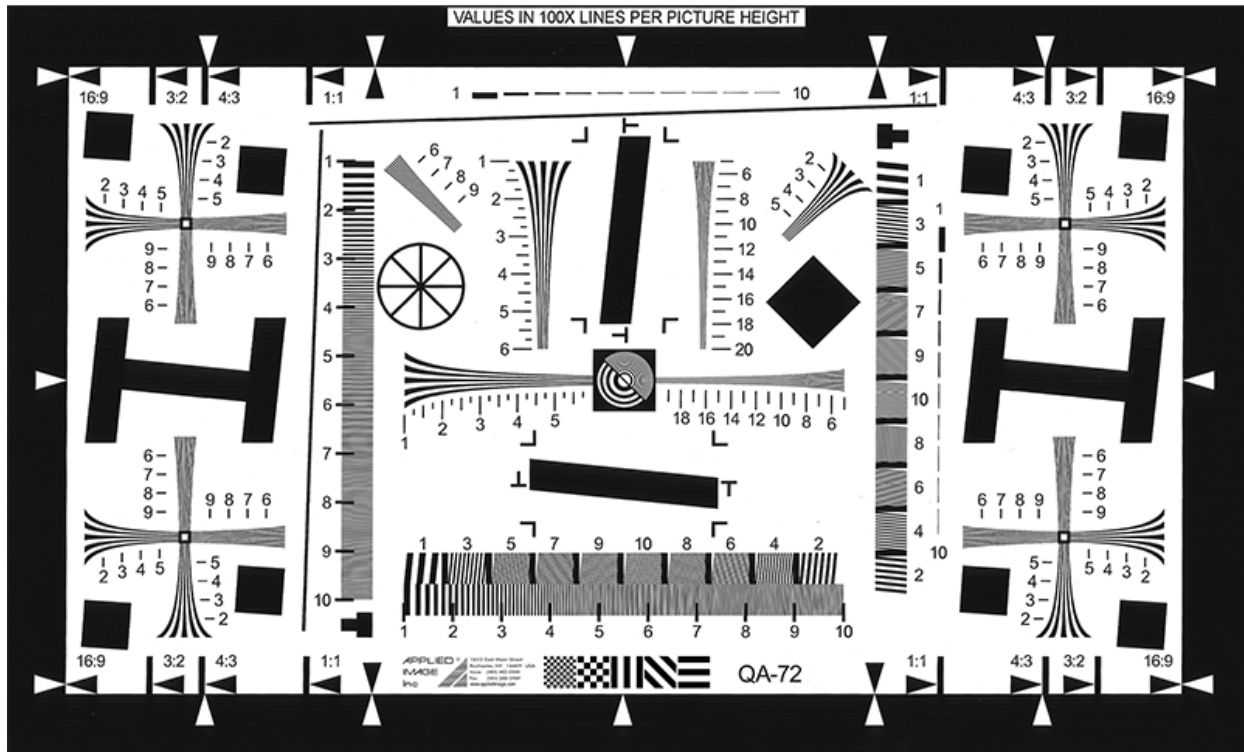
Figure 52. Test Chart from ISO-12233:2000

Subsequent analysis of the test chart as captured in the field shows that most of the line samples start to become indistinguishable at or near 200 lines per picture height. With a picture height of 24 in. as measured on the ground (approximately 610 mm), the analysis suggested that the M210 at 2-mm GSD has the ability to resolve high contrast features down to approximately 3 mm in size.

Figure 53 illustrates the test chart that was placed in field at WWD while collecting imagery with the M210 at a GSD of 2 mm and Figure 54 illustrates a closeup of Figure 53.
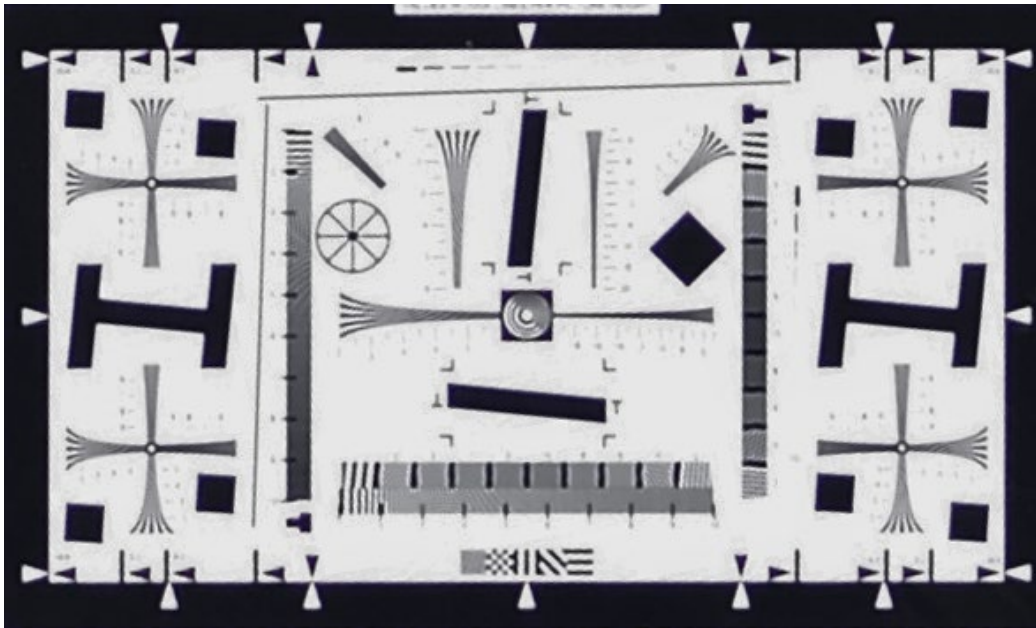
Figure 53. Test Chart from ISO-12233:2000 at WWD at 2-mm GSD

Figure 54. Closeup of Figure 53 Showing the Resolution Limit at 3 mm

This test was not duplicated for any other sensors used throughout this research.

5.4.6 Small Unmanned Aircraft System Data Processing

The processing team successfully generated orthomosaics with no loss of data or stitching artifacts when the overlap settings were reduced to 40/40. Table 31 presents the results of processed orthomosaics and their viability for distress analysis.

Table 31. Processing Results for sUAS Data at WWD

Flight Number	System	Overlap	GSD (mm)	Successful Orthomosaic	Acceptability for Analysis
1	Wingtra	80/60	8	✓	✓
2	HAMR	80/60	4	✓	✓
4*	M210	60/60	2	✓	✓
5*	M210	50/50	2	✓	✓
6*	M210	40/40	2	✓	✓

*Color banding was identified in the imagery of Flights 4, 5, and 6. Banding was a result of auto exposure during imagery collection while transitioning from a bright, concrete pavement to darker asphalt. This does not affect the resulting pavement distress analysis.

5.4.7 Small Unmanned Aircraft System Data Analysis and Evaluation

Full Runway 10/28

For the purposes of evaluating operational times, the capture limits during Phase 2 encompassed the entire runway 10/28 at WWD. However, the test limits only included three sections: 10N, 10C, and 10S, with eight sample units each as illustrated in Figure 55. Each sample unit was 50 ft x 100 ft (5,000 sq ft).
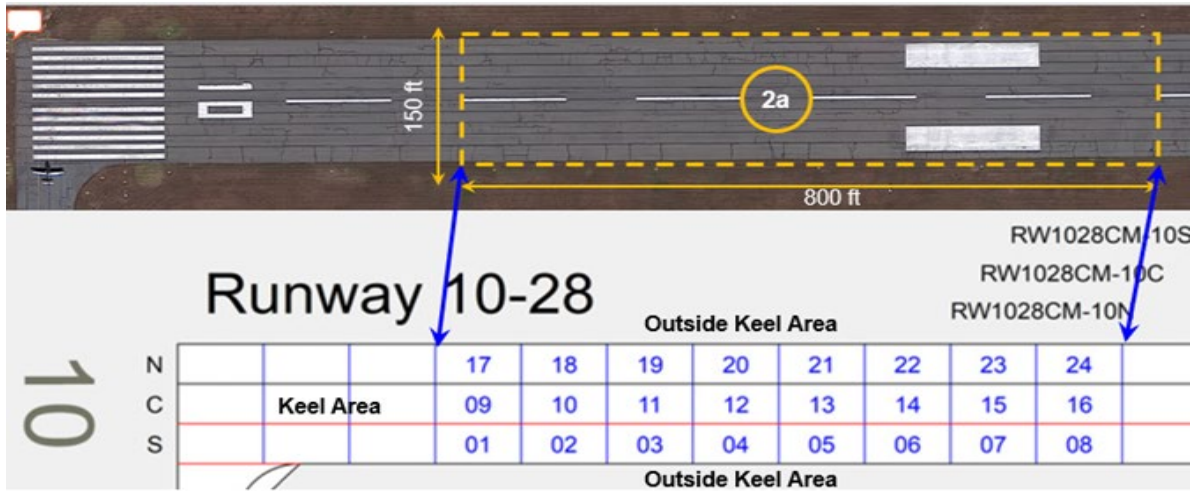
Figure 55. Sample Units of Runway 10/28 at WWD

Each sample unit illustrated in Figure 55 was analyzed, and their PCI values are shown in Table 32.

Table 32. The PCI Values of Runway 10/28 at WWD

Section	Sample Number	FOG PCI	DSV PCI	sUAS PCI (Wingtra)	sUAS PCI (HAMR)	FOG Section PCI	DSV Section PCI	sUAS Section PCI (Wingtra)	sUAS Section PCI (HAMR)
10N	17	62	69	51-66	55-69	63	66	51-66	53-68
	18	65	68	52-67	55-69				
	19	64	67	52-66	54-68				
	20	63	66	50-66	51-66				
	21	66	66	51-66	54-68				
	22	63	58	50-65	52-66				
	23	64	62	46-62	51-66				
	24	56	69	56-70	57-71				
10C	9	68	69	54-68	54-68	69	67	54-68	56-70
	10	68	65	55-69	56-70				
	11	71	67	56-70	58-72				
	12	71	67	55-69	58-72				
	13	67	64	52-67	54-69				
	14	68	66	53-68	56-70				
	15	69	66	52-67	55-69				
	16	69	67	52-67	59-72				
10S	1	56	69	53-67	54-68	60	70	54-68	55-69
	2	53	68	58-71	57-70				
	3	64	71	54-68	54-68				
	4	66	73	56-70	57-70				
	5	67	73	54-68	56-70				
	6	65	70	53-68	54-69				
	7	58	67	53-68	56-69				
	8	47	67	53-68	54-68				

Note: Full runway data were not analyzed and were only collected for full-scale sUAS operation evaluation.

In addition to field findings for newly introduced systems, the runway analysis indicated that the resolutions of Flights 1 and 2 were not adequate in identifying 100% of the low-severity cracking. Additionally, crack widths were not accurately measured when performing the sUAS distress takeoff, due to the lower resolution and lack of image clarity. Figure 56 shows a comparison of Flight 1 and Flight 2 at WWD.

Flight 1 - WingtraOne | Sony RXIR-II |
80/60 Overlap | 8-mm GSD
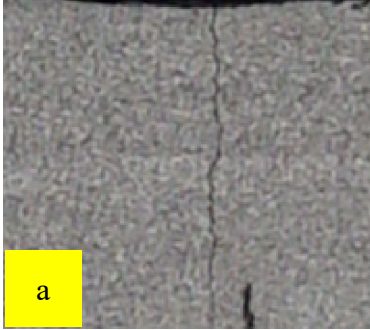
Flight 2 - HAMR | Cannon EOR 5DS |
80/60 Overlap | 4-mm GSD
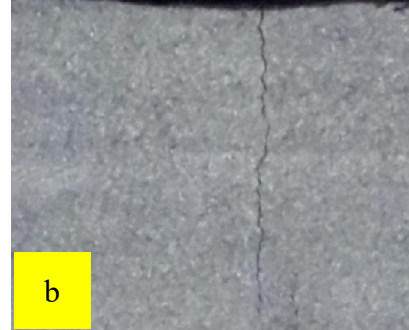
Figure 56. Flight 1 (a) vs Flight 2 (b) at WWD

Assumptions could have been made to estimate crack severities, such as rating cracks with apparent crack seal as low severity and the remaining cracking as medium severity. However, due to the objective of this research effort, this was not considered. Instead, the research team calculated PCI ranges based on what was physically measured and quantified during the distress takeoff. The top end of the PCI range considers all of the L&T cracking as low severity, and the bottom end of the PCI range considers all of the L&T cracking as medium severity. Therefore, due to low-quality imagery and its inadequacy for analysis, Wingtra and HAMR were not considered for further testing.

GA Asphalt Apron Area 2C

The sample size was 50 ft x 100 ft (5,000 sq ft), and eight samples were analyzed (as illustrated in Figure 57). For purposes of data comparison, sample units 9 and 10 were not analyzed in Phase 2 due to the lack of imagery in Phase 1 data.
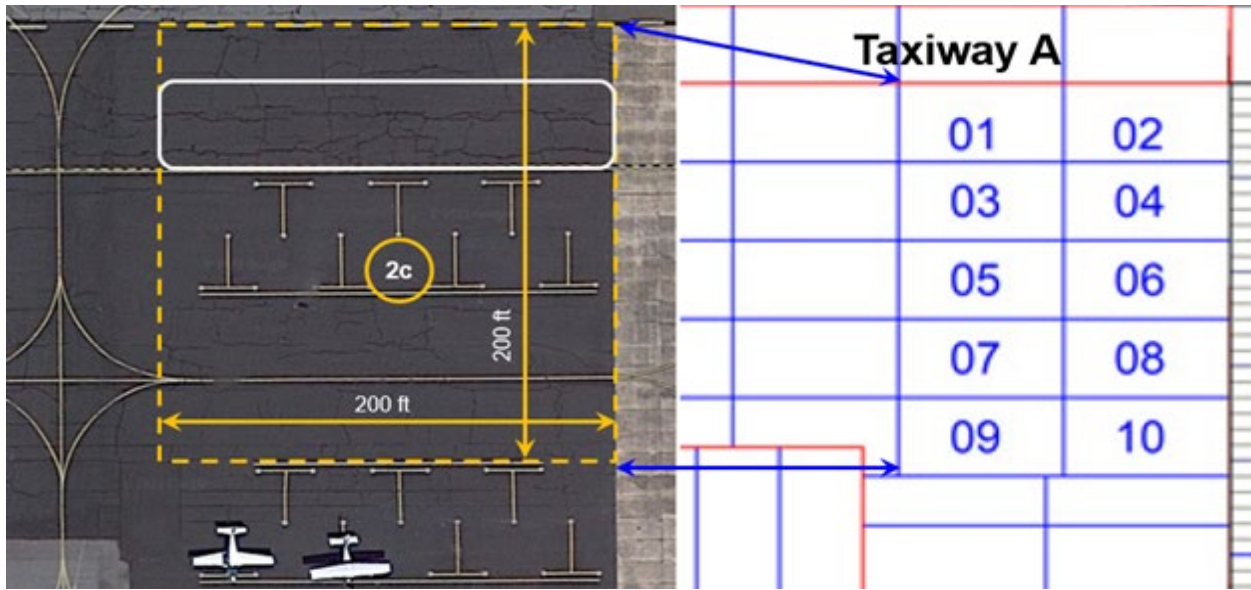
Figure 57. Sample Units of GA Asphalt Apron at WWD

Table 33 shows the PCI values of analyzed sample units.

Table 33. The PCI Values of Asphalt Apron at WWD

Section	Sample Number	FOG PCI	DSV PCI	sUAS PCI (60/60)	sUAS PCI (50/50)	sUAS PCI (40/40)	FOG Section PCI	DSV Section PCI	sUAS Section PCI (60/60)	sUAS Section PCI (50/50)	sUAS Section PCI (40/40)
30	1	64	61	59	60	61	56	58	51	52	50
	2	41	50	49	50	41					
	3	63	64	48	48	49					
	4	53	54	50	53	47					
	5	58	62	50	51	48					
	6	54	55	48	50	49					
	7	59	62	49	50	51					
	8	58	54	55	57	57					

The GA Asphalt Apron was an aged pavement with a 10+-year-old surface seal and crack seal applied. As shown in Figure 58, these aged/weathered maintenance and rehabilitation (M&R) applications have deteriorated and made observations of the excessive amounts of cracking difficult to track in the field.

Figure 58. Asphalt Apron Pavement Deterioration at WWD

Flights 4, 5, and 6 demonstrated the ability to accurately perform a PCI distress survey while increasing operational efficiencies by reducing the amount of overlap between the images. The PCI values for these flights were all within 2 points of one another and averaged to be 5 points lower than the FOG control data set. While there was an 8% reduction in total amount of L&T cracking from Flight 4 to Flight 5 and an additional 2% reduction from Flight 5 to Flight 6, all three flights were able to identify significantly more cracking than was observed in the FOG survey. As shown in Figure 59, the slight variance between the sUAS flights did not affect overall PCIs, but rather, small differences could be attributed to where (or at how many locations) a pavement inspector measured a crack's width to determine its severity.

Flight 4 - DJI M210 RTK v2 | X7-35mm | 60/60 Overlap | 2-mm GSD **Flight 5 - DJI M210 RTK v2 | X7-35mm | 50/50 Overlap | 2-mm GSD** **Flight 6 - DJI M210 RTK v2 | X7-35mm | 40/40 Overlap | 2-mm GSD**
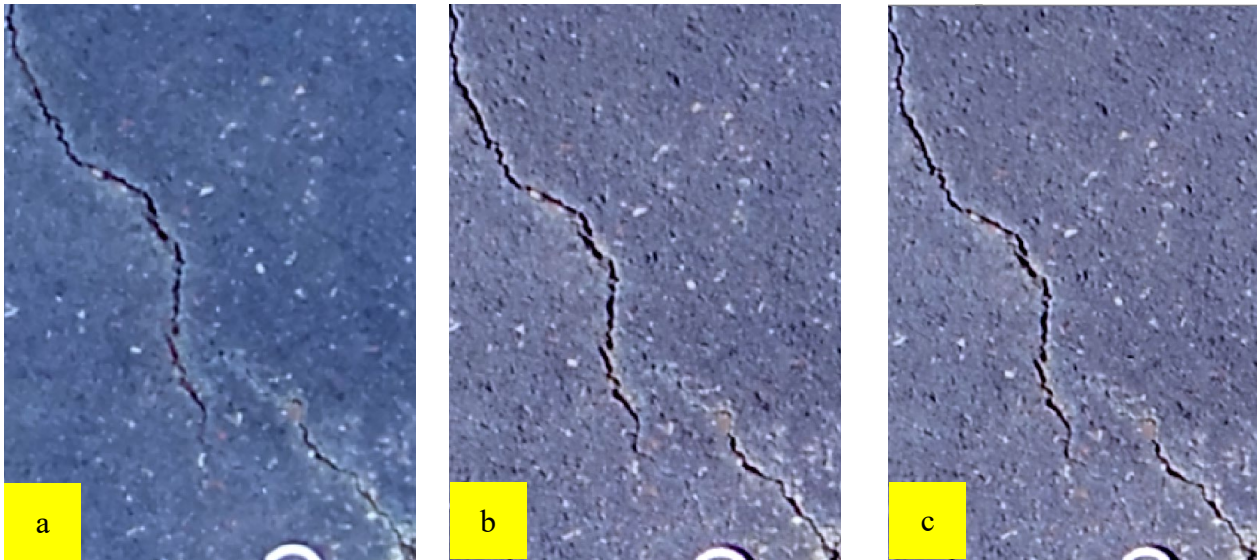
Figure 59. Flight 4 (a) vs Flight 5 (b) vs Flight 6 (c) at WWD

In conclusion, there were no identifiable functional differences between the 60/60, 50/50, and 40/40 overlaps, and the differences in PCI values are indicative of inspector differences and fall within the ASTM standard deviation. The key highlight from this phase of data collection at WWD was the added benefit of being able to inspect an area of pavement in an office setting with such precision and certainty that distresses are not missed.

Figure 60 demonstrates how difficult it would be to accurately track the quantity of cracking in the field. The ability to digitize and track distresses demonstrates superiority over manually measuring distresses in the field or performing a distress takeoff from the DSV laser-based imagery.
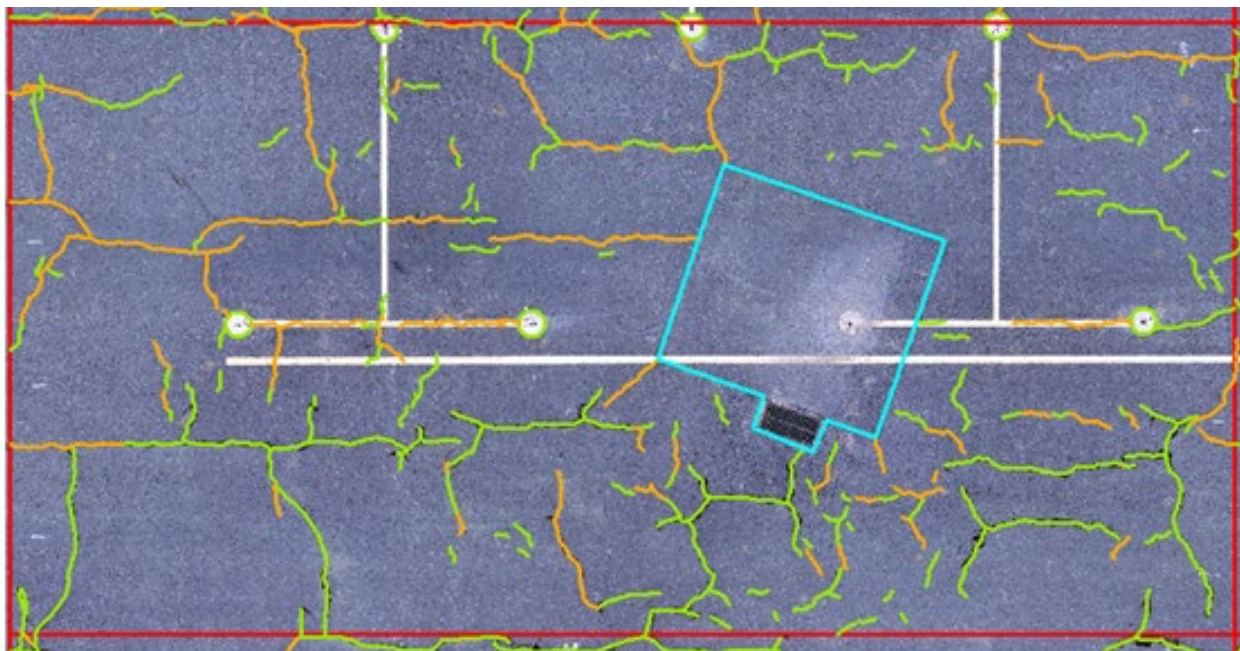
Figure 60. Example of sUAS Distress Analysis for GA Apron at WWD

5.5 STAGE 2—SAV

This section expands on the testing performed at SAV including test areas, control data, the use of ground control, sUAS data collection parameters, data processing workflows, and data analysis for PCI.

5.5.1 Test Areas

The test areas at SAV included the west end of Runway 10/28 and Taxiway GA4. Figures 61 and 62 illustrate the capture areas (yellow) and test areas (red) selected for data collection.

Figure 61. West End of Runway 10/28 at SAV
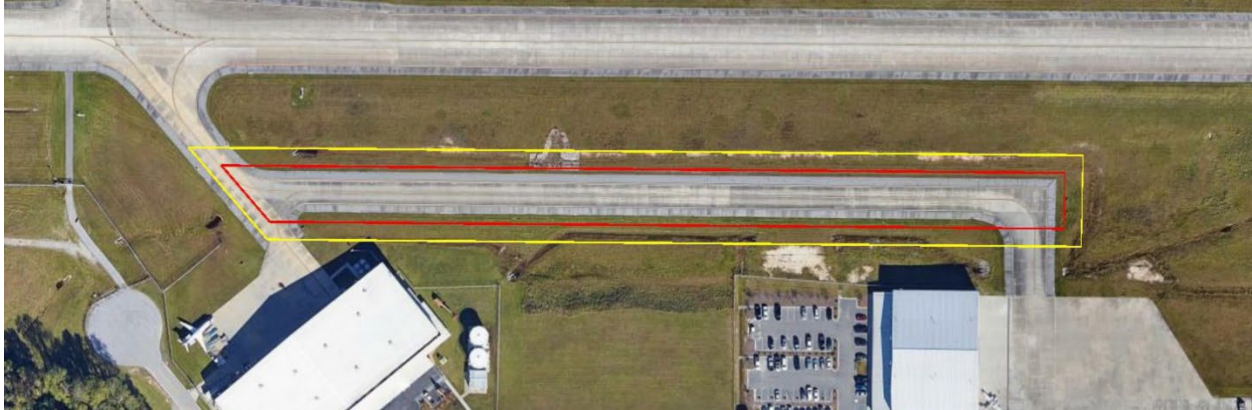
Figure 62. Taxiway GA4 at SAV

5.5.2 Control Data—FOG and DSV

Control data sets were collected through FOG and DSV surveys at SAV. Procedures followed were identical to those performed at WWD.

A summary of field notes that inspectors recorded to supplement the DSV data is as follows:

- Runway 10/28—100% Low-severity weathering
- Runway 10/28—100% Low-severity joint seal damage
- Taxiway GA4—Minimal low-severity blowups along the centerline

FOG and DSV PCI data were close in comparison on the Runway 10/28 sections with very similar distresses, severities, and quantities being recorded. However, due to the inability to accurately quantify or determine where the low-severity blowups were located on Taxiway GA4 (based on the field notes), and since these distresses were not observed in the intensity imagery from the DSV, these distresses were not captured in the DSV distress analysis. Consequently, the DSV PCI was 5 points higher than the FOG PCI for the PCC Taxiway GA4 section.

5.5.3 Ground Control

GCPs were RTK surveyed using a Trimble R8-3 GNSS receiver connected to a local base station at SAV. These data were assessed in the processing workflow to evaluate the requirement of having GCPs for a pavement distress analysis. Figures 63 and 64 show the numbers and locations of each point.
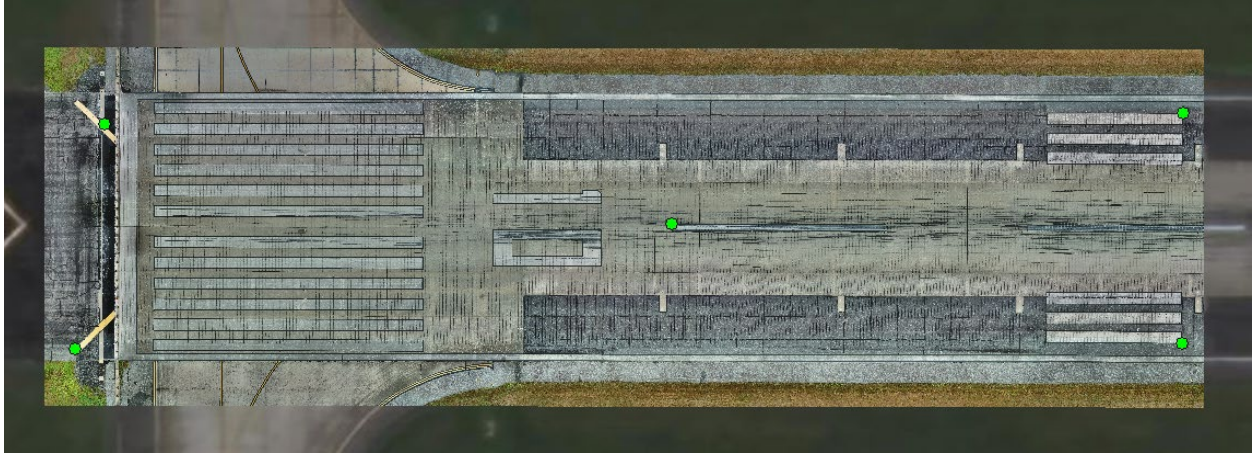
Figure 63. Five GCP Locations over Runway 10/28 at SAV

Figure 64. Five GCP Locations over Taxiway GA4 at SAV

5.5.4 Small Unmanned Aircraft System Data Collection Parameters

The data collection at SAV used an M210 at 2-mm GSD. These data were collected to validate the 2-mm orthoimagery at a high overlap of 75/60. Table 34 presents the data collection parameters.

Table 34. Data Collection Parameters for sUAS at SAV

Flight Number	Test Area	Airframe	Sensor	Data Type	Overlap (Forward/Side)	Altitude (ft)	GSD (mm)	Actual Flight Time (min)	Actual Number Photos
1	W End RWY 10/28	M210	X7-35mm	RGB	75/60	59.59	2	68	1,543
2*	~~TXY B & Apron~~	~~M210~~	~~X7-35mm~~	~~RGB~~	~~75 / 60~~	~~59.59~~	~~2~~	~~0~~	~~0~~
3	TWY GA4	M210	X7-35mm	RGB	75/60	59.59	2	52	1,213
					Total Flying Time	(Minutes)		120	

Note: Flight 2 was not collected due to airspace limitations.

74

Two flights were successfully executed as part of the data collection in Stage 2 at SAV. All completed flights collected RGB imagery. Due to connectivity issues, RTK on the sUA was not utilized for either flight at SAV.

5.5.5 Small Unmanned Aircraft System Data Processing

While ground control was surveyed, both data sets were processed with and without using those points. The processed data without GCPs indicated negligible geographical shift with no impact on identifying and analyzing the pavement distresses. Additionally, data processing without GCPs or RTK indicated negligible shift in relation to the established pavement sample units. It was determined that standalone GPS provided adequate absolute accuracy for pavement analysis. The benefit of this lies in reduced survey data collection time and was considered for further validation testing.

Table 35 presents the results of processed orthomosaics and their viability for distress analysis.

Table 35. Processing Results for sUAS Data at SAV

Flight Number	System	Overlap	GSD (mm)	Successful Orthomosaic	Acceptability for Analysis
1	M210	75/60	2	✓	✓
3	M210	75/60	2	✓	✓

5.5.6 Small Unmanned Aircraft System Data Analysis and Evaluation

West End of Runway 10/28

Runway 10/28 is 150 ft wide and a mix of AC and PCC pavement. The central sections are PCC, and the north and south sections are AC. The pavement is divided into north, central, and southern sections and further divided into sample units as shown in Figure 65. The size of the sections and sample units vary. While the capture limits included the western 1,250 ft of the runway, the test limits only encompassed north sections 01, 02, and 03, south sections 01, 02, and 03, and central sections 01, 02, 03, 04, 05, and 06.
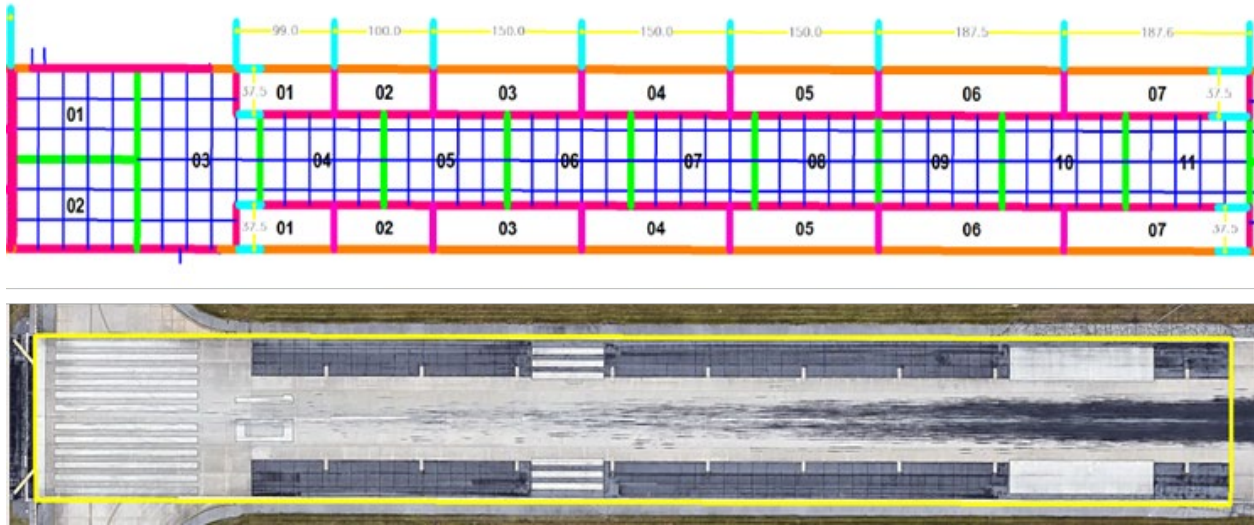
Figure 65. Sample Units of Runway 10/28 at SAV

Table 36 shows the PCI values of analyzed sample units.

Table 36. The PCI Values of Runway 10/28 at SAV

Section	Sample Number	FOG Sample PCI	DSV Sample PCI	sUAS Sample PCI	FOG Section PCI	DSV Section PCI	sUAS Section PCI
10C	01	84	87	80	84	84	78
	02	92	95	87			
	03	84	81	71			
	04	83	85	78			
	05	83	82	77			
	06	83	82	79			
10N	01	69	70	68	69	68	67
	02	69	69	67			
	03	69	67	66			
10S	01	68	74	65	73	72	69
	02	68	74	68			
	03	79	70	72			

The observed distresses and overall PCIs on Runway 10/28 were comparable between all data collection methods. In all three sections, the sUAS PCIs were slightly lower than those of the FOG and DSV.

In Section 10C of the PCC pavement, patching, shrinkage cracking, linear cracking, joint seal damage, joint spalling, and corner breaks were observed across FOG, DSV, and sUAS. The research team attributed the differences in PCI in this section to a 30% increase in shrinkage cracking and an increase in patching severity in the sUAS analysis.

Joint reflective cracking, weathering, and L&T cracking were observed on both of the asphalt overlay over Portland cement concrete (APC) pavement areas (Sections 10N and 10S). The differences in PCI in the AC sections were attributed to a 6% increase in overall cracking, with 2% more of the cracking recorded as medium severity in the sUAS analysis. It is worth noting that the joint seal damage and weathering previously added as supplemental data from field notes at WWD were analyzed during the sUAS distress takeoff. This analysis yielded the same results as the FOG inspection. Figure 66 illustrates an example of distress identified on Runway 10/28 at SAV.

Figure 66. Distress Example on Runway 10/28 at SAV

Overall, the differences between the sUAS and control data sets were minor and are attributed to being able to spend more time analyzing the pavement distresses in an office setting.

Taxiway GA4

Taxiway GA4, a mix of AC and PCC pavement, was broken into sample units, as illustrated in Figure 67.

Figure 67. Sample Units of Taxiway GA4 at SAV

Each of the seven sample units was analyzed, and their PCI values are shown in Table 37.

Table 37. The PCI Values of Taxiway GA4 at SAV

Section	Sample Number	FOG Sample PCI	DSV Sample PCI	sUAS Sample PCI	FOG Section PCI	DSV Section PCI	sUAS Section PCI
20	1	53	67	58	69	74	72
	2	70	77	76			
	3	70	74	71			
	4	73	76	76			
	5	73	76	76			
	6	78	77	78			
	7	68	68	66			

Identical distresses were observed on Taxiway GA4 as on Runway 10/28. The sUAS PCI was 3 points higher than that of the FOG PCI, with the difference directly attributed to three, low-severity blowups recorded in the FOG survey that were not observed in the sUAS data. Figure 68 displays sample unit 1, where two of the blowups were recorded in the FOG survey.
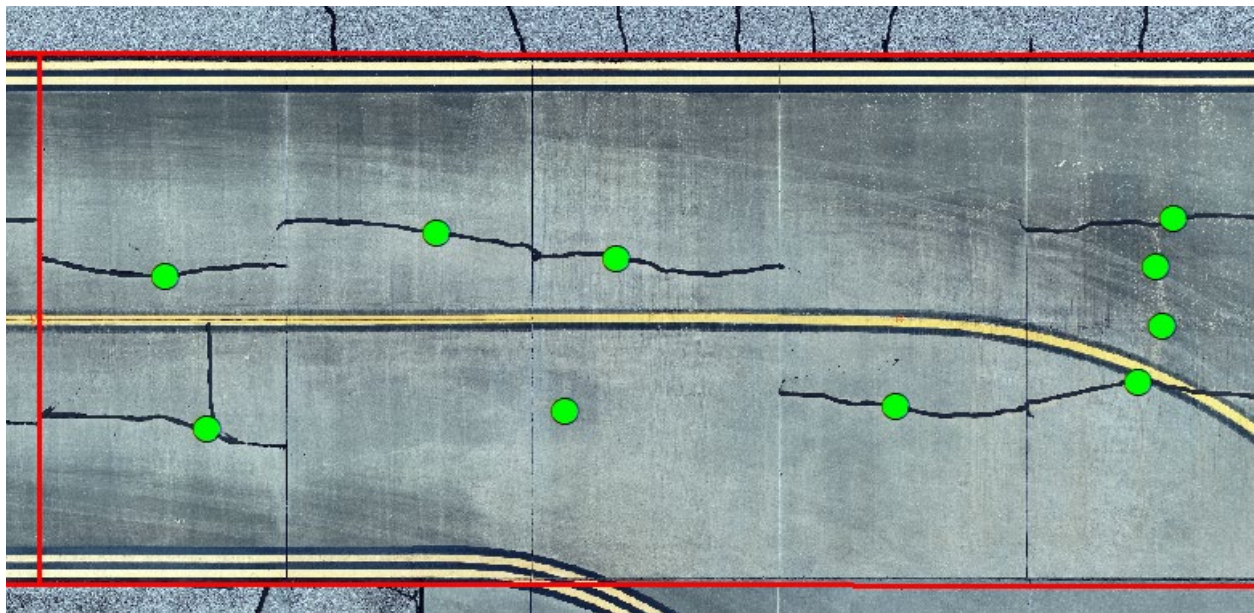
Figure 68. Sample Unit 1 of Taxiway GA4 at SAV

While the associated linear cracking was observed, there was no evidence of a blowup along the centerline as indicated in the field notes. Additional research is required to capture depth distresses, such as these blowups. Figure 69 illustrates an example of distress identified on Taxiway GA4 at SAV.
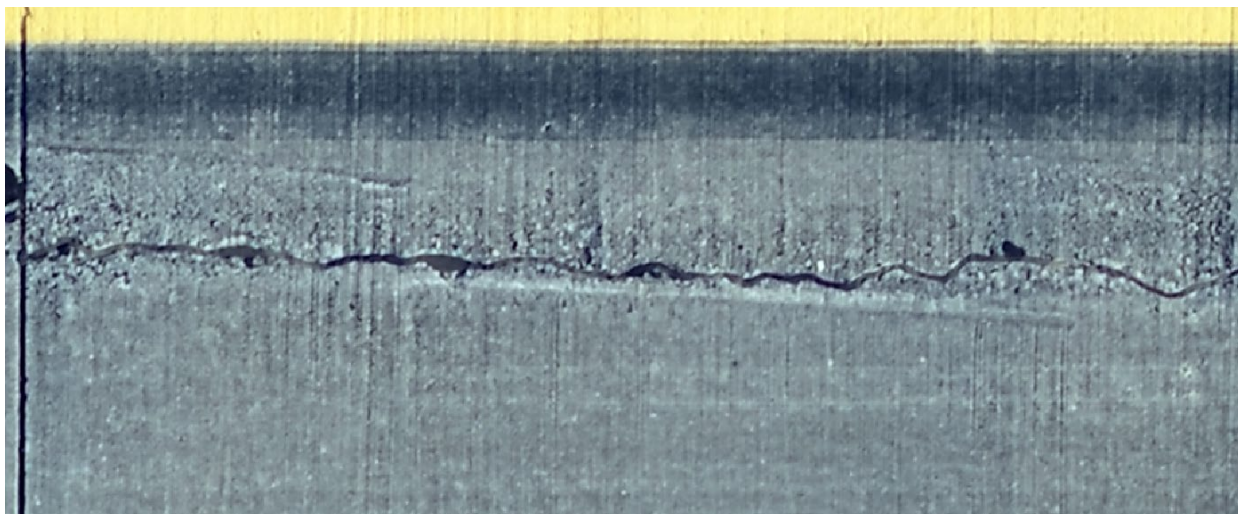
Figure 69. Distress Example on Taxiway GA4 at SAV

5.6 STAGE 3—CVG

This section expands on the testing performed at CVG including test areas, control data, the use of ground control, sUAS data collection parameters, data processing workflows, and data analysis for PCI.

5.6.1 Test Areas

The test area at CVG was the Remote Aircraft Parking Apron 1 South. Figure 70 illustrates the capture areas (yellow) and test areas (red) that were selected for data collection.
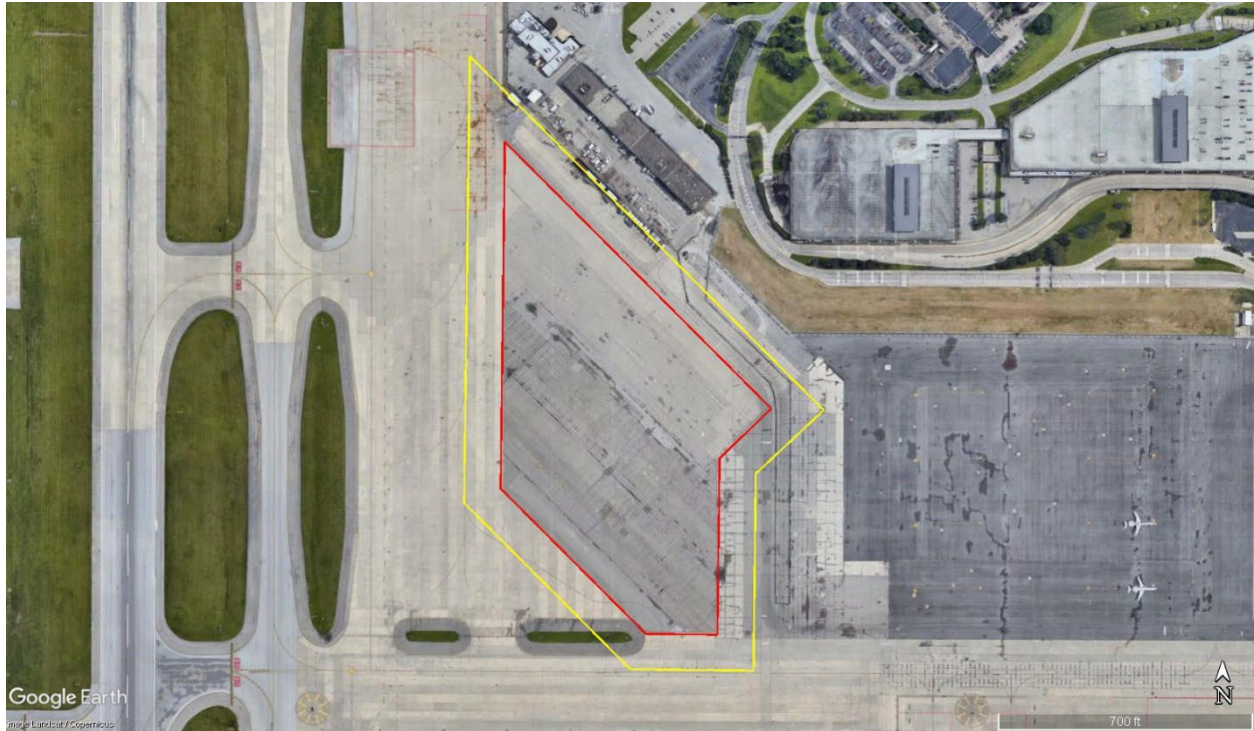
Figure 70. Remote Aircraft Parking Apron 1 South at CVG

5.6.2 Control Data—FOG and DSV

Control data sets were collected through FOG and DSV surveys, and identical procedures were followed to those performed at WWD and SAV. A summary of field notes recorded to use as supplemental data to the DSV data is as follows:

- Apron—Section 10 (PCC Pavement)—100% High-severity joint seal damage
- Apron—Section 20 (AC Pavement)—100% Medium-severity weathering
- Apron—Section 30 (AC Pavement)—100% Medium-severity weathering
- Apron—Section 40 (AC Pavement)—100% Low-severity weathering

As seen at WWD, the DSV PCI values for Sections 10, 20, and 30 were higher than the FOG PCI values. This was attributed to the poor resolution of the intensity and depth imagery, resulting in some of the DSV distresses being rated at a lesser severity than the FOG distresses. Section 40 of the apron experienced the same PCI value between the FOG and DSV surveys. Since this was a newer pavement with low-severity weathering and minimal other distresses, the weathering was the largest contribution to the PCI deductions and minimized the impact of the cracking distresses.

5.6.3 Ground Control

GCPs were RTK surveyed using a Trimble R8-3 GNSS receiver connected to a VRS. These data were not used in the production of the imagery that was analyzed and were only collected as a

backup for use in image processing if the resulting imagery was not spatially accurate. Figure 71 shows the number and locations of each point.

Figure 71. Five GCP Locations Over the Remote Aircraft Parking Apron 1 South at CVG

5.6.4 Small Unmanned Aircraft System Data Collection Parameters

The data collection at CVG used an M210 for RGB imagery and a Rock R2A sensor for LiDAR. For the RGB imagery, the research team aimed to further validate the data acquired at lower overlap settings and to introduce 3-mm GSD. Table 38 presents the data collection parameters.

Table 38. Data Collection Parameters for sUAS at the Remote Aircraft Parking Apron 1 South at CVG

Flight Number	Airframe	Sensor	Data Type	Overlap (Forward/ Side)	Altitude (ft)	GSD (mm)	Actual Flight Time (min)	Actual Number Photos
1	M210	X7-35mm	RGB	30/30	58.65	2	97	1,975
2	M210	X7-35mm		30/30	87.97	3	44	880
3	M210	X7-35mm		20/20	58.65	2	64	1,517
4	M210	X7-35mm		20/20	87.97	3	31	666
5	M210	Rock R2A	Lidar	5/33	39	N/A	N/A	N/A
6	M210	Rock R2A		5/33	60	N/A	N/A	N/A
7	M210	Rock R2A		5/33	145	N/A	N/A	N/A
8	M210	X7-35mm	RGB	40/40	87.97	3	47	1,199

A total of eight flights were successfully executed as part of data collection, three of which were flown to collect LiDAR, and the remaining five to collect RGB imagery. The LiDAR flight parameters were developed to derive a certain point density, with an ortho being a secondary derivative if possible. However, due to time constraints, lower overlap was collected, which did not yield imagery that could be processed into an ortho.

No operational issues were encountered during data collection at CVG. However, Flight 4 was repeated at a later time due to poor image quality during the first attempt. As a result, the research team optimized the field Quality Assurance/Quality Control (QA/QC) procedures. The initial processing for data collected with 30/30 overlap indicated loss of data in the orthomosaic. For these reasons, an overlap of 40/40 was added and collected along with the repeated Fight 4.

5.6.5 Light Detection and Ranging Data

LiDAR was introduced to identify texture and vertical distresses at CVG. The LiDAR data collection had no issues. LiDAR processing involves multiple steps to achieve accurate elevation information:

Airborne GPS Processing. In this process, kinematic corrections for the aircraft position are resolved using aircraft GPS and static ground GPS (1-Hz) for each geodetic control (base station) within the test limits.

Inertial Measurement Unit (IMU) Processing. Post processing of the IMU system data is completed to compute an optimally accurate blended navigation solution based on Kalman filtering technology, or the Smooth Best Estimate of Trajectory (SBET).

LiDAR Point Processing and Quality Control. Once the data acquisition, GPS, and IMU processing are complete, a formal data reduction process occurs that includes:

- Calculating laser point position by associating SBET position to each laser point return time, scan angle, intensity, etc. The raw laser point cloud data are created for the entire survey; each point will maintain the corresponding scan angle; return number (echo); intensity; and x, y, z information.
- Ground and nonground points are classified and statistical absolute accuracy is assessed via direct comparisons of ground classified points to the ground control (RTK survey data).
- Data are then converted to orthometric elevations and the appropriate map projection.
- Relative accuracy is tested using ground classified points per each flight line.
- Additional ground models can then be created, such as the DEM shown in Figure 72.
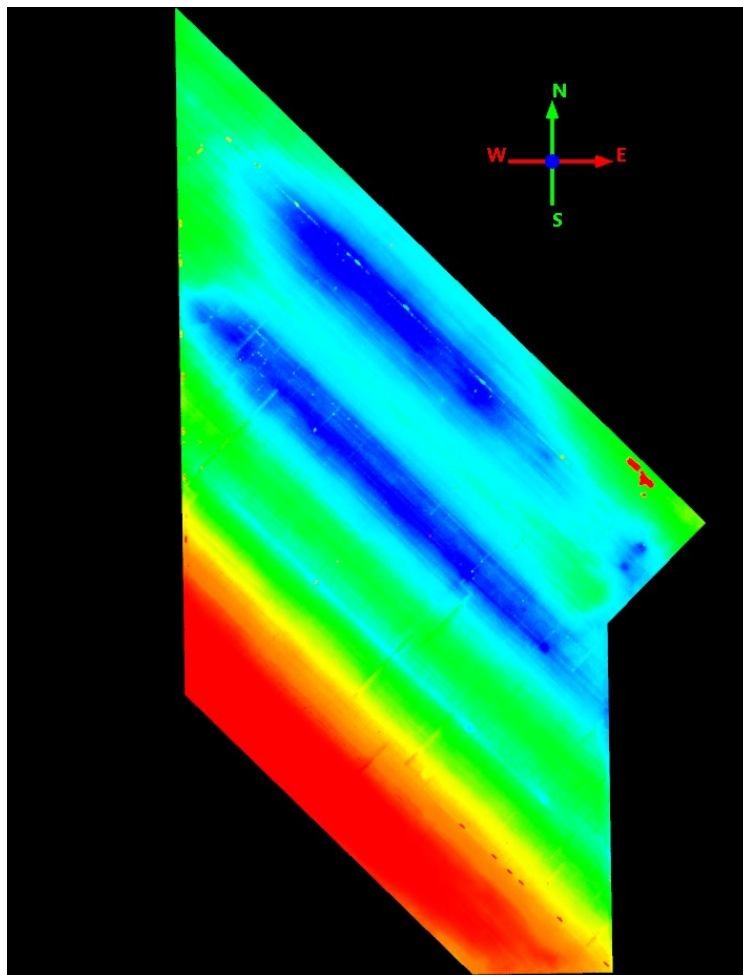
Figure 72. A DEM Derived from LiDAR Point Cloud at CVG

Figure 73 illustrates a sample cross section through both an RGB and a LiDAR data set. The results from this specific flight (Flight 5) indicated that LiDAR lacked the point density (resolution) to accurately determine crack depth.

Cross Section through RGB Orthomosaic

Cross Section through LiDAR
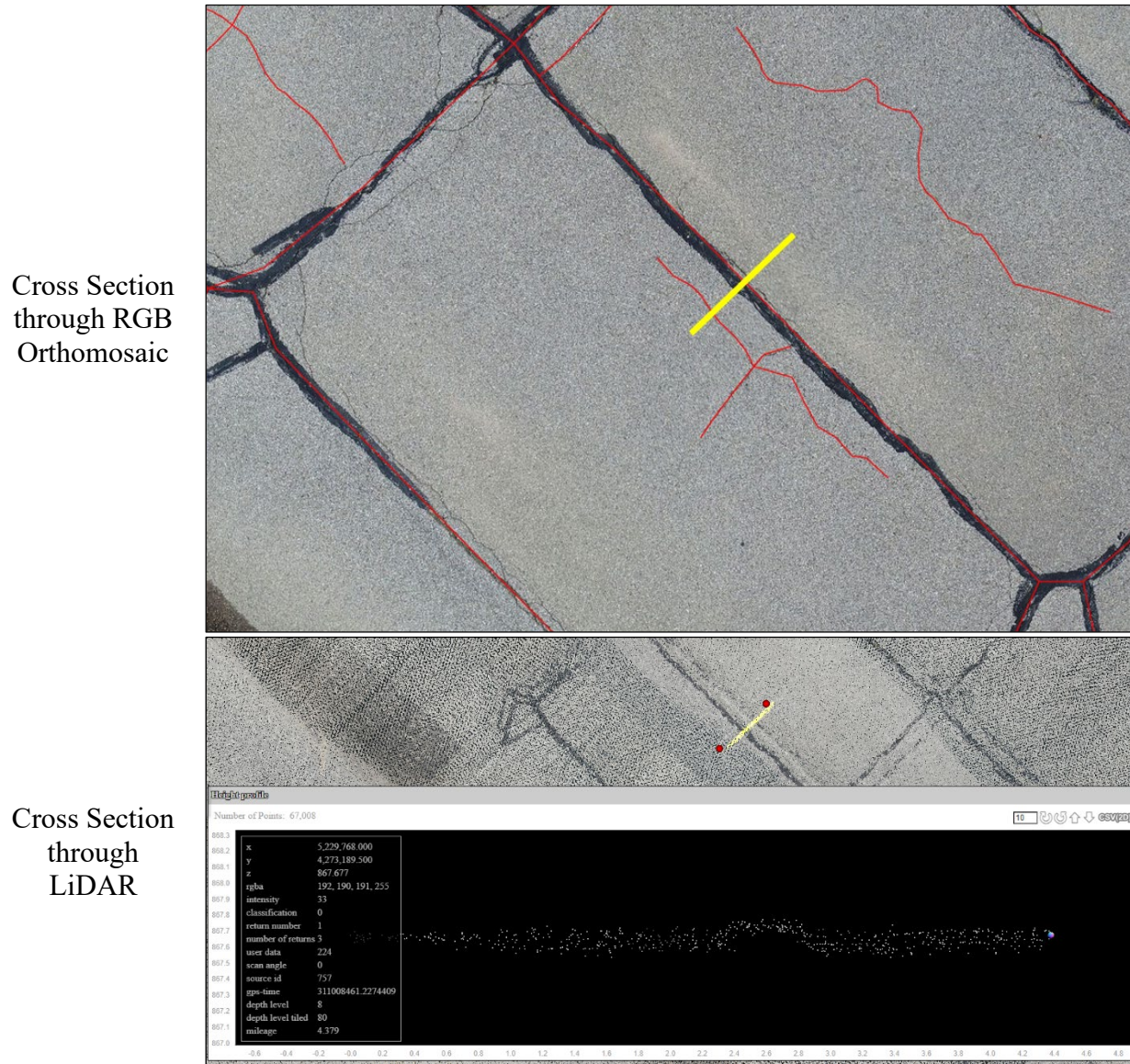
Figure 73. Cross Section Through a Crack of LiDAR Data

5.6.6 Small Unmanned Aircraft System Data Processing

The research team introduced a combination of variables and sensors in Stage 3 of testing. The RGB sensors tested new overlap and GSD values, while the LiDAR sensor was tested at different altitudes and flying speeds. As a result, the research team found holes and gaps in some of the processed data. Flight 4 processing generated an orthomosaic, but stitching issues during the automatic tiling process resulted in the orthomosaic being too incomplete for analysis. Alternatively, while it was still possible to generate a full orthomosaic through manual stitching

of the images, a significant amount of time is needed to accomplish the desired results. Due to these reasons, Flight 8 was introduced in the test plan to collect data at 40/40 overlap and 3-mm GSD. This parameter led to generating a complete orthomosaic acceptable for analysis.

Table 39 presents a summary of all processed flights for RGB data. Figures 74 through 77 illustrate the orthomosaic results of Flights 1, 2, 4, and 8. Processing for Flight 3 completely failed due to a combination of large GSD (small image footprint) and low overlap.

Table 39. Processing Results for sUAS RGB Data at CVG

Flight Number	System	Overlap	GSD (mm)	Successful Orthomosaic	Acceptable for Analysis
1	M210	30/30	2	✓	✓
2	M210	30/30	3	✗	✓
3	M210	20/20	2	✗	✗
4	M210	20/20	3	✓	✗
8	M210	40/40	3	✓	✓

Flight 1
DJI M210 RTK v2 | X7-35mm | 30/30 Overlap | 2-mm GSD
Successful Orthomosaic: No; minor gaps were present.
Acceptable for Analysis: Yes; gaps were in areas not being analyzed.
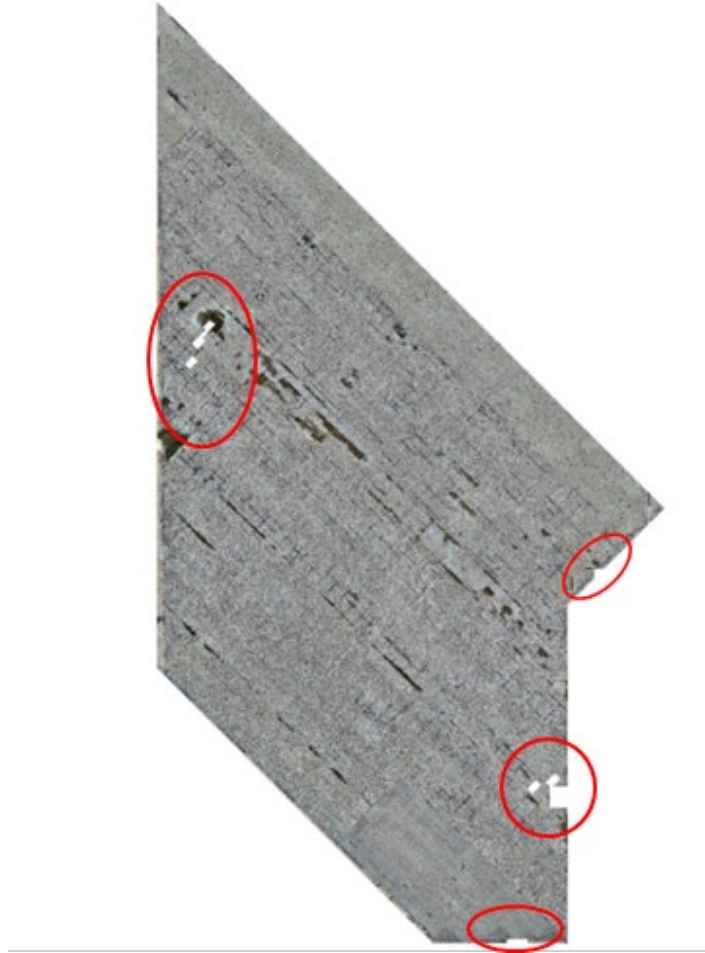
Figure 74. Flight 1 at CVG

Flight 2
<u>DJI M210 RTK v2 | X7-35mm | 30/30 Overlap | 3-mm GSD</u>
Successful Orthomosaic: Yes; no gaps in the orthomosaic due to larger image footprint.
Acceptable for Analysis: Yes.

Figure 75. Flight 2 at CVG

Flight 3
DJI M210 RTK v2 | X7-35mm | 20/20 Overlap | 2-mm GSD
Successful Orthomosaic: Processing completely failed due to a combination of small GSD (leading to a small image footprint) and low overlap.
Acceptable for Analysis: No.

Flight 4
DJI M210 RTK v2 | X7-35mm | 20/20 Overlap | 3-mm GSD
Successful Orthomosaic: Yes; however, there are many gaps within the orthomosaic.
Acceptable for Analysis: No.

Figure 76. Flight 4 at CVG

Flight 8
DJI M210 RTK v2 | X7-35mm | 40/40 Overlap | 3-mm GSD
Successful Orthomosaic: Yes.
Acceptable for Analysis: Yes.

Figure 77. Flight 8 at CVG

Table 40 presents a summary of all processed flights for LiDAR data. Flights 5, 6, and 7 did not have enough side overlap to generate an orthomosaic from the RGB images. However, Figures 78 through 80 illustrate the LiDAR point densities for these flights. Further research is required to assess the viability of LiDAR data in PMP inspections. Section 7 details these research gaps and recommendations.

Table 40. Processing Results for sUAS LiDAR Data at CVG

Flight Number	System	Side Overlap	Minimum Density (points/m^2)	Successful Orthomosaic	Acceptability for Analysis
5	M210 | Rock R2A	33	3,355	✗	Further research required
6	M210 | Rock R2A	33	1,633	✗	
7	M210 | Rock R2A	33	676	✗	

Flight 5
DJI M210 RTK v2 | Rock R2A | 33% Side Overlap | 3,355 Minimum points/m^2 Density
Successful Orthomosaic: Not applicable.
Acceptable for Analysis: Further research required.
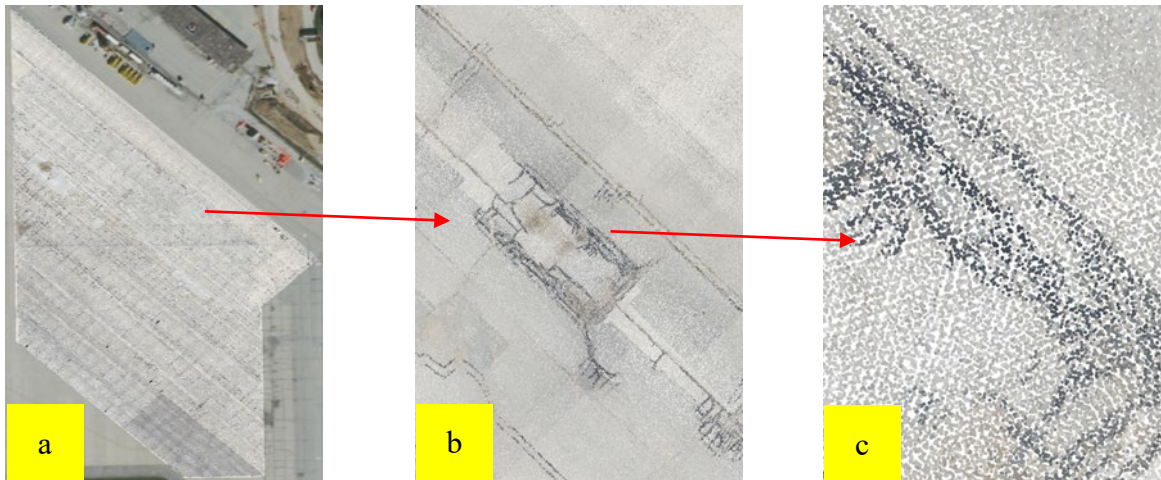
Figure 78. Flight 5 at CVG

Flight 6
DJI M210 RTK v2 | Rock R2A | 33% Side Overlap | 1,633 Minimum points/m^2 Density
Successful Orthomosaic: Not applicable.
Acceptable for Analysis: Further research required.
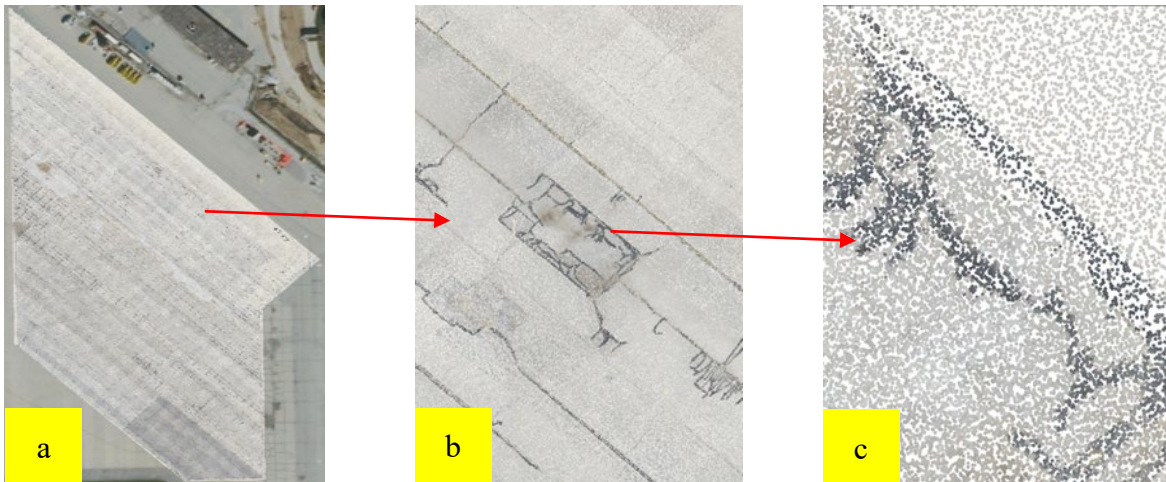
Figure 79. Flight 6 at CVG

Flight 7
DJI M210 RTK v2 | Rock R2A | 33% Side Overlap | 676 Minimum points/m^2 Density
Successful Orthomosaic: Not applicable.
Acceptable for Analysis: Further research required.

Figure 80. Flight 7 at CVG

5.6.7 Small Unmanned Aircraft System Data Analysis and Evaluation

Remote Aircraft Parking Apron 1 South
The Remote Aircraft Parking Apron 1 South is approximately 580,000 sq ft and a mix of APC and PCC pavements. The pavement is divided into four sections and further divided into sample units as shown in Figure 81. Section 10 is PCC pavement with 20 samples. Sections 20, 30, and 40 are APC pavement. The size of the sections and sample units vary. While the capture limits included the entire Remote Aircraft Parking Apron 1 South, the test limits encompassed sections 10 and 40, and only portions of sections 20 and 30.

Figure 81. Remote Aircraft Parking Apron 1 South Sample Units at CVG

Tables 41 through 44 show the PCI values of analyzed samples.

Table 41. The PCI Values of Section 10 at CVG

Section	Sample Number	FOG PCI	DSV PCI	sUAS PCI (Flight 1)	sUAS PCI (Flight 2)	FOG Section PCI	DSV Section PCI	sUAS Section PCI (Flight 1)	sUAS Section PCI (Flight 2)
	001	52	54	52	55				
	002	64	65	69	69				
	003	60	65	72	72				
	004	63	67	73	73				
	005	83	88	91	91				
	006	87	87	89	89				
	007	88	83	85	85				
	008	88	88	86	86	78	80	82	83
10	009	86	84	88	88				
	010	82	88	85	91				
	011	85	87	85	85				
	012	87	88	88	88				
	013	83	87	84	84				
	014	83	88	88	88				
	015	83	81	86	88				
	016	77	83	86	86				

92

Section	Sample Number	FOG PCI	DSV PCI	sUAS PCI (Flight 1)	sUAS PCI (Flight 2)	FOG Section PCI	DSV Section PCI	sUAS Section PCI (Flight 1)	sUAS Section PCI (Flight 2)
10	017	83	88	85	85	78	80	82	83
	018	82	84	85	86				
	019	79	80	80	80				
	020	56	60	68	70				

Table 42. The PCI Values of Section 20 at CVG

Section	Sample Number	FOG PCI	DSV PCI	sUAS PCI (Flight 1)	sUAS PCI (Flight 2)	FOG Section PCI	DSV Section PCI	sUAS Section PCI (Flight 1)	sUAS Section PCI (Flight 2)
20	025	37	43	43	43	47	56	46	48
	026	41	45	44	43				
	027	44	60	41	41				
	028	48	58	46	46				
	029	47	61	16	51				
	030	49	59	48	43				
	031	56	63	56	55				
	032	48	63	64	62				
	041	44	51	48	48				
	042	53	55	53	54				
	043	43	56	46	42				
	044	47	58	51	50				

Table 43. The PCI Values of Section 30 at CVG

Section	Sample Number	FOG PCI	DSV PCI	sUAS PCI (Flight 1)	sUAS PCI (Flight 2)	FOG Section PCI	DSV Section PCI	sUAS Section PCI (Flight 1)	sUAS Section PCI (Flight 2)
30	076	30	32	37	38	28	31	27	27
	077	31	33	37	37				
	078	30	25	36	36				
	080	31	32	39	40				
	081	35	35	27	28				
	082	23	34	40	40				
	083	33	30	22	22				
	084	20	34	23	23				
	085	22	26	2	3				
	086	29	32	18	19				
	087	23	28	18	19				
	088	28	32	22	18				

Table 44. The PCI Values of Section 40 at CVG

Section	Sample Number	FOG PCI	DSV PCI	sUAS PCI (Flight 1)	sUAS PCI (Flight 2)	FOG Section PCI	DSV Section PCI	sUAS Section PCI (Flight 1)	sUAS Section PCI (Flight 2)
40	112	90	87	90	89	88	88	87	86
	113	89	86	86	85				
	114	89	87	87	86				
	115	87	88	88	86				
	116	84	88	83	82				
	117	86	90	89	87				

The four test sections at CVG were diverse in terms of deterioration. While the airport was not actively using any of these sections at the time of this research, Section 10 and Section 20 were better maintained and represented typical airfield pavements. Regardless, all four sections experienced very similar PCI results between each data collection method.

The global distresses were not supplemented into the data set from field notes, but, rather, were analyzed from the imagery. There was an instance where the sUAS data did not match the FOG data in Section 10. The severity of joint-seal damage was split between medium and high severity, instead of 100% high severity recorded in the FOG data. However, field notes indicate oxidation or hardening of the joint seal, which is only able to be observed by physically touching the joint seal.

Section 10 also included a new distress that had not been observed at WWD or SAV: durability cracking. Only two out of the 1,000+ inspected slabs displayed signs of durability cracking. Both were identified in the sUAS analysis, while only one was recorded in the FOG collection.

5.7 STAGE 4—ONZ AND TTF

This section expands on the testing performed at ONZ and TTF including test areas, control data, the use of ground control, sUAS data collection parameters, data processing workflows, and data analysis for PCI.

5.7.1 Test Areas

The test areas at ONZ included Runway 17/35, Taxiway A, and connector taxiways. Figures 82 and 83 illustrate the data capture areas (yellow) and test areas (red) that were selected for data collection.

Figure 82. Runway 17/35 at ONZ

Figure 83. Taxiway A at ONZ

The test areas at TTF included Runway 03/21 and Taxiway A. During data collection, the data for the connector Taxiways A2 and A3 were also collected. Hence, Taxiways A2 and A3 were included in the analysis and evaluation of the PCIs. Figure 84 illustrates the capture areas (yellow) and test areas (red) selected for data collection.

Figure 84. Runway 03/21 and Taxiway A at TTF

5.7.2 Control Data—FOG and DSV

Control data sets were collected through FOG survey and consisted of a 100% survey of all test areas. A total of 188 PCC samples were inspected at ONZ, and 47 AC samples were inspected at TTF. It was determined that sUAS-derived orthoimagery was of better quality than the DSV data. The sUAS had the ability to

- Identify a wider range of distresses.
- Collect higher resolution imagery.
- Analyze lower-severity distresses.
- Collect data with significantly cheaper equipment.
- Produce PCI values comparable to FOG inspections.

Hence, it was determined that DSV data collection was not required for comparison against the FOG or sUAS data sets.

5.7.3 Ground Control

GCPs were surveyed using a Trimble R8-3 through RTK GNSS surveying. GCPs were not used in the production of the analyzed imagery and were only collected as a backup for use in image

processing if the resulting imagery was not spatially accurate. Figures 85 and 86 show the numbers and locations of each point.
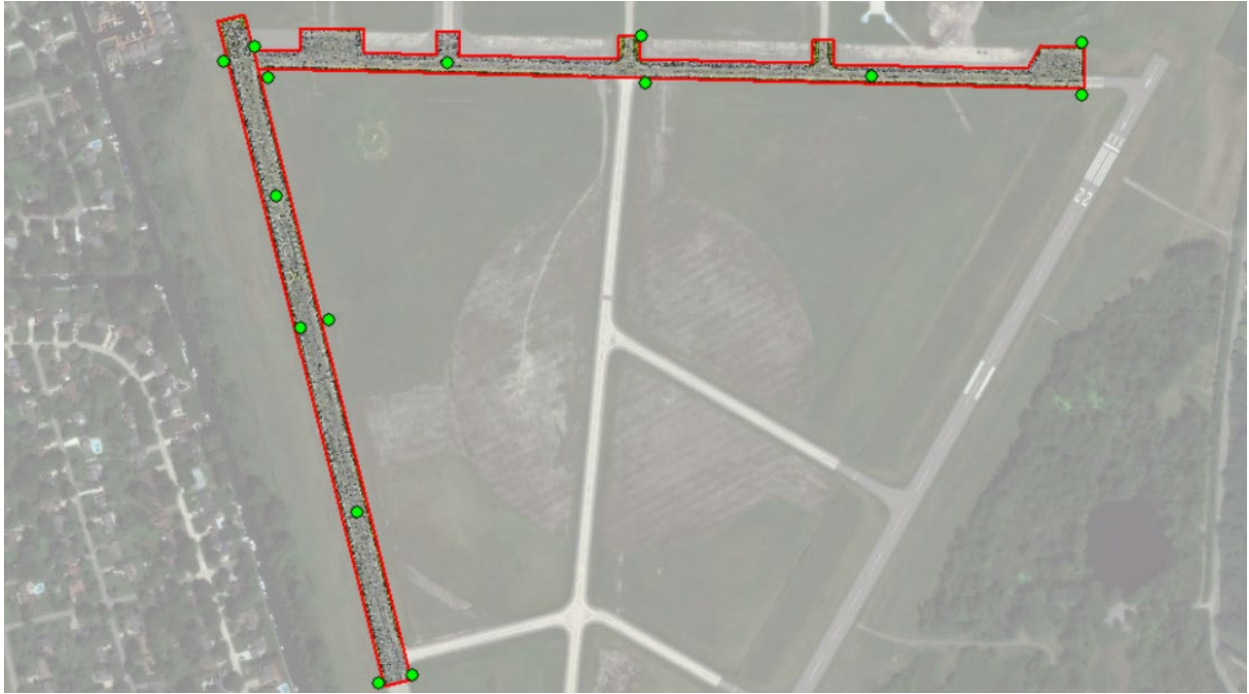
Figure 85. Ground Control Points Locations Over Each Test Area at ONZ

Figure 86. Ground Control Points Locations Over Each Test Area at TTF

5.7.4 Small Unmanned Aircraft Systems Data Collection Parameters

The data at ONZ were collected to evaluate the efficiency of collecting 2-mm GSD with a previously untested overlap. Table 45 presents the data collection parameters.

Table 45. Data Collection Parameters for sUAS at ONZ

Flight Number	Test Area	Airframe	Sensor	Data Type	Overlap (Forward/ Side)	Altitude (ft)	GSD (mm)	Actual Flight Time (min)	Actual Number Photos
2	Runway 17/35	M210	X7-35mm	RGB	50/50	58.65	2	128	2,234
4	TWY A	M210	X7-35mm	RGB	50/50	58.65	2	137	2,640

The data at TTF were collected to evaluate the efficiency of collecting 2-mm GSD with a previously untested overlap. Table 46 presents the data collection parameters.

Table 46. Data Collection Parameters for sUAS at TTF

Flight Number	Test Area	Airframe	Sensor	Data Type	Overlap (Forward/ Side)	Altitude (ft)	GSD (mm)	Actual Flight Time (min)	Actual Number Photos
6	Runway 03/21	M210	X7-35mm	RGB	50/50	58.65	2	89	1,622
8	TWY A, A2, A3	M210	X7-35mm	RGB	50/50	58.65	2	102	1,461

Four flights were successfully executed as part of the data collection in Stage 2.4 at ONZ and TTF. All flights collected RGB imagery. The data collection team had to pause flight operations numerous times during data collection efforts due to manned aircraft activity at both airports.

5.7.5 Small Unmanned Aircraft System Data Processing

The research team encountered issues during the orthoimagery processing for Flight 8 at TTF due to inconsistent results obtained from the Pix4D Mapper software.

Following initial preparation, the processing team used an aerial triangulation (AT) software package to process the imagery and photo control data. Due to inaccuracies in the sUAS reported payload orientation for Flight 8, the use of ground control targets was needed to correct for the sUAS imagery's erroneous initial exterior orientation. Without these targets, the AT software was unable to produce a viable solution or complete orthorectification successfully. Had the sUAS payload accurately reported the camera orientation, the team believes that GCPs would not have been needed to generate an orthomosaic, as evidenced by the successful processing of Flight 6, which did not require ground control.

The processed data for Flights 2, 4, and 6 without ground control indicated negligible geographical shift with no impact on identifying and analyzing the pavement distresses. Table 47 presents the results of processed orthomosaics and their viability for distress analysis.

Table 47. Processing Results for sUAS RGB Data at ONZ & TTF

Flight #	System	Site	Overlap	GSD (mm)	Successful Orthomosaic	Acceptability for Analysis
2	M210	ONZ RWY 17/35	50/50	2	✓	✓
4	M210	ONZ TWY A	50/50	2	✓	✓
6	M210	TTF RWY 03/21	50/50	2	✓	✓
8	M210	TTF TWY A	50/50	2	✓	✓

5.7.6 Small Unmanned Aircraft System Data Analysis and Evaluation

Six total test areas, which covered a large portion of each airfield, were selected at ONZ and TTF. These airfields were selected so that new pavement distresses that were not observed at previous airports could be identified, namely, alkali-silica reactions (ASR) of the PCC pavements at ONZ.

ONZ test areas consisted of one PCC runway and one PCC taxiway. Eighteen samples from Runway 17/35 and 20 samples from Taxiway A were evaluated as part of ONZ distress analysis. Both test sections consisted of very aged pavement with a considerable amount of ASR reported by the airport. ASR is a rare pavement distress; however, it carries a high level of importance when observed on an airfield due to the extreme FOD potential that it creates.

Note: Random samples were selected for all four test areas at ONZ and TTF to evaluate and perform a distress and PCI analysis.

Runway 17/35

Runway 17/35 is 75 ft wide and entirely PCC pavement. The pavement is composed of a single section and divided into sample units, as shown in Figure 87. Each sample unit is 30 ft x 75 ft (2,250 sq ft). While the capture limits included the northern 2,500 ft of the runway, the test limits only encompassed 18 sample units chosen to represent the varied conditions across the section.
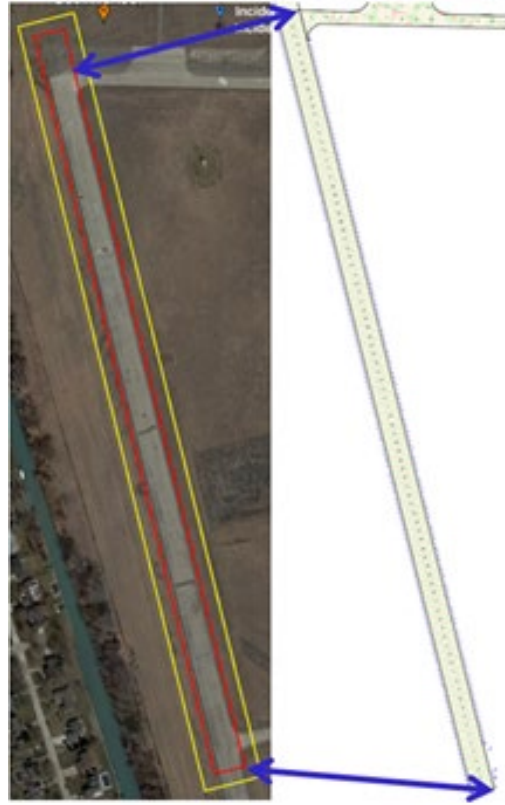
Figure 87. Sample Units of Runway 17/35 at ONZ

Table 48 shows the PCI values of analyzed sample units.

Table 48. The PCI Values of Runway 17/35 at ONZ

Section	Sample Number	FOG PCI	sUAS PCI	FOG Section PCI	sUAS Section PCI
RWY 17/35	2	13	36	28	19
	5	13	13		
	10	13	13		
	15	36	13		
	20	18	11		
	25	45	40		
	30	45	18		
	35	13	8		
	40	13	13		
	46	13	13		
	50	13	13		
	55	36	13		
	61	26	13		
	66	11	12		
	71	45	26		

Section	Sample Number	FOG PCI	sUAS PCI	FOG Section PCI	sUAS Section PCI
RWY 17/35	76	51	48	28	19
	82	46	9		
	87	46	27		

Taxiway A

Taxiway A is 40 ft wide and entirely PCC pavement. The pavement is composed of a single section and divided into sample units as shown in Figure 88. Each sample unit on Taxiway A is 40 ft x 50 ft (2,000 sq ft), while the samples on the connector taxiways vary in size. Although the capture limits included the entirety of Taxiway A and portions of associated connectors, the test limits only encompassed 23 sample units chosen to represent the varied conditions across the section.
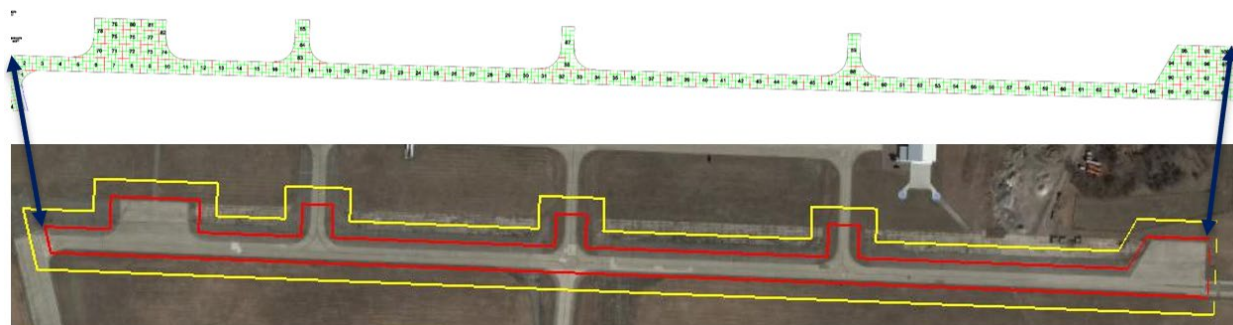
Figure 88. Sample Units of Taxiway A at ONZ

Table 49 shows the PCI values of analyzed sample units.

Table 49. The PCI Values of Taxiway A at ONZ

Section	Sample Number	FOG PCI	sUAS PCI	FOG Section PCI	sUAS Section PCI
TWY A	4	45	17	46	38
	9	56	35		
	14	58	51		
	19	53	39		
	23	63	49		
	28	54	43		
	33	0	52		
	38	67	59		
	43	42	16		
	47	24	19		
	52	45	28		
	57	36	18		

Section	Sample Number	FOG PCI	sUAS PCI	FOG Section PCI	sUAS Section PCI
TWY A	62	59	56	46	38
	66	48	45		
	71	72	58		
	76	50	39		
	81	68	53		
	*85	50	42		
	*87	25	19		
	*88	18	35		
	91	51	40		
	96	45	37		
	99	36	22		

*Samples 85, 87, and 88 are part of connecter taxiways that were considered for the PCI evaluation of Taxiway A.

FOG and sUAS trends between each sample unit and section PCI value were largely aligned with one another, however, there were some obvious dissimilarities. sUAS values were typically lower than that of the FOG inspection due to the surveyor's interpretation of the ASTM guidance on determining ASR severity levels.

ASR was observed in every sample on the airfield. The deduct values were not only impactful to the PCI score, but they also had a drastic difference in deduction per severity level. In a typical 20-slab PCC sample, with one slab exhibiting low-severity ASR, one slab presenting medium-severity ASR, and one slab showing high-severity ASR, deduct values for each distress would be -5.04, -14.03, and -23.13, respectfully. For comparison, the same sample with equal amounts of corner breaks would have deduct values of -4.07, -8.41, and -13.15, respectively. Therefore, when a surveyor evaluates whether there is—as defined in the ASTM—"Minimal," "Some," or "High," amount of FOD potential caused by the ASR, the resulting PCI can change drastically. Nevertheless, when comparing the total number of slabs that contained ASR from the FOG and sUAS inspections, the total was nearly identical, confirming that sUAS data collection can effectively observe this distress.

Ten samples from Runway 03/21, eight samples from Taxiway A, two samples from Taxiway A2, and two samples from Taxiway A3 were evaluated as a part of the TTF distress analysis. These test sections consisted of moderately aged pavements with pavement distresses typical to most airfields.

Runway 03/21 and Taxiways A, A2, and A3

Runway 03/21 and Taxiways A, A2, and A3 are 100 ft wide and are entirely AC pavement. The runway is composed of a single section, as are each taxiway. The sections are further divided into sample units as shown in Figure 89. Each runway sample unit size is 50 ft x 100 ft (5,000 sq ft) while the taxiway sample units vary in size. Although the capture limits included 1,700 ft of the runway and 2,000 ft of taxiway, the test limits only encompassed 22 sample units chosen to represent the varied conditions across the sections.
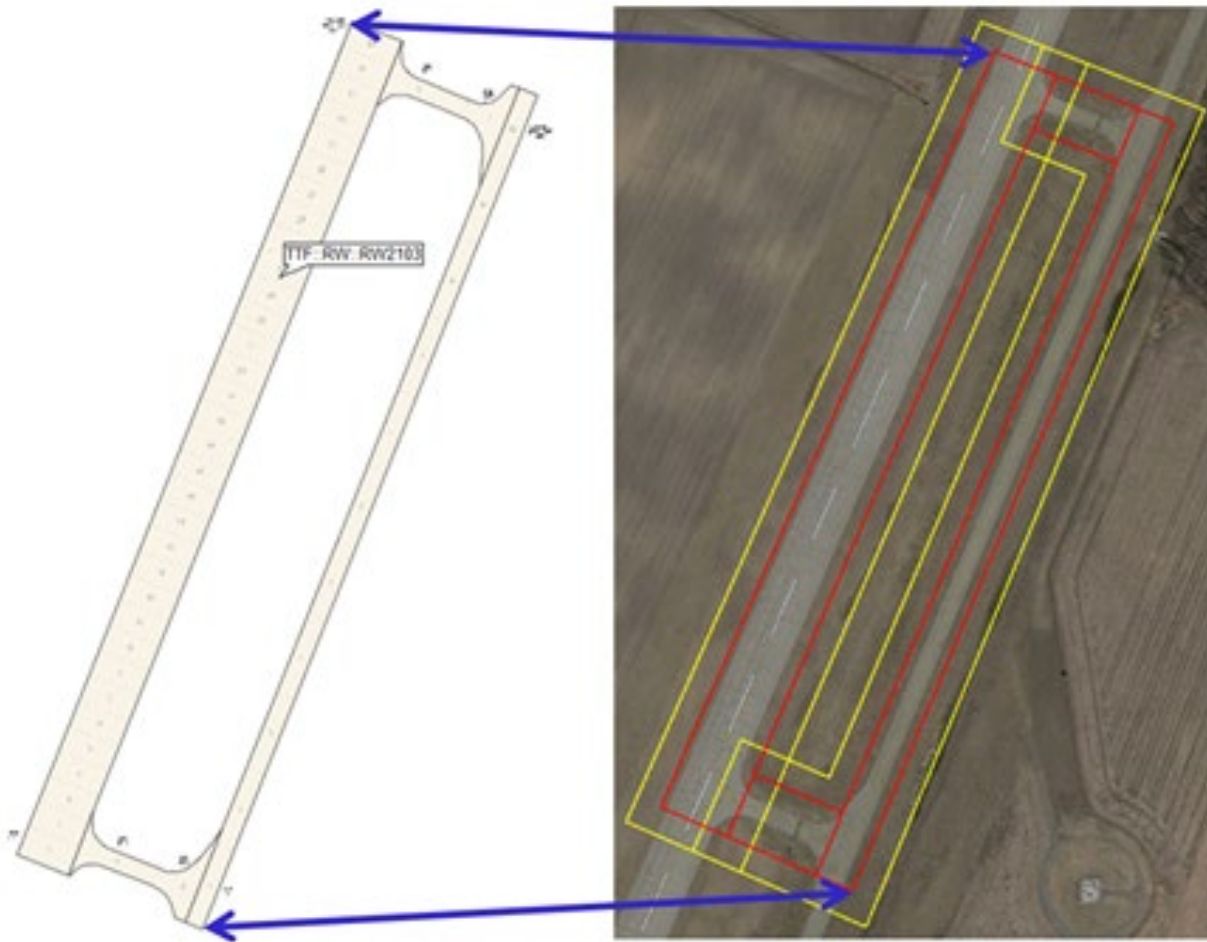
Figure 89. Sample Units of Runway 03/21 and Taxiways A, A2, and A3 at TTF

Tables 50 and 51 show the PCI values of analyzed sample units.

Table 50. The PCI Values of Runway 03/21 at TTF

Section ID	Sample Number	FOG PCI	sUAS PCI	FOG Section PCI	sUAS Section PCI
RWY 03/21	2	81	75	77	77
	4	74	77		
	6	76	76		
	10	76	77		
	14	77	76		
	16	82	81		
	18	72	73		
	22	80	82		
	26	72	73		
	30	79	80		

Table 51. The PCI Values of Taxiway A, A2, and A3 at TTF

Section ID	Sample Number	FOG PCI	sUAS PCI	FOG Section PCI	sUAS Section PCI
TWY A	2	70	70	70	70
	3	70	70		
	4	70	70		
	6	70	70		
	7	69	70		
	8	70	71		
	9	70	70		
	10	69	70		
TWY A2	1	59	65	64	67
	2	70	69		
TWY A3	1	64	63	67	64
	2	70	66		

As observed at WWD, SAV, and CVG, sUAS data collection performs very closely to FOG surveys when evaluating airfield pavement, such as on the TTF pavement sections. Distresses were largely limited to weathering and L&T Cracking, and the PCI values between the FOG and sUAS evaluations were nearly identical.

5.8 PHASE 2 SUMMARY

The testing and research performed during Phase 2 across WWD, SAV, CVG, ONZ, and TTF led to the following conclusions:

- 2-mm GSD (or smaller) orthomosaic imagery derived from sUAS data collection is preferred for PCI analysis.
- 3-mm GSD orthomosaic imagery derived from sUAS data collection is acceptable but requires minimal assumptions to identify global distresses. Some minor severity L&T cracking can also be missed at this resolution.
- 4-mm GSD (or larger) is not acceptable for pavement inspection, as it does not consistently identify low-severity distresses. Additionally, global distresses can appear blurry and are harder to identify with lower resolution imagery.
- The parameters tested with LiDAR data did not provide enough detail for analysis.
- The processed imagery without surveyed ground control indicated negligible geographical shift with no impact on identifying and analyzing the pavement distresses.
- The PCI values did not indicate a significant difference when RTK was not utilized for either test area at SAV.
- A live video feed with in-flight camera adjustments (ISO, shutter speed, aperture) is a valuable asset while conducting sUAS-based pavement inspections, as it allows for minute adjustments to ensure consistent and reliable data collection.
- Distresses identified in FOG surveys can be equally identified in 2-mm GSD sUAS imagery for PCI evaluation.

- Orthomosaics derived from 2-mm GSD sUAS imagery are of better quality and resolution than the DSV data.
- The ability to evaluate pavement from orthoimagery in an office environment using GIS tools ensures a quantifiable and high-accuracy analysis.
- sUAS-based pavement inspections provide digital records of pavement assets at the time of collection and can be used for change management.
- Expanding the collection area by at least two full-image frames at the beginning and end of each flight line and at least one flight line on either side of the test area resolved issues found during Phase 1 with data lost near the edge of the test area.
- Executing tests with lower overlap settings minimized field time, which increased operational efficiency. A minimum overlap setting of 40/40 leads to a full orthomosaic without any loss of data.

Table 52 and Figure 90 present the estimated amount of time required for data collection at a runway (WWD is used as an example) using a multirotor sUAS tested in this.

Table 52. Estimated Collection Time at WWD Using a Multirotor sUAS

WWD Full RWY 10/28 (150 ft X 5,000 ft)			
GSD (mm)	Overlap (Forward %/Side %)	Estimated Photo Count	Estimated Capture Time[1] (Hours)
2	80/60	N/A[2]	N/A[2]
	75/60	11,700	7.75
	60/60	7,400	5
	65/50	6,700	4.75
	50/50	**4,700**	**3.25**
	40/40	**3,300**	**2.25**
3	80/60	6,500	4.5
	75/60	5,200	3.5
	60/60	3,300	2.25
	65/50	2,300	2
	50/50	**2,100**	**1.5**
	40/40	**1,600**	**1.25**
4	80/60	3,400	2.75
	75/60	2,720	2
	60/60	1,700	1.25
	65/50	1,700	1.25
	50/50	1,200	1
	40/40	810	0.75

[1] This is only accounting for the time the sUA is flying and collecting imagery. It does not account for starting/ending flights due to battery changes (i.e., from takeoff position to start point and end point to landing position), battery changes themselves, flight line redos, or equipment troubleshooting.
[2] Cannot capture using these parameters—equipment limitation.
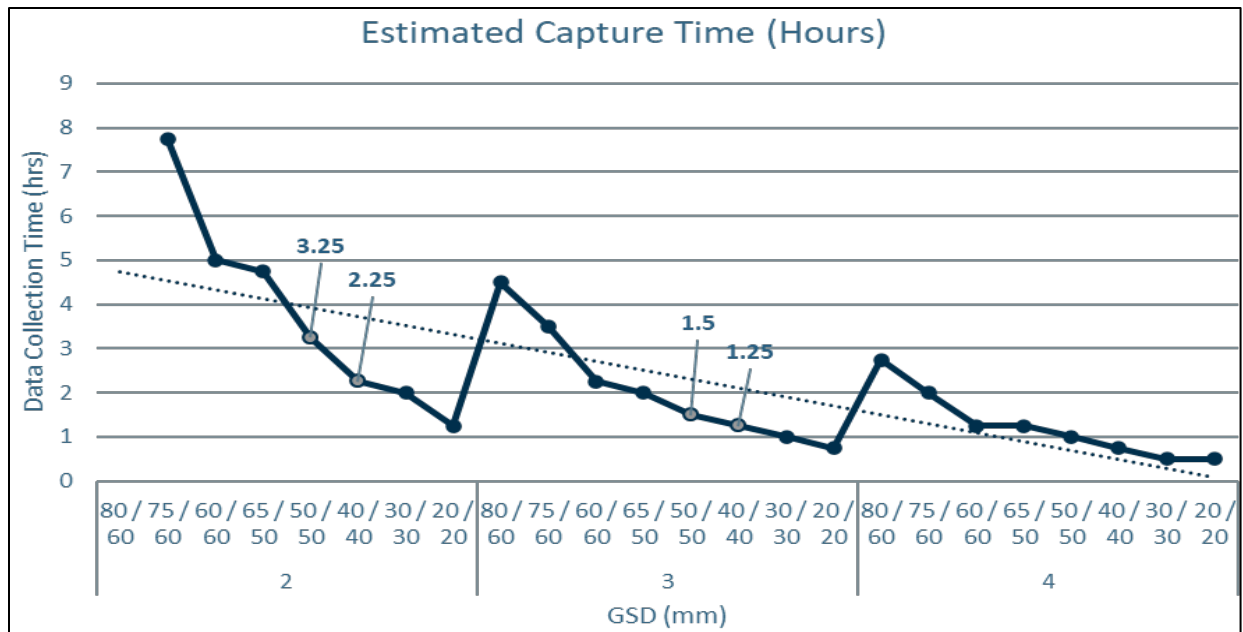
Figure 90. Estimated Collection Time at WWD using a Multirotor sUAS

5.8.1 Small Unmanned Aircraft System Data Capture Recommendations

The research team recommended the following for data capture using sUAS:

- A 2-mm GSD or smaller must be achieved.
- As validated by the testing at TTF, surveyed GCPs are recommended to ensure sufficient geolocation of the imagery, but not required.
- RTK/PPK image position corrections can be used to increase overall absolute accuracy but is not required to determine PCI values.
- The minimum forward and side overlap can vary based on the system and its capability in processing a full orthoimagery with no loss of data. The minimum forward overlap of 40% and a minimum side overlap of 40% allowed seamless orthomosaic generation.
- Due to the small GSD, extensive field QC must be done at the completion of each flight to ensure imagery is clean and usable.
- In-flight camera control allows for minute adjustments to ensure consistent and reliable data collection but is not required.

5.8.2 Small Unmanned Aircraft System Data Processing Recommendations

The research team recommended the following for processing of sUAS-acquired imagery:

- Using software that can measure GCPs and adjust camera parameters.
- Using software that can consistently produce georeferenced orthoimagery.

5.8.3 Small Unmanned Aircraft System Data Analysis and Evaluation Recommendations

The analysis and processing workflows established during Phase 1 were further refined for efficiency in Phase 2. The research team recommended the following for analyzing the processed orthoimagery:

- Georeference the sUAS imagery to directly overlay the GIS database containing section, sample, and slab layouts.
- Create three layers to map distresses: AC linear distresses, AC area distresses, and PCC point distresses.
- Create attributes for the layers including Section ID, Sample Unit ID, Slab Number (for PCC pavements), Distress, Severity, and Area/Length, which are automatically filled during the distress takeoff.
- Create a template to easily switch between distress types, which introduces the ability to assign all attributes during the inspection, limiting the time needed to evaluate the updated attributes at the end of the inspection. Update this template for each new distress throughout the analysis.
- Initially identify distresses at a zoom ratio of 1:50, zooming in to clarify severities as needed. At this zoom level, 50% to 70% of the distresses can be identified and mapped.
- Reanalyze the imagery at a 1:20 zoom ratio. This will now capture 85% to 95% of the distresses.
- Perform final analysis at a 1:10 zoom ratio to capture the smaller/less-severe distresses.
- Export the attributes tables and concatenate distresses per sample, including limiting distress to one per slab for PCC pavements.

5.9 RECOMMENDATIONS FOR FINAL VALIDATION TESTING

Based on conclusions drawn from Phase 2, the research team made the following recommendations for Validation Testing:

- Fly an entire runway to assess the feasibility of using sUAS in an airport environment for pavement inspections.
- Fly a system that was not tested during Phase 1 or Phase 2 to demonstrate viability of minimum performance standards for pavement inspections.
- Implement final Validation Testing at 2-mm GSD and 40/40 overlap settings to reduce excessive image coverage and increase time efficiency.
- Survey ground control for accuracy validation.
- Perform a cost-benefit analysis of FOG vs sUAS methods for pavement inspections.

6. VALIDATION TESTING

For Validation Testing, the research team considered the recommendations, findings, and best practices identified from Phase 1 and Phase 2. Validation Testing sought to implement an operationally efficient, full-scale test at WWD to showcase the viability and reliability of using sUAS for pavement inspections. This testing did not require data collection through FOG or

DSV methods; however, the research team had access to FOG data collected in previous phases of this research effort.

6.1 AIRPORT SELECTION

The research team selected WWD for Validation Testing, as it provides accessibility to both AC and PCC pavement surfaces with a wide variety of pavement distresses. Both Phase 1 and Phase 2 of this research effort involved testing at WWD.

6.2 TESTING METHODOLOGY

A comprehensive methodology for Validation Testing at WWD was developed in advance of mobilizing field crews to the test area. Test areas at WWD allowed the research team to validate the operational efficiency of lower forward/side overlap, validate data collection parameters with a system not tested in prior testing, and attempt to capture ASTM pavement distresses that were not previously identified in prior testing. Table 53 shows a breakdown of the testing rationale performed for Validation Testing.

Table 53. Validation Testing Methodology

Airport	Test Rationale	Test Area
WWD	Final validation—validate the operational efficiency of lower forward/side overlap, validate data collection parameters with a system not tested in prior testing, and attempt to capture ASTM pavement distresses that were not previously identified	W End RWY 10/28
		Apron (Entire AC and PCC)

6.3 SMALL UNMANNED AIRCRAFT AIRFRAMES AND SENSORS

To reflect recent industry sUAS offerings, a new airframe and sensor were introduced while performing Validation Testing. Table 54 shows a summary of this airframe, sensor, GSD, data type, and software package used in Validation Testing.

Table 54. Summary of Systems and Software Used in Validation Testing

Airframe	Sensor	GSD (mm)	Data Type	Image Processing	Data Analysis
DJI M300 RTK	P1-35mm	2	RGB	Pix4D Mapper	Esri ArcMap, FAA PAVEAIR

DJI M300 RTK, shown in Figure 91, utilized the DJI Zenmuse P1-35mm (RGB) payload. This airframe and RGB camera were identified during Validation Testing since they were an airframe and payload that were not included in any prior testing. The DJI Zenmuse P1 is a 45-megapixel camera commonly used in the surveying industry. The DJI M300 RTK with Zenmuse P1-35mm payload will herein be referred to as M300.

| (a) | (b) |

Figure 91. The DJI M300 RTK (a) with Zenmuse P1 (b)

6.4 VALIDATION TESTING—WWD

This section expands on Validation Testing performed at WWD including test areas, control data, the use of ground control, sUAS data collection parameters, data processing workflows, and data analysis for PCI.

6.4.1 Test Areas

The test areas for full-scale testing at WWD included the west end of asphalt Runway 10/28 and a GA apron (AC and PCC). When possible, the research team purposely overflew these areas to ensure full coverage across the edges of the pavement.

Figures 92 and 93 illustrate the two test areas selected for data collection.

Note: Capture limits in yellow, test limits in red.

Figure 92. West End of Runway 10/28 at WWD

Note: Capture limits in yellow, test limits in red.

Figure 93. Apron at WWD

6.4.2 Control Data

Ground control data were surveyed as part of Validation Testing but were not used in processing, as it proved to be unnecessary. The research team also had access to ground control data acquired in previous phases of this research.

6.4.3 Small Unmanned Aircraft System Data Collection Parameters

The final validation at WWD utilized a DJI M300 RTK with P1-35mm sensor at 2-mm GSD. These data were collected to validate the 2-mm GSD orthoimagery at an operationally efficient low overlap of 40/40. Table 55 presents the data collection parameters.

Table 55. Parameters for sUAS Data Collection—Validation Testing

Flight Number	Test Area	Airframe	Sensor	Data Type	Overlap (Forward/ Side)	Altitude (ft)	GSD (mm)	Actual Flight Time (min)	Actual Number Photos
1	W End RWY 10/28	M300	P1-35mm	RGB	40/40	53.75	2	35	1,350
2	Apron (AC, PCC)	M300	P1-35mm	RGB	40/40	53.75	2	29	1,256

6.4.4 Data Processing

Following initial preparation, the processing team used Pix4D Mapper to process the imagery into seamless orthomosaics. The processed data without ground control indicated negligible geographical shift with no impact on identifying and analyzing the pavement distresses.

6.4.5 Data Analysis and Evaluation

Three total test areas, including five pavement sections, were surveyed as a part of the final validation at WWD. These areas were surveyed to a lesser degree during earlier phases of research but were surveyed as per ASTM sampling requirements during this phase and represent a real-life PCI survey for an airfield.

West End of Runway 10/28

Runway 10/28 is 150 ft wide and consists of AC pavement. The pavement is divided into north, central, and southern sections and further divided into sample units as shown in Figure 94. The size of each sample unit is 50 ft x 100 ft (5,000 sq ft). Although the capture limits included 2,500 ft of the runway, the test limits only encompassed 18 sample units chosen to represent the varied conditions across the sections.
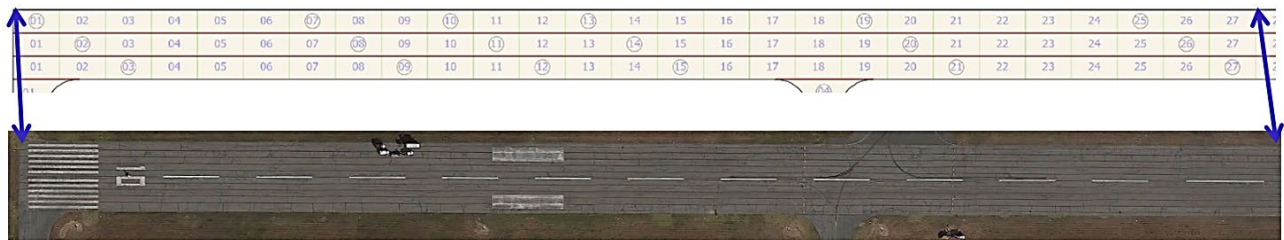
Figure 94. Sample Units of Runway 10/28 at WWD

Table 56 shows the PCI values of analyzed sample units.

Table 56. The PCI Values of Runway 10/28 at WWD

Section	Sample Number	FOG PCI	sUAS PCI	FOG Section PCI	sUAS Section PCI
10S	3	61	62	63	61
	9	65	62		
	12	65	63		
	15	66	61		
	21	59	59		
	27	62	59		
10C	2	68	67	70	64
	8	67	62		
	11	70	67		

Section	Sample Number	FOG PCI	sUAS PCI	FOG Section PCI	sUAS Section PCI
	14	76	60		
	20	71	61		
	26	70	66		
10N	1	66	68	62	64
	7	63	64		
	10	64	62		
	13	54	65		
	19	62	64		
	25	63	63		

GA Apron

The GA Apron capture limits were approximately 340 ft x 575 ft (195,500 sq ft) and consisted entirely of AC pavement. The capture limits encompassed two sections, further divided into sample units of varying size as shown in Figure 95. Although the capture limits included 38 sample units, the test limits encompassed only nine sample units chosen to represent the varied conditions across the sections.
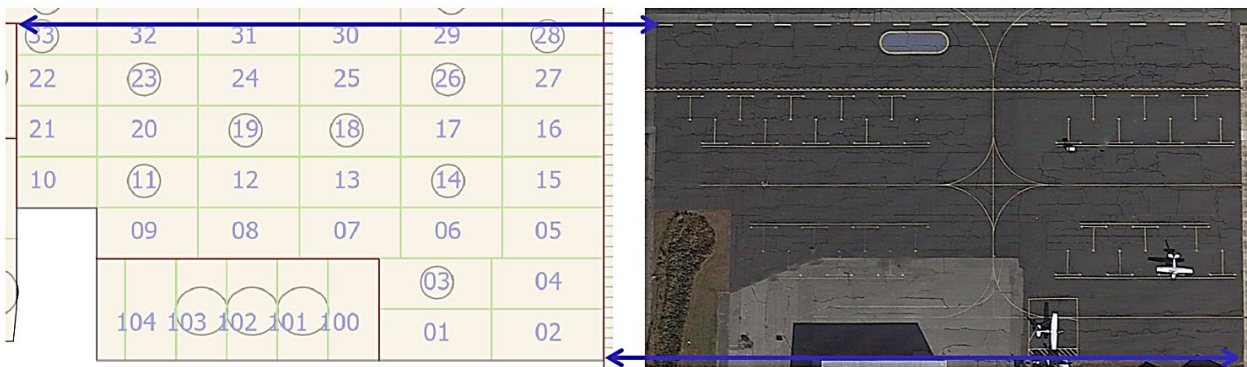
Figure 95. Sample Units of Apron Section 30 at WWD

Table 57 shows the PCI values of analyzed sample units.

Table 57. The PCI Values of Apron Section 30 at WWD

Section	Sample Number	FOG PCI	sUAS PCI	FOG Section PCI	sUAS Section PCI
30	3	58	59	59	57
	11	64	59		
	14	55	59		
	18	64	60		
	19	63	60		
	23	63	56		
	26	60	60		

Section	Sample Number	FOG PCI	sUAS PCI	FOG Section PCI	sUAS Section PCI
30	28	43	43	59	57
	33	54	51		

Terminal Apron

The Terminal Apron capture limits were approximately 470 ft x 1280 ft (433,000 sq ft) and consisted entirely of PCC pavement. The capture limits encompassed one section, further divided into sample units of varying size as shown in Figure 96. Although the capture limits included 123 sample units, the test limits encompassed only 18 sample units chosen to represent the varied conditions across the section.
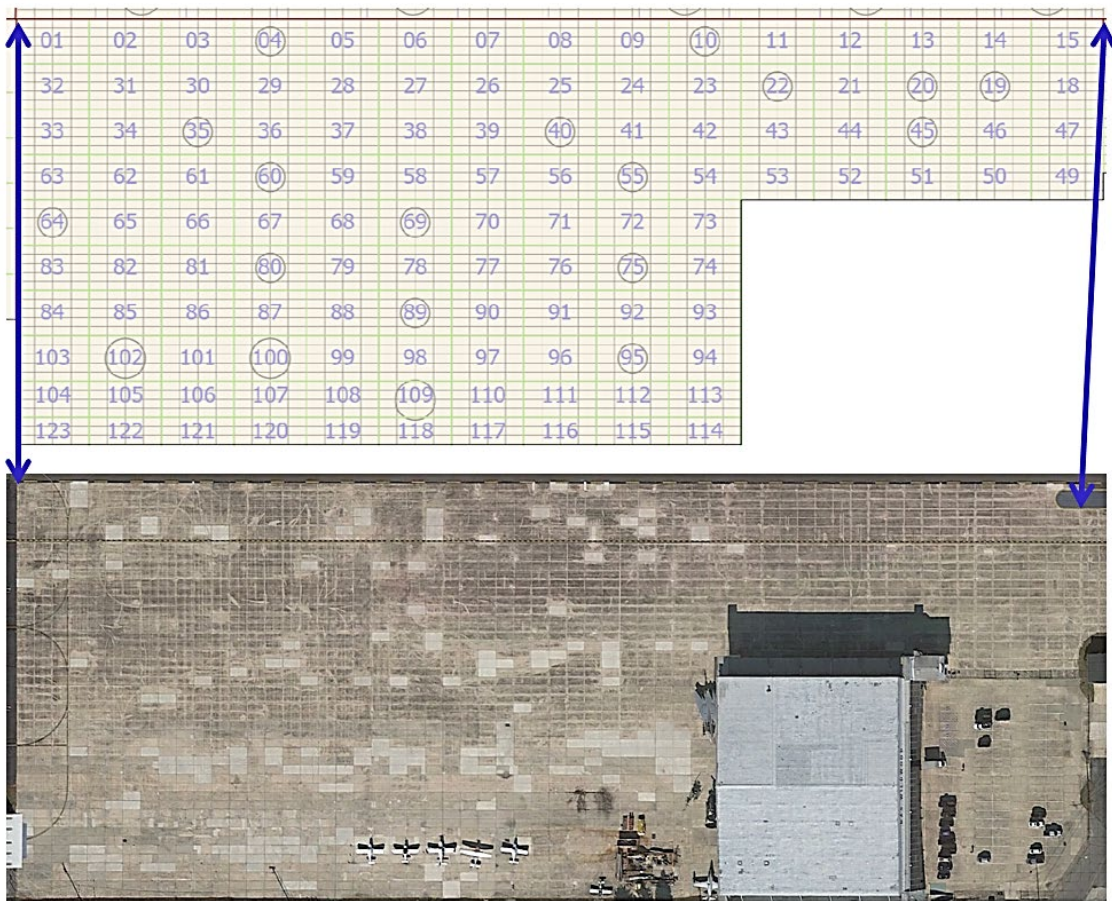
Figure 96. Sample Units of Apron Section 40 at WWD

Table 58 shows the PCI values of analyzed sample units.

Table 58. The PCI Values of Apron Section 40 at WWD

Section	Sample Number	FOG PCI	sUAS PCI	FOG Section PCI	sUAS Section PCI
40	4	73	73	61	59
	10	75	71		
	19	53	65		
	20	61	63		
	22	55	57		
	35	74	78		
	40	68	66		
	45	57	63		
	55	62	62		
	60	70	56		
	64	61	70		
	69	76	72		
	75	73	61		
	80	72	48		
	89	45	55		
	95	42	35		
	100	39	27		
	102	43	45		

All distress ratings that were used to determine the PCIs during the final validation were strictly observed via the sUAS imagery, and no field notes were used to supplement the analysis. Furthermore, these inspections were completed 16 months apart from one another, so the team expected to see further degradation of the pavements and a lower PCI for the sUAS inspection. Additionally, there is evidence that the airport had performed M&R between the inspections on the PCC Apron by means of small and large patches.

PCI values, at the section and sample level, were very consistent between the FOG and sUAS inspections. Given the age of the pavements and the geographical location of WWD, it is expected that the AC pavements would deteriorate at a rate of 2 to 3 PCI points per year and the PCC pavements at 1 to 2 PCI points per year. This is precisely what was observed in the analysis of the FOG and sUAS data, with the AC pavements deteriorating at 2.5 points per year and the PCC pavements deteriorating at 1.5 points per year on average.

Deterioration is attributed to weather-related distress increasing in severity and in quantity. The leading distress for AC pavements that contributed to this deterioration was L&T cracking. Low-severity L&T cracking increased by 17% and medium-severity L&T cracking increased by 3%. The leading distresses for PCC pavement that contributed to this deterioration were small patches, joint spalls, and corner spalls. Thirty-four additional small patches were observed during the sUAS inspection, and seven others increased from low to medium severity. That is a 28% increase in small patches and a 78% increase in medium-severity small patches.

Joint and corner spalling doubled in quantity between the inspections. It is unlikely that this large increase is strictly due to deterioration, but that the field inspector neglected smaller spalls as compared to the sUAS inspector. However, the number of medium- and high-severity spalls increased by 75%, which had a greater impact on the pavement's PCI values.

6.5 COST-BENEFIT ANALYSIS

The collection of FOG and DSV control data on Runway 10/28 at WWD during Stage 1 and the implementation of a refined sUAS workflow during Validation Testing across the same test area provided datapoints that allowed the research team to assess the cost of each pavement inspection method.

The research team used generic hourly rates and developed rough order-of-magnitude cost estimates to maintain the integrity of the analysis provided and protect confidential proprietary information. It should be noted that the costs represent an implementation of mature workflows for FOG and DSV inspections against a workflow that is validating components in a test environment. Additionally, to maintain consistency, the following assumptions were made as part of this cost analysis:

- FOG inspection costs consider a three-person crew composed of two inspectors and one driver.
- DSV cost analysis considers a two-person crew composed of one operator and one driver. Data processing for the DSV considers a 100% analysis of 150 sample units and includes one day of typical equipment fee.
- sUAS cost estimate considers additional effort for the preparation phase to account for airport coordination and airspace authorizations and represents a two-pilot crew collecting data. Data processing for the sUAS cost also considers a 100% analysis of 150 sample units and includes one day of typical equipment fee.

Table 59 summarizes an analysis that determines the cost per square yard of each pavement inspection method for Runway 10/28 at WWD.

Table 59. Cost-Benefit Analysis, FOG vs DSV vs sUAS

Based on 100% Survey of a 5,000-ft x 150-ft Runway in Fair Condition				
Data Collection Type	Process	Time (Labor Hours)	RWY Closure (Hours)	Cost per Sq Yd
FOG	Preparation	5	--	8%
FOG	Data Collection	48	12	79%
FOG	Processing/QC	8	--	13%
TOTAL FOG		61	12	$.08 - $.15
DSV	Preparation	5	--	4%
DSV	Data Collection	12	4	10%
DSV	Processing/QC	100	--	86%
TOTAL DSV		117	4	$.10 - $.25

Based on 100% Survey of a 5,000-ft x 150-ft Runway in Fair Condition				
Data Collection Type	Process	Time (Labor Hours)	RWY Closure (Hours)	Cost per Sq Yd
sUAS	Preparation	10	--	8%
sUAS	Data Collection	6	5	5%
sUAS	Processing/QC	105	--	87%
TOTAL sUAS		**121**	**5**	**$.10 - $.25**

The cost analysis indicated that, at its current level of implementation during research validation, costs associated with sUAS for pavement inspections are comparable to that of mature DSV workflows. As operational efficiencies are gained by implementing improved workflows, airframes, and sensors, these costs will be reduced further.

6.6 VALIDATION TESTING SUMMARY

The Validation Testing performed at WWD led to the following conclusions:

- A 2-mm GSD (or smaller) orthomosaic imagery derived from sUAS data collection is acceptable for PCI analysis.
- 40/40 overlap is sufficient in generating a seamless orthomosaic across the entire test area.
- Multirotor systems are typically less complicated to operate and best compensate for wind.
- The processed imagery without surveyed ground control indicates negligible geographical shift with no impact on identifying and analyzing the pavement distresses.
- Overall, it was determined that the sUAS data offer more benefits than the DSV data.
- Overall, it was determined that the sUAS is comparable to FOG in evaluating pavement health.
- Increased sensor size leads to increased operational efficiency.
- With the current stage of using sUAS for pavement inspection, the cost is comparable to DSV, however it is expected to decrease once more widely used.

7. CONCLUSIONS AND RECOMMENDATIONS

There are numerous variables that determine the success of using small unmanned aircraft systems (sUAS) for pavement inspections at an airport, i.e., longer flight times can result in extended closures of the inspection area. To use the benefits of operational efficiencies like low overlap, extensive field quality control (QC) must be performed at the completion of each flight to ensure imagery meets the standards necessary for pavement inspection.

A total of 97 mission plans were executed at the airports in varying environmental and geographic conditions resulting in approximately 1.5 terabyte of pavement imagery data collected and analyzed for pavement distress per ASTM standards. Additionally, under the direction of the FAA, two technical interchange meetings were held with the Michigan Technological Research Institute, Iowa State University, and APTech research teams that were

performing research concurrently. These interchanges provided opportunities for both teams to share findings, validations, and best practices.

All analyzed data sets can be viewed in their full resolution using the Geographical Information System (GIS) tool[3] created by the research team.

While no system can be deemed the definitive minimum, some features and capabilities, such as airframe/sensor characteristics and product requirements, must be accounted for. Therefore, the research team produced a performance report that establishes key recommendations and requirements for successful execution of sUAS-based pavement inspections. The rapidly evolving sUAS industry could present improved and more efficient technologies in the future, which could require re-evaluation of currently recommended minimum performance standards.

7.1 DISTRESS IDENTIFICATION MATRIX FOR ASPHALT CONCRETE

The research team developed a distress identification matrix, shown in Table 60, that lists all airport pavement distresses. This matrix shows a comparison of the distresses identified via foot-on-ground (FOG), digital survey vehicle (DSV), and sUAS on asphalt concrete (AC) surface.

Table 60. Distress Identification Matrix—AC Surface

Distress Breakdown	FOG	DSV (Manual)	DSV (Automated)	sUAS (Manual)
Alligator Cracking	✓	✓	✓	✓
Bleeding	✓	✓		✓
Block Cracking	✓	✓		✓
Corrugation	✓			
Depression	✓			
Jet Blast				
Joint Reflection Crack	✓	✓		✓
L&T Crack	✓	✓	✓	✓
Oil Spillage	✓			
Patching	✓	✓		✓
Polished Aggregate	✓			✓
Raveling	✓	✓		✓
Rutting	✓	✓	✓	
Shoving	✓	✓	✓	
Slippage Crack		✓		✓

---

[3] GIS tool
Login Details:
Username: faa_collaboration
Password - Woolpert-FAA-2021GO!

Distress Breakdown	FOG	DSV (Manual)	DSV (Automated)	sUAS (Manual)
Swelling	✓			
Weathering	✓	✓		✓

Distresses such as rutting and shoving can be identified via DSV but not sUAS (Red, Green, Blue [RGB]). Because of DSV's laser-based imagery collection, DSV can more accurately determine elevation differences and can therefore identify those distresses. However, it is an output that needs to be carefully and manually QC-ed since the processing software does not take into consideration the location of the vehicle, i.e., if the vehicle is in a wheel path or at a pavement change.

7.1.1 Longitudinal & Transverse Cracking

Figures 97 through 103 show photographs comparing AC distresses from FOG and sUAS inspections. Some AC distresses were not captured during the FOG data collection but were identified in these sUAS data sets.

Figure 97 illustrates low-severity longitudinal and transverse (L&T) cracking as identified at WWD via FOG and sUAS inspections.

(a)   (b)
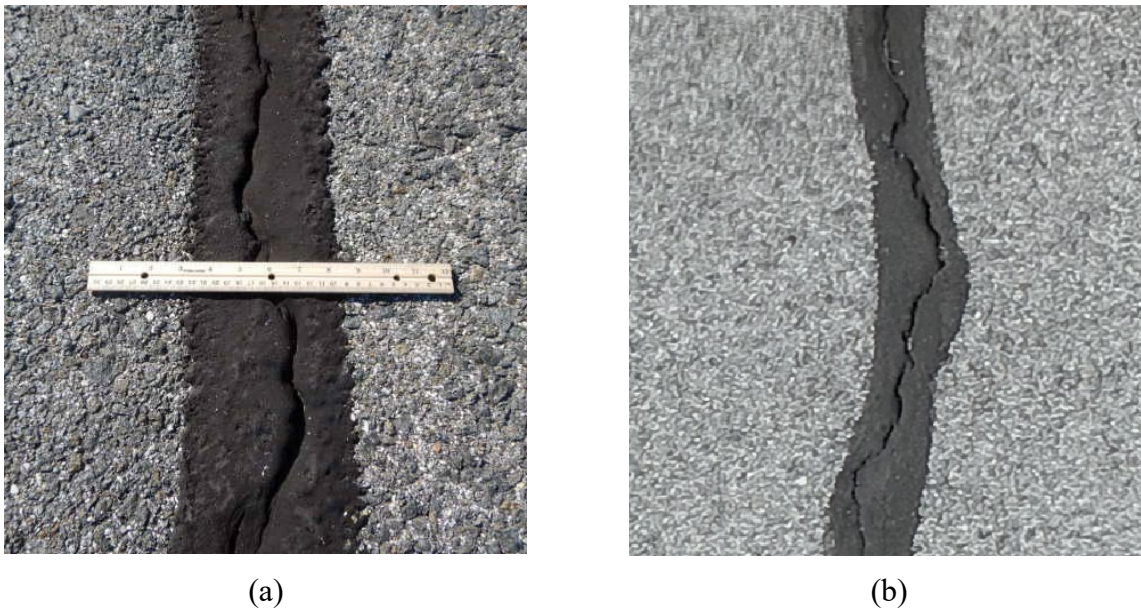
Figure 97. Low-Severity L&T Cracking Detected via FOG (a) and sUAS (b) Inspections

Figure 98 illustrates medium-severity L&T cracking as identified at WWD via FOG and sUAS inspections.

<center>(a)</center>

<center>(b)</center>

Figure 98. Medium-Severity L&T Cracking Detected via FOG (a) and sUAS (b) Inspections

Figure 99 illustrates high-severity L&T cracking as identified at Cape May County Airport (WWD) via FOG and sUAS inspections.

<center>(a)</center>
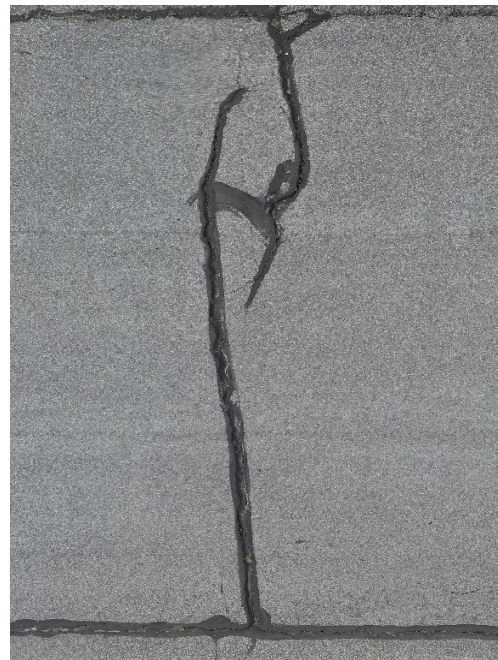
<center>(b)</center>

Figure 99. High-Severity L&T Cracking Detected via FOG (a) and sUAS (b) Inspections

7.1.2 Raveling

Figure 100 illustrates low-severity raveling as identified at WWD via FOG and sUAS inspections.

(a)   (b)

Figure 100. Low-Severity Raveling Detected via FOG (a) and sUAS (b) Inspections

Figure 101 illustrates medium-severity raveling as identified at WWD via FOG and sUAS inspections.

(a)   (b)
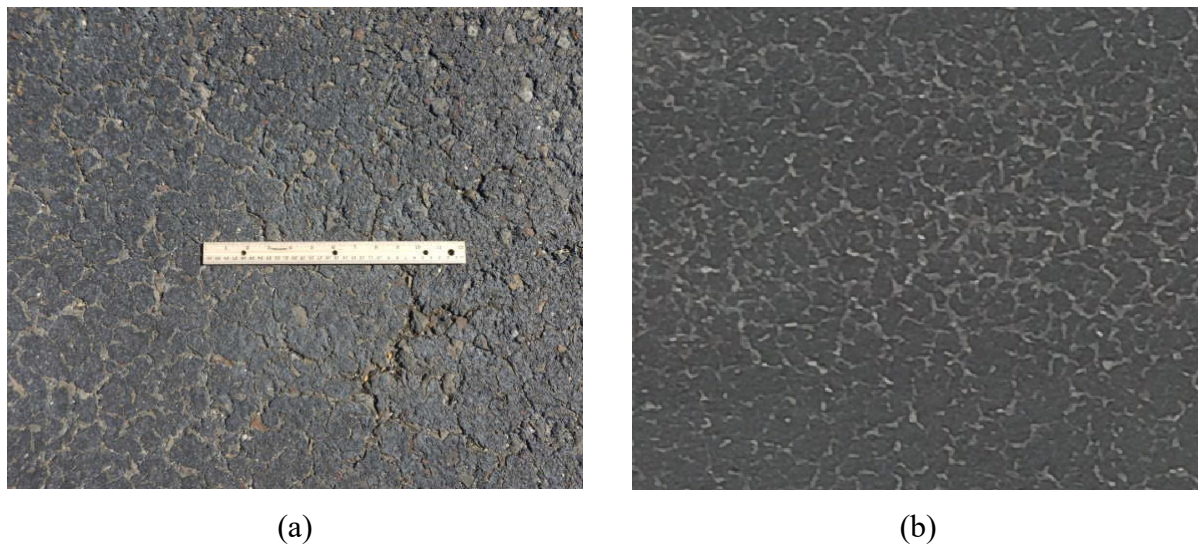
Figure 101. Medium-Severity Raveling Detected via FOG (a) and sUAS (b) Inspections

7.1.3 Weathering

Figure 102 illustrates low-severity weathering as identified at WWD via FOG and sUAS inspections.

<div style="text-align:center">(a)   (b)</div>

Figure 102. Low-Severity Weathering Detected via FOG (a) and sUAS (b) Inspections

Figure 103 illustrates medium-severity weathering as identified at WWD via FOG and sUAS inspections.

<div style="text-align:center">(a)   (b)</div>

Figure 103. Medium-Severity Weathering Detected via FOG (a) and sUAS (b) Inspections

7.2 DISTRESS IDENTIFICATION MATRIX FOR PORTLAND CEMENT CONCRETE

The research team developed a distress identification matrix that lists all airport pavement distresses. Table 61 presents this matrix, which shows a comparison of the distresses identified via FOG, DSV, and sUAS on Portland cement concrete (PCC) surface.

Table 61. Distress Identification Matrix—PCC Surface

Distress Breakdown	FOG	DSV (Manual)	DSV (Automated)	sUAS (Manual)
Blowup	✓	✓		
Corner Break	✓	✓		✓
Linear Crack	✓	✓	✓	✓
Durability Cracking	✓	✓		✓
Joint Seal Damage	✓	✓		✓
Small Patch	✓	✓		✓
Large Patch	✓	✓		✓
Pop-outs	✓	✓		✓
Pumping	✓			✓
Scaling	✓			✓
Faulting	✓	✓	✓	
Shattered Slab	✓	✓		✓
Shrinkage Crack	✓	✓		✓
Joint Spall	✓	✓		✓
Corner Spall	✓	✓		✓
Alkali-Silica Reaction	✓	✓		✓

Figures 104 through 117 show photographs comparing PCC distresses from FOG and sUAS inspections. Some PCC distresses were not captured during the FOG data collection but were identified in the sUAS data set.

7.2.1 Corner Break

Figure 104 compares low- vs medium-severity corner break as identified at WWD via sUAS inspections.

(a)   (b)

Figure 104. Low- (a) vs Medium-Severity (b) Corner Break Detected via sUAS Inspections

7.2.2 Linear Crack

Figure 105 illustrates a low-severity linear crack as identified at WWD via FOG and sUAS inspections.

(a) (b)

Figure 105. Low-Severity Linear Crack Detected via FOG (a) and sUAS (b) Inspections

Figure 106 illustrates medium-severity linear crack with seal no longer bonded to PCC as identified at WWD via sUAS inspections.

Figure 106. Medium-Severity Linear Crack Detected via sUAS Inspections

7.2.3 Small Patch

Figure 107 illustrates low-severity small patch as identified at WWD via FOG and sUAS inspections.

<table>
<tr><td>(a)</td><td>(b)</td></tr>
</table>
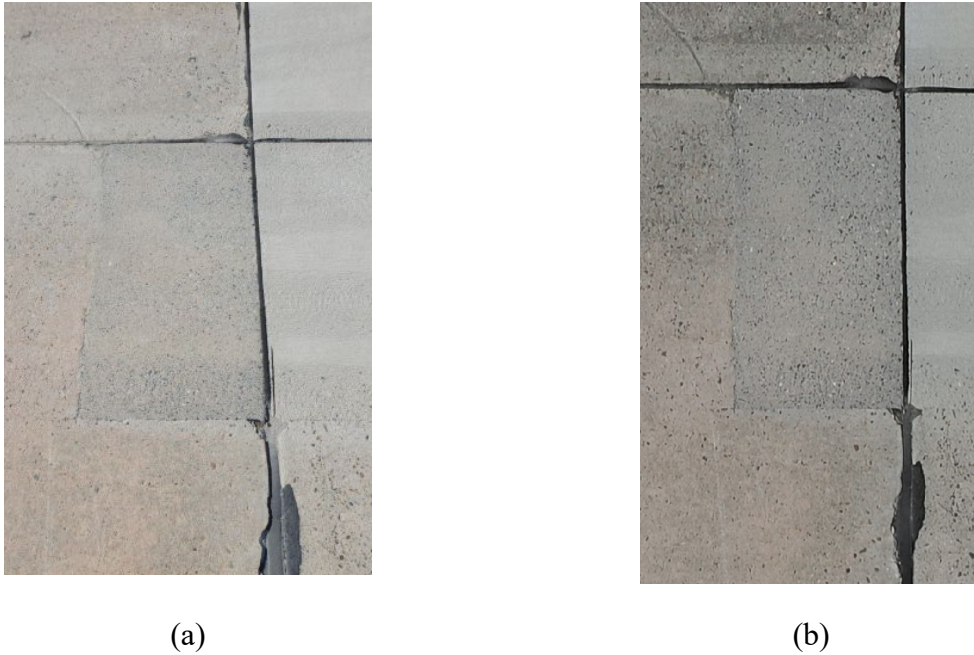
Figure 107. Low-Severity Small Patch Detected via FOG (a) and sUAS (b) Inspections

Figure 108 compares medium- vs high-severity small patch as identified at WWD via sUAS inspections.

<table>
<tr><td>(a)</td><td>(b)</td></tr>
</table>

Figure 108. Medium- (a) vs High-Severity (b) Small Patch Detected
via sUAS Inspections

7.2.4 Large Patch

Figure 109 illustrates low-severity large patch as identified at WWD via FOG and sUAS inspections.

| (a) | (b) |
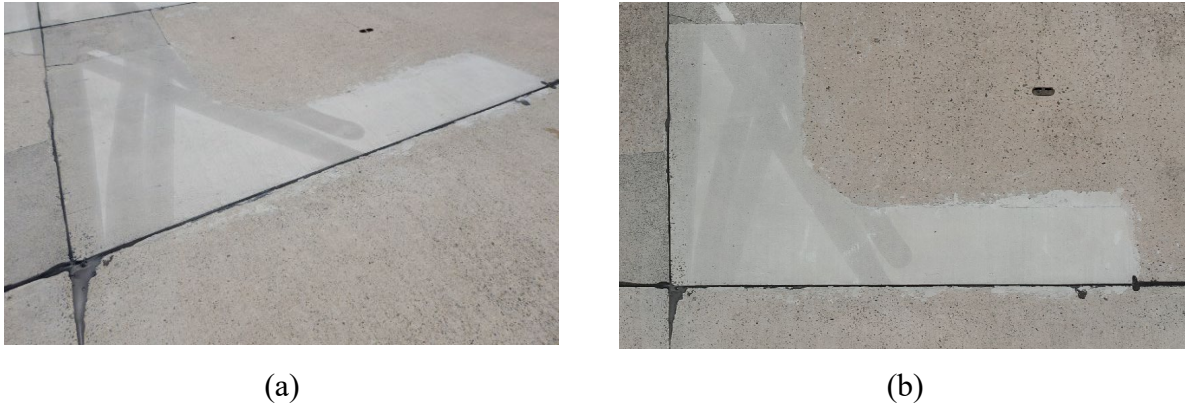
Figure 109. Low-Severity Large Patch Detected via FOG (a) and sUAS (b) Inspections

Figure 110 illustrates medium-severity large patch as identified at WWD via FOG and sUAS inspections.

| (a) | (b) |
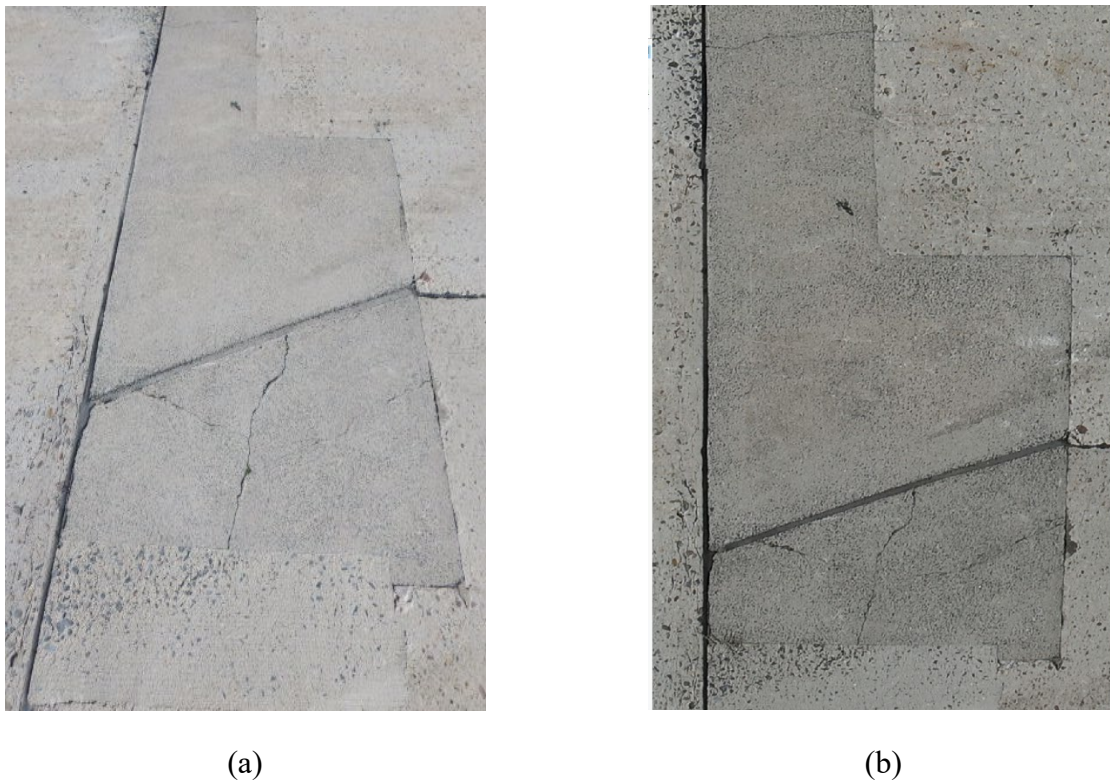
Figure 110. Medium-Severity Large Patch Detected via FOG (a) and
sUAS (b) Inspections

7.2.5 Scaling

Figure 111 compares low-severity vs medium-severity scaling as identified at WWD via sUAS inspections.

<div align="center">(a)   (b)</div>

Figure 111. Low- vs Medium-Severity Scaling Detected via sUAS Inspections

7.2.6 Shrinkage Crack

Figure 112 illustrates shrinkage crack as identified at WWD via FOG and sUAS inspections.

<div align="center">(a)   (b)</div>
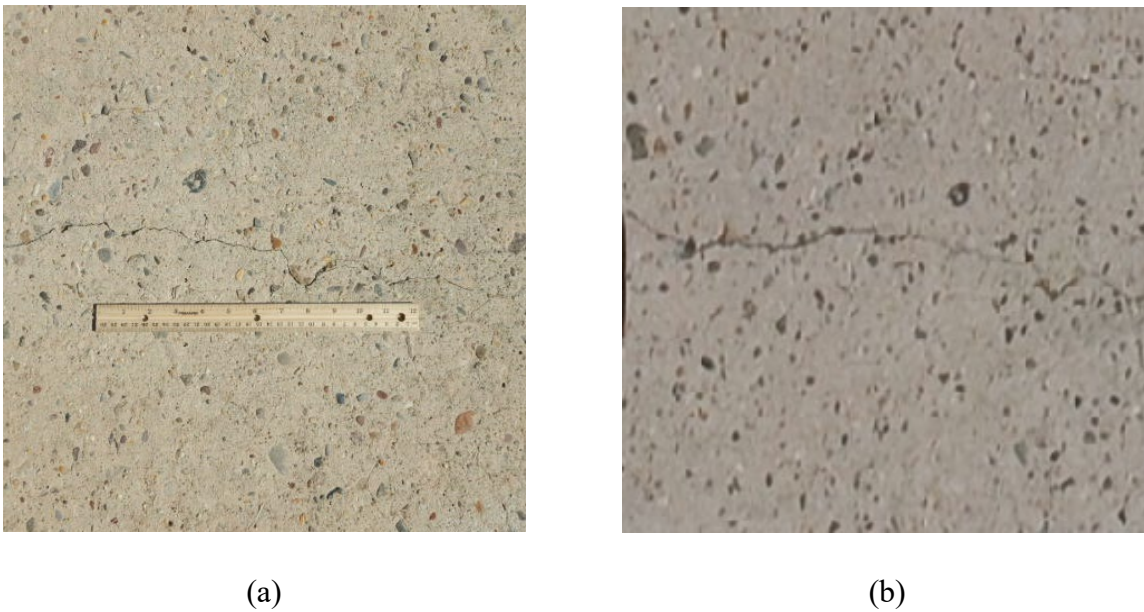
Figure 112. Shrinkage Crack Detected via FOG (a) and sUAS (b) Inspections

7.2.7 Joint Spall

Figure 113 compares low-, medium-, and high-severity joint spall as identified at WWD via sUAS inspections.

<div align="center">(a)   (b)   (c)</div>
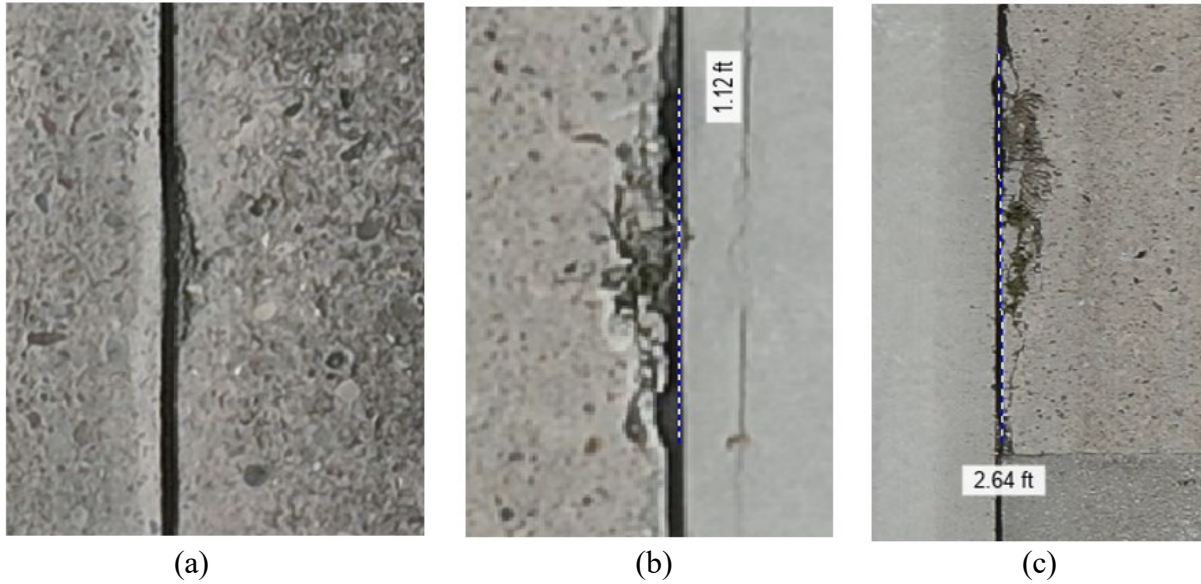
Figure 113. Low- (a), Medium- (b), and High-Severity Joint Spall Detected via sUAS (c) Inspections

7.2.8 Corner Spall

Figure 114 illustrates low-severity corner spall as identified at WWD via sUAS inspections.

Figure 114. Low-Severity Corner Spall Detected via sUAS Inspections

Figure 115 illustrates medium-severity corner spall as identified at WWD via FOG and sUAS inspections.

<center>(a)</center> <center>(b)</center>

<center>Figure 115. Medium-Severity Corner Spall Detected via FOG (a) and sUAS (b) Inspections</center>

Figure 116 illustrates high-severity corner spall as identified at WWD via FOG and sUAS inspections.
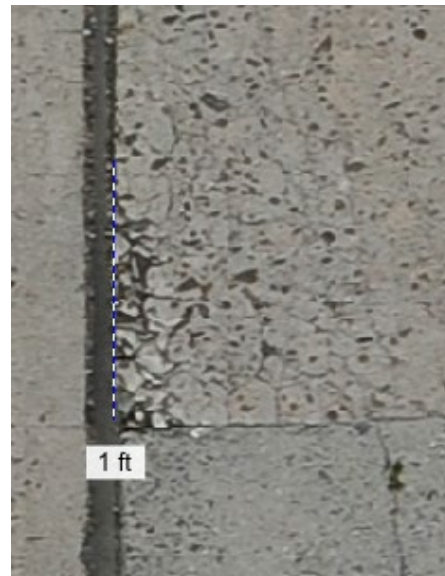
<center>(a)</center> <center>(b)</center>

<center>Figure 116. High-Severity Corner Spall Detected via FOG (a) and sUAS (b) Inspections</center>

7.2.9 Alkali-Silica Reaction

Figure 117 compares low-, medium-, and high-severity ASR as identified at WWD via sUAS inspections.

<center>128</center>

(a)

(b)

(c)
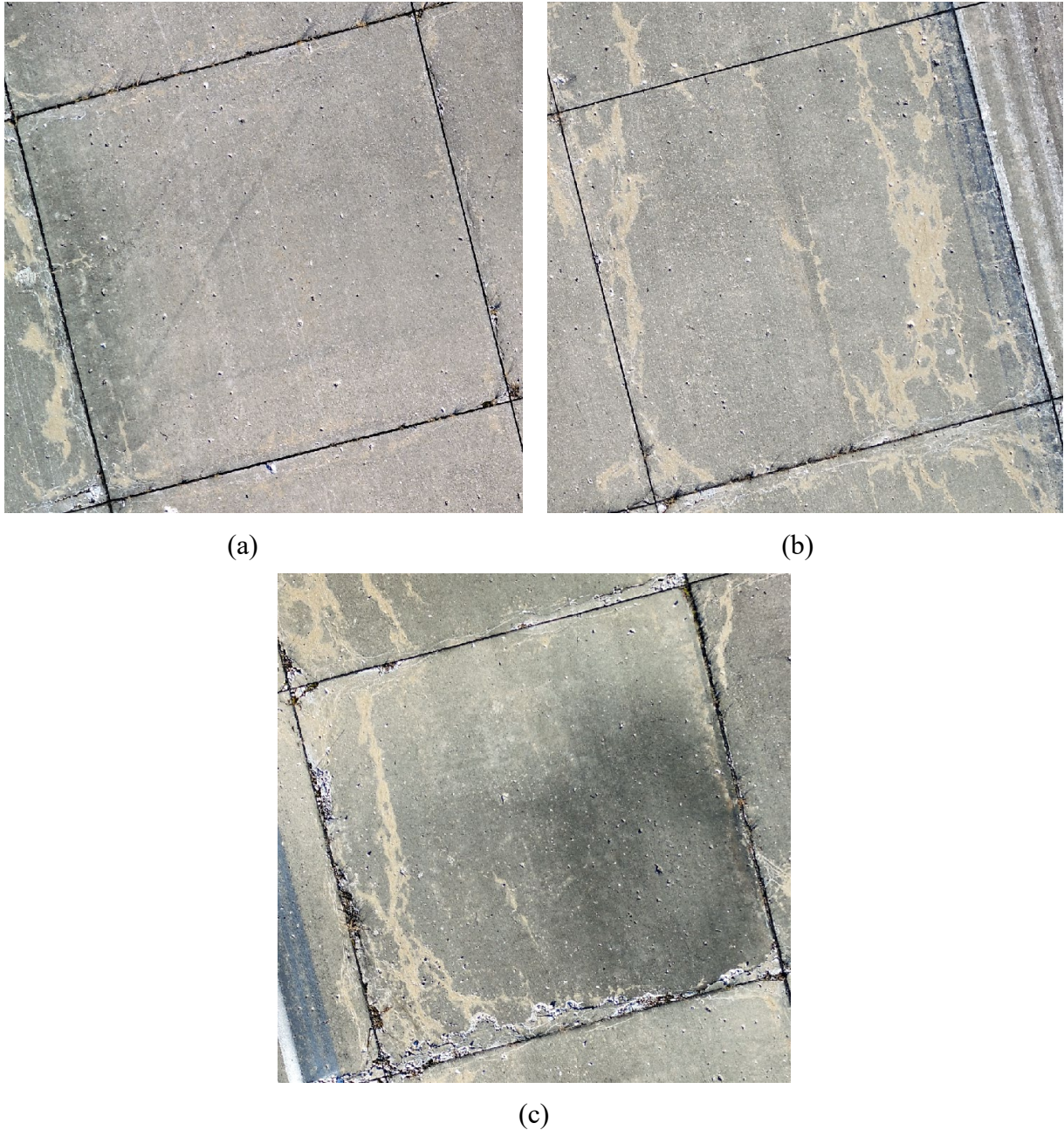
Figure 117. Low-(a), Medium- (b), and High-Severity (c) ASR Detected via sUAS Inspections

7.3 RESEARCH GAPS AND RECOMMENDATIONS FOR FURTHER TESTING

The research team identified several gaps at the time of this research. These gaps merit additional research and investigation, as follows:

- Conduct further study on LiDAR sensors to evaluate and quantify depth- and elevation-related distresses.
- Test additional integrations of aircraft airframes and sensors.
- Test additional software packages.

- Collect data in additional lighting and environmental conditions.
- Explore application of artificial intelligence (AI) for pavement distress data analysis, which is the focus of significant research and development. Incorporating its use into a standard, repeatable set of processes and procedures for sUAS data analysis and reporting has the potential to automate distress identification.
- Test the application potential of hyperspectral imagery and ground-penetrating radar (GPR) for PCI analysis. Hyperspectral sensors possess the ability to detect a surface's chemical and mineral properties while GPR sensors can determine subsurface conditions through nondestructive testing.

8. REFERENCES

AASHTO. (2018). *35 State DOTs are Deploying Drones to Save Lives, Time and Money*. https://dailyupdate.transportation.org/Pages/NewsReleaseDetail.aspx?NewsReleaseID=1504

AASHTO. (2019). *UAS/Drone Survey of All 50 State DOTs*. https://uas-aam.transportation.org/wp-content/uploads/sites/69/2022/06/Drone-Survey-2019.pdf

ASTM International. (2020). *Standard Test Method for Airport Pavement Condition Index Surveys* (ASTM D5340-20). https://www.astm.org/d5340-20.html

Federal Aviation Administration. (2014). *Guidelines and Procedures for Maintenance of Airport Pavements* and 150/5380-7B, *Airport Pavement Management Program*. https://www.faa.gov/documentlibrary/media/advisory_circular/150-5380-7b.pdf

International Organization for Standardization (ISO). (2000). *Photography—Electronic still picture imaging—Resolution and spatial frequency responses* (ISO Standard 12233:2000).

Woolpert, Inc. (2023). *Small unmanned aircraft systems (sUAS) for pavement inspections performance specifications report* [Unpublished report].

APPENDIX A—LITERATURE REVIEW

A.1 ACRONYMS AND ABBREVIATIONS

5A9	Roosevelt Memorial Airport
ACRP	Airport Cooperative Research Program
AFN	Jaffrey Airport
AI	Artificial Intelligence
AJR	Habersham County Airport
AMG	Automated Machine Guidance
ATL	Hartsfield-Jackson Atlanta International Airport
BCA	Benefit-Cost Analysis
CMOS	Complementary Metal-Oxide Semiconductor
CNN	Convolutional Neural Network
DL	Deep learning
DOT	Department of Transportation
DSV	Digital survey vehicle
DTM	Digital terrain model
FAA	Federal Aviation Administration
FHWA	Federal Highway Administration
FMA	Fitchburg Municipal Airport
FOG	Foot-on-Ground
FTG	Front Range Airport
GDOT	Georgia Department of Transportation
GIT	Georgia Institute of Technology
GNSS	Global navigation satellite system
GPR	Ground-penetrating radar
GSD	Ground sampling distance
IP	Image Processing
IRT	Infrared thermography
ITV	Iterative tensor voting
JNX	Johnston Regional Airport
KTH	Kungliga Tekniska Högskolan
MassDOT	Massachusetts Department of Transportation
MAVLink	Micro Air Vehicle Link
MDOT	Michigan Department of Transportation
ML	Machine learning
NAS	National Airspace System
NDVI	Normalized Difference Vegetation Index
NHDOT	New Hampshire Department of Transportation
NIOSH	National Institute of Occupational Safety and Health
NN	Neural Networks
PMP	Pavement Management Program
PPK	Post-processing kinematic
RAM	Random-access memory
ROI	Return on investment
RTK	Real-time kinematic

SfM	Structure from motion
SPR	State Planning and Research
sUAS	Small Unmanned Aircraft System
SWIR	Short-wavelength infrared
TLS	Terrestrial Laser Scanning
UAS	Unmanned aircraft system
USDOT	U.S. Department of Transportation

A.2 INDUSTRY LITERATURE REVIEW

The research team conducted an extensive review of industry and academic literature on successful implementation of small unmanned aircraft system (sUAS) technologies for applications related to pavement, roadway, railroad, bridges, construction, monitoring, and inspection. This section details the key pieces of literature relevant to this research.

A.2.1 Massachusetts Department of Transportation (Mogawer et al., 2019)

In 2019, the Massachusetts Department of Transportation (MassDOT) used sUAS to assess roadway pavement condition (Mogawer et al., 2019). This research program, supported via the Federal Highway Administration (FHWA) State Planning and Research (SPR) funds, had two main objectives:

(1) Perform a review of existing sUAS technologies for pavement condition survey.
(2) Conduct a pilot study to evaluate the applicability of using sUAS for pavement condition analysis.

A literature review was conducted on the use of sUAS technologies for data collection and deep learning applications. Based on the results reflected in the literature review, the research team observed and experimented with the use of two different methods of pavement crack detection. One was the MATLAB CrackIT toolbox, and the other was a deep-learning algorithm (convolutional neural network algorithm).

The research team used sUAS to collect two sets of data at the Fitchburg Municipal Airport (FMA), in addition to those previously acquired by the MassDOT Aeronautics Division. As part of the data collection effort at FMA, several heights were tested to find the optimal altitude at which cracks in the pavement are still identifiable. Table A-1 identifies a summary of tested parameters for data collection.

Table A-1. Massachusetts Department of Transportation Data Collection Parameters

Airframe/Sensor	Altitudes Tested (ft)	Coverage	Flight Description
DJI Matrice 210/XT2 Dual	10–70 (at a 5-ft interval), 80–150 (10-ft interval), and 200	Single Point	Elevator flight, visual and thermal cameras
DJI Inspire 2/X4S	32, 40, 50, and 60	Half Runway	Coverage flight, visual camera
	70, 90, 120, and 200	Full Runway	

The pavement evaluation from collected images was performed using a MATLAB toolbox called CrackIT and two deep-learning approaches, Feature Pyramid and Hierarchical Boosting Network (FPHBN) and U-Net. The online image data set was used to train the deep-learning models via transfer learning.

For data collection using sUAS, the study suggested that a 50-ft altitude provided balanced efficiency and accuracy for crack detection applications and resulted in 0.16 in. per pixel ground sampling distance (GSD). The study found that the increase in flight altitude had a negative impact on the image quality. Additionally, the image quality associated with thermal imagery did not exhibit clearer characteristics compared to the red, green, blue (RGB) imagery and was therefore removed from further consideration.

Deep-learning models outperformed the MATLAB CrackIT toolbox, but these models required pixel-level ground marking to be successfully applied in image analysis. The ground marking is done manually and, therefore, requires significant effort in visual detection of pavement distresses to be effective. The time-intensive job of annotating a training data set can be an obstacle to the successful application of deep-learning models in pavement crack detection. Furthermore, the research suggested that combining a multirotor platform with selected cameras proved to be feasible in the data collection efforts and provided useful crack information with the deep learning methods. (Mogawer et al., 2019)

A.2.2 Michigan Department of Transportation (Brooks et al., 2018)

A 2018 study conducted by the Michigan Department of Transportation (MDOT) conducted field tests with five distinct airframes equipped with thermal, visual, and light detection and ranging (LiDAR) sensors to determine their implementation into MDOT workflows for transportation infrastructure inspections (Brooks et al., 2018). Field demonstrations included bridges, roadway corridors, construction sites, and highways, and data were processed using customized algorithms and tools. A cost-benefit analysis of manual vs automated bridge evaluation techniques and an implementation plan were also presented in a separate report.

The team performed ten tests that used five different airframes and eight different sensors and covered four different types of infrastructure environments and needs. While the study did not share any flight parameters, such as GSD and altitude, Table A-2 summarizes the test sites, systems selected, and deliverables.

Table A-2. Michigan Department of Transportation Field Tests

Test Site	Platforms Used	Deliverables Produced
South Warren Road Bridge: hot mix asphalt with some delamination and a surface condition rating of 5	Bergen Hexacopter/Nikon D810/ FLIR Vue Pro DJI Phantom 3A	Orthophotos, Digital Elevation Model, hillshade, thermal imagery
Gordonville Road Bridge: concrete with some spalling and a surface condition rating of 5	Bergen Hexacopter/Nikon D810/ FLIR Vue Pro DJI Phantom 3A	Orthophotos, Digital Elevation Model, hillshade, thermal imagery

Test Site	Platforms Used	Deliverables Produced
I-75/Square Lake Road: construction site (no pavement, aggregate mound)	Riegl Ri-COPTER/LiDAR unit Bergen Hexacopter/Nikon D810	Point cloud data, orthophotos, Digital Elevation Model, hillshade
Uncle Henry Road: concrete with several spalls and delamination and a surface rating of 5	Bergen Hexacopter/Nikon D810/ FLIR Vue Pro DJI Phantom 3A	Orthophotos, Digital Elevation Model, hillshade, thermal imagery
Beyer Road/STR 9293: concrete bridge deck with spalling and delamination and a surface rating of 5	Bergen Hexacopter/Nikon D810/ FLIR Vue Pro DJI Phantom 3A	Orthophotos, Digital Elevation Model, hillshade, thermal imagery
M-120/Holton Road: 0.23-mile asphalt roadway corridor	Bergen Hexacopter/Nikon D810/ FLIR Vue Pro/FLIR Vue Pro R DJI Phantom 3A DJI Mavic Pro	Orthophotos, Digital Elevation Model, hillshade, thermal imagery, traffic video
US-31/White River Corridor: 169-ft concrete bridge deck with several delaminations and a pavement surface rating of 4	Bergen Hexacopter/ Nikon D810/ FLIR Vue Pro/ FLIR Vue Pro R/ FLIR Duo/ GoPro Hero 3 DJI Phantom 3A DJI Mavic Pro	Orthophotos, Digital Elevation Model, hillshade, thermal orthophotos
Merriman Road: 176-ft concrete bridge deck with several patched spallings and a surface rating of 4	Bergen Hexacopter/ Nikon D800/ FLIR Tau2	Orthophotos, Digital Elevation Model, hillshade, thermal orthophotos
MTRI Highway Corridor: concrete highway corridor, good condition	DJI Mavic Pro	4K Video
MTRI Highway/US 23: asphalt roadway	Bergen Hexacopter/ Velodyne LP-16 LiDAR unit	Point Cloud

The study suggested that implementation of sUAS within MDOT workflows had several benefits in detecting bridge deck surface and subsurface conditions, including spalls and delamination, through optical and thermal imagery; monitoring and quantifying construction surface elements; low-cost traffic monitoring; and identifying inventory of roadway assets. Table A-3 presents the suggested combination of airframes and sensors.

Table A-3. Combination of Airframes and Sensors

Platform	Sensors	Conclusion
Bergen Hexacopter	Optical and Thermal	Most appropriate for high-resolution imaging of transportation infrastructure
Bergen, Quad-8 Octocopter	Optical and LiDAR	Most appropriate for flying both sensors simultaneously for testing purposes and along a road corridor
DJI Phantom 3A	Optical	Most useful for rapid overview imaging of bridges and road corridors
DJI Mavic Pro	Optical	Most useful for rapid overview imaging of a scene, traffic monitoring video, and close imagery of the side of a bridge
The Mariner 2 Splash	Optical	Most useful for collecting imagery under a bridge

The cost-benefit analysis suggested that the manual bridge evaluation techniques over-estimated the distresses, which led to higher maintenance costs as compared to the accuracy of sUAS, which possessed lower maintenance costs and improved deterioration modeling. (Brooks et al., 2018)

A.2.3 Airport Cooperative Research Program (Booz Allen Hamilton, 2020b)

Established in 2005 by the FAA, the Airport Cooperative Research Program's (ACRP) goal is to solve common problems, learn about new technologies, and assess innovations in service and operations through research efforts. ACRP Report 212, published in 2020, provides guidance for airports on unmanned aircraft system (UAS) applications and discusses the use of UAS in pavement inspections. The report considers pavement inspections among the most common types of UAS use cases and explores its potential implementation in the short term. UAS can improve the efficiency of the current process by inspecting runways, taxiways, aprons, and ramps to meet any FAA-mandated condition levels. The report discusses the three steps required in UAS operations (pre-planning coordination, flight planning, and executing the operation) in detail and provides successful case studies of high-resolution imagery data collection that were used to determine pavement conditions at Front Range (FTG) and Johnston Regional (JNX) Airports. (Booz Allen Hamilton, 2020b)

The following ACRP research guidance (listed in Table A-4) was reviewed and considered as part of this research effort.

Table A-4. Airport Cooperative Research Program Research References

Report Number	Report Name
ACRP Research Report 212, Volume 3 (Booz Allen Hamilton, 2020b)	*Airports and Unmanned Aircraft Systems: Potential Use of UAS by Airport Operators*
ACRP Research Report 212, Volume 2 (Booz Allen Hamilton, 2020a)	*Airports and Unmanned Aircraft Systems: Incorporating UAS into Airport Infrastructure Planning Guidebook*

Report Number	Report Name
ACRP Synthesis 104 (Prather, 2019)	*Current Landscape of Unmanned Aircraft Systems at Airports*

A.2.4 Federal Highway Administration

Report FHWA-HIF-19-089, *Effective Use of Geospatial Tools in Highway Construction* (Jagannath et al., 2018), provides a look at the past, current, and future of the industry's use of new technology, such as UAS, LiDAR, and photogrammetry. The report examines the benefits and limitations of using various geospatial technologies. Of interest to this research were those that relate to UAS. It was observed that the industry in general was exploring the use of UAS for

- Surveillance and traffic monitoring
- Structural inspections
- Construction safety inspection and security
- Pavement inventory collection, pavement condition assessment, and inspection
- Topographic mapping and earthwork quantities assessment
- Construction progress monitoring
- Slope stability assessment
- Crash investigation

The report tracks the growth of geospatial technologies and introduces commonly used ones like UAS, LiDAR, Photogrammetry, structure from motion (SfM), and Global Navigation Satellite System (GNSS), and also presents the current status and details of spinoffs like automated machine guidance (AMG), ground-penetrating radar (GPR), and total stations. The report investigates the benefits, challenges, and existing and potential uses of these technologies. The UAS used in the study included multicopters and helicopters, as summarized in Table A-5.

Table A-5. Use Cases for UAS

Operator	Platforms	Purpose
Ohio State University for Ohio DOT	senseFly's albris sUAS	Bridge inspections.
Utah DOT	senseFly's albris, Phantom4, and the 3DR Solo system	Evaluate sUAS's ability to deliver 3D imagery/models, perform topographic mapping, compute construction quantities, and perform construction inspection.
Ohio DOT	Aibotix Aibot X6 Hexacopter with traditional RGB cameras	Ohio DOT's intent was to help survey areas designated for construction. Finding: a learning curve for surveying (specifically the post-processing of imagery), limited vertical accuracy.
Large Highway Contractor #1; sUAS operations from NV regional office	Five sUAS operated in different offices, in-house data processing	Stockpile monitoring, construction inspection, surveillance of environmentally sensitive areas, pre-construction records.

Operator	Platforms	Purpose
Large Highway Contractor #2: rent sUAS	Multi/Quadcopter	Imagery capture for photogrammetry and generating 3D surfaces, construction inspection, stockpile monitoring, accurate logistic planning.
Geospatial Service Company	Operates multiple sUAS—multicopters, fixed-wing aircraft	Drones as a service, construction progress, earthwork quantity estimation, intermediate as-builts.

The authors found that highway contractors and geospatial services companies (e.g., Woolpert) were the early adopters of this technology, but State Departments of Transportation (DOTs) also realized that these systems could increase efficiency. The delay in adoption of these tools at the time of writing this report were attributed to the difficulty in quantifying the return on investment (ROI). However, many State DOTs have overcome this challenge and are finding that these tools allow them to increase staff utilization and productivity with fewer resources. The report includes case studies and details gleaned from discussions with highway contractors and geospatial service providers along with sample benefit cost analysis (BCA) and ROI calculations.

The major benefits of UAS use were found to be in enhancing safety through reducing the requirement of human inspectors, improving construction reporting via high-resolution imagery and videos, and real-time construction quantity monitoring. UAS can typically fly a diverse set of sensors to collect different data types. In some cases, UAS can also access areas that can be difficult or dangerous to reach. With its smaller cost, as compared to fixed-wing aircraft, the ability to perform repetitive flights allows for change detection capability. And unlike fixed-wing aircraft, rotary-wing UAS can be flown close to the ground to collect high-resolution data efficiently. A major limitation that was reported was the limited time on station, typically under one hour. Consequently, for flights requiring longer on-station time, the operator must have an adequate supply of batteries or gasoline as needed.

A.2.5 Health & Safety Fund of North America (Dorsey, 2018)

The Laborers' Health & Safety Fund of North America (LHSFNA) published a report in 2018 that stresses the important role that UAS plays in project forecasting and construction monitoring (Dorsey, 2018). The agency believes that UAS technology offers a tool for rapidly gauging progress, particularly on construction sites that span large areas. UAS mounted with a diverse range of sensors (e.g., thermal, radar) can facilitate a quantum leap in surveillance capabilities, enabling the tracking of equipment, workers, and material, in addition to construction progress. The use of UAS in hazardous conditions also reduces risk exposures of workers.

The FAA has one set of regulations for drone operations for recreational use, while commercial use falls under its UAS rules. The regulations for commercial operations require the platform to be registered with the FAA, fly below 400 ft and within line of sight, fly mindful of privacy and airspace restrictions, and never fly near other aircraft or near airports (Dorsey, 2018).

The agency did not provide UAS platform details, but the article illustrated quadcopters and multirotor platforms. The agency cautions that potential hazards to workers from drones—like risk of injury due to a falling drone—could open employers to liability or privacy issues. Consequently, the agency advises employers to purchase adequate insurance. However, with those concerns out, the agency feels positive about the potential of this technology and lists the following applications:

- Construction progress monitoring
- Structural integrity assessment
- Preventive maintenance
- Construction site surveillance
- Search and rescue
- Time lapse recording of construction sites
- Frequent inspections permitted by increased time on station

A.2.6 Hartsfield-Jackson Atlanta International Airport (Michael Baker International, 2017)

In 2017, Hartsfield-Jackson Atlanta International Airport (ATL), a Class B airport, partnered with Michael Baker International and used a UAS to inspect Runway 9L/27R to develop a pavement condition assessment after obtaining approval from the FAA (Michael Baker International, 2017).

The team inspected the busiest and longest runway (12,390 ft) at ATL, which incurs the most pavement distress and damage due to the operations of heavy aircraft. A Topcon Falcon 8 UAS was used to collect high-resolution imagery of Runway 9L/27R. The aerial data were used to generate elevation contours, high-resolution orthomosaic imagery, a RGB 3D textured mesh, and a digital terrain model (DTM). Data were then analyzed using a suite of Autodesk, Esri, and Bentley software.

With the use of UAS, the inspection was completed in fewer than 20 minutes, and more than 630 high-resolution photos of the airfield were collected. The process took less than half the time to complete the inspections, as compared to the traditional, time-intensive, and cost-inefficient methods used today. The use of UAS provided the research team with a large amount of data that will help identify future areas for rehabilitation and improvement. (Michael Baker International, 2017)

A.2.7 Drone Deploy (Drone Deploy, 2018)

Bolton & Menk—an engineering, planning, and consulting firm—carried out a pavement analysis study to evaluate pavement deterioration for the City of Elko New Market, Minnesota (Drone Deploy, 2018).

The firm used DJI's Phantom 4 for pavement analysis in real time across 26 miles of roadway infrastructure. The team involved in this effort planned flights using the Linear Flight Plan application inside DroneDeploy to capture high-resolution aerial imagery through 18 separate missions over 2 days. Data were then processed using DroneDeploy's cloud-based platform.

The study showed that UAS can be effective in counteracting the need for ground-based surveys and can provide quick and convenient imagery-based data for city infrastructure planning. By reducing field times by more than 60% and testing high-accuracy imagery data, this novel implementation was a lucrative tool for city officials. (DroneDeploy, 2018)

A.3 UNIVERSITY/ACADEMIC LITERATURE REVIEW

A.3.1 Texas A&M (Henrickson et al., 2016)

In 2016, Texas A&M conducted a study to evaluate the use of UAS for infrastructure assessment (Henrickson et al., 2016). The team collected imagery of a variety of infrastructure elements, such as runway segments and roads (among others). The objective of the research was to assess the quality of imagery produced using specific sensors at a specific flight altitude and while maintaining a specific airspeed.

The selected tests included a variety of terrain types (e.g., paved runway, paved taxiway, grass field, trees), and the normalized difference vegetation index (NDVI) was used as spectral vegetation index. The three sensors used in the study were as follows:

- Sentek GEMS Multispectral and dual Complementary Metal-Oxide Semiconductor (CMOS) with visual and infrared imagery
- Canon EOS 5D Mark III DSLR along with CMOS for visual imagery and Marrex MX-G10 external Global Positioning System (GPS) antenna
- GoPro Hero3+ silver edition

The research team used two fixed-wing airframes (Anaconda and Super Club) to cover large areas, and two rotary-wing airframes (DJI S1000+ Octocopter and a Hexacopter) for areas that required detailed imagery. The collected geo-tagged images were later processed using Pix4D software with a 75% forward overlap and 60% side overlap.

The research team detected weeds growing through cracks on the runway pavement. In addition, they detected changes in surface uniformity on the runway from the texture maps they had developed. The study found that large areas could be assessed with a two-man crew and Sentek sensor along with the Anaconda. The team was successful in achieving the research objective at an altitude of 400 ft and airspeed of 35 mph at 2.34 in. (59 mm) GSD. (Henrickson et al., 2016)

A.3.2 Georgia Institute of Technology (Irizarry and Johnson, 2019)

The Georgia Institute of Technology (GIT) partnered with the Georgia Department of Transportation (GDOT) to conduct a study on *Field-Test-Based Guideline Development for Integrating UAS in GDOT Operations* (Irizarry and Johnson, 2019). GIT experimented with integrating UAS in applications such as airports, rail terminals, construction sites, and bridges to help provide Federal Aviation Administration (FAA)-adhered UAS guidelines. The purpose of the study was to determine technological feasibility, advantages, and limitations, and FAA guidelines compatibility; and to conduct a workshop for GDOT to understand the use of UAS technology and integrate it in GDOT division operations. GIT used several UAS platforms to

collect data via manual and automated modes. The reviewed literature focuses on GIT's tests at two different airports where runway inspections have been performed.

GIT conducted field tests at two airports: Habersham County Airport (AJR) and Roosevelt Memorial Airport (5A9). Both airports are located in the State of Georgia and were selected after site visits at four airports. The research team used six different UAS platforms to conduct runway inspections, construction inspections, and obstruction inspections, with Skysight as their industry partner. Four of the six platforms were used to conduct runway pavement inspections to identify and measure cracks. These four platforms were:

- DJI Phantom 4
- DJI Mavic Pro
- Yuneec Typhoon
- DJI Matrice 210

The four platforms collected still images, 3D model, and infrared images, and the 3D models were developed using photogrammetry. The team used Pix4D Mapper for data processing due to its high compatibility with DJI platforms and stored the data in a cloud environment.

The FAA requirements corresponded to GDOT standards for UAS use in the National Airspace System (NAS) and were suitable for the study of UAS operations. The study found that GDOT could use UAS for operations in their divisions with the help of technical training. The team identified that hiring an experienced contractor was beneficial to conduct UAS operations efficiently and relatively faster, particularly for airport inspections. GDOT recommended having a UAS-dedicated group that would help with the operations across various GDOT divisions. The study found that operating UAS was technologically feasible.

UAS proved to be time-efficient at gathering quantifiable information and enabled access to remote or otherwise inaccessible areas, in addition to increasing the safety of team members. However, data storage, insufficient training for data processing using photogrammetry, legal and privacy issues like liability insurance, and liability management were noted areas of concern.

Lastly, a workshop conducted for GDOT helped with education on UAS technology, FAA regulations, data collection planning, software, and processing. Further research with advanced use of data and newly developed sensors was recommended. (Irizarry and Johnson, 2019)

A.3.3 South Dakota University (Zhang, 2008)

In 2008, South Dakota State University conducted a study (Zhang, 2008)—sponsored by the U. S. Department of Transportation (USDOT)—to use remote sensing technology to assess the condition of unpaved road. The research was focused on developing image processing algorithms to detect and extract road defects from the UAS-collected imagery, including various road distresses from two-dimensional (2D) imagery, analysis of the inherent three-dimensional (3D) geometry information in images using photogrammetric techniques, and the fusion of 2D and 3D information to derive road condition parameters in an efficient and cost-effective way.

To assess the condition of unpaved road, an Airstar International Mongoose airframe helicopter used a pre-programmed flight path. The UAS's parameters (like position, velocity, and altitude) were recorded using GPS and geomagnetic sensor.

Preliminary results of the 2D road imagery analysis showed that UAS images were suitable for extracting many distresses needed for monitoring the condition of unpaved roads. For the imagery acquired right after sunrise, potholes, rutting, loss of aggregate cover, drainage issues, and poor overall cross section were identifiable despite the large shadows of roadside trees. The study concluded that 2D imagery is limited in distress identification and does not provide enough information on vertical dimensions of a surface distress. Hence, the study suggested 3D models for enhanced detection of distresses such as potholes and rutting. (Zhang, 2008)

A.3.4 University of New Vermont

The University of New Vermont conducted a study on integration of UAS to increase safety and decrease costs of transportation projects and related tasks for the New Hampshire Department of Transportation (NHDOT) (O'Neil-Dunne and Estabrook, 2019). The University of New Vermont established eight case studies to analyze UAS implementation in the transportation infrastructure. One of the case studies involved airport runway and airspace inspection. The team worked with Jaffrey Airport (AFN), NHDOT, and the FAA to collect the data using UAS.

Table A-6 summarizes the eight case sites, platforms used for testing, and deliverables.

Table A-6. University of New Vermont Test Sites and Platforms

Test Study and Site	Platforms	Deliverables
Simulated Car Accident, New Hampshire Motor Speedway, Loudon, NH	senseFly eBee RTK, DJI Phantom 4	Orthomosaic imagery, 3D point cloud
Airport Runway and Airspace Inspection, AFN	senseFly eBee Plus	Orthomosaic imagery, digital surface model, digital elevation model, and 3D point cloud
Bridge Inspection, Lebanon, NH	senseFly Albris, DJI Phantom 4	High-resolution inspection photos, aerial photos, aerial videos
Construction Monitoring, Derry and Windham, NH	senseFly eBee Plus	Orthomosaic imagery, digital surface model, digital elevation model, and 3D point cloud
Emergency Management, Murphy Dam on Connecticut River, Pittsburg, NH	senseFly Albris, senseFly eBee Plus	Orthomosaic imagery, digital surface model, digital elevation model, 3D point cloud, and high-resolution inspection photos
Traffic Monitoring, I-95 (1430-1630), Portsmouth, NH; Franconia State Park Parking Area (1030-1430)	DJI Phantom 4	10 video files, 8 video files and 38 photos

Test Study and Site	Platforms	Deliverables
Rail and Bridge Inspection, NH Central Railroad, Lancaster, NH: (2-mile stretch) and bridge in the railroad corridor	senseFly Albris, senseFly eBee Plus	Orthomosaic imagery, digital surface model, digital elevation model, 3D point cloud, and high-resolution inspection photos

RTK = Real-time kinematic

For AFN's runway and airspace inspection, a fixed-wing small UAS platform, eBee Plus, was used to capture 1,068 photos over an area of 210 acres, taking 53 minutes and two flights. An additional 1,058 pictures were captured on another day (for northern and southern runway approaches) across five flights in 115 minutes. The team used eMotion software after the flight to tally the collected images and Pix4D Mapper to generate 2D and 3D orthomosaic imagery; and a digital surface model, digital elevation model, and 3D point cloud for the total of 2,126 pictures.

The study suggested that using UAS was safe, time-efficient, and feasible for runway pavement inspections in comparison to foot-on-ground (FOG) inspections. The study found that the UAS technology was efficient in identifying fine cracks with a resolution of 1.8 cm (18 mm) compared to Esri base map of 30 cm (300 mm).

Furthermore, the study found that UAS was helpful in areas that were traditionally inaccessible or unsafe for inspection personnel, and that the data extracted provided a spectrum of analysis and geospatial integration possibilities. According to the researchers, senseFly eBee Plus was comparatively a more complex platform than DJI Phantom 4, as it requires more technical GIS knowledge for operations. To implement the use of UAS within NHDOT, the evaluation determined quadcopters along with cameras and gimbals as the most viable solutions due to their minimum training requirements and capability to acquire aerial imagery. In addition to emphasizing the need for liability and insurance for UAS operators, the researchers looked into the privacy laws of New Hampshire and suggested private landowner approval prior to UAS operations. (O'Neil-Dunne and Estabrook, 2019)

A.3.5 Massachusetts Institute of Technology (Petkova, 2016)

This thesis study focused on deploying drones for autonomous detection of pavement distress (Petkova, 2016). The motivation for the research is to push the state of the art and improve how pavement assessments are performed. During FOG inspections that are time-consuming and labor-intensive, assumptions are made about the condition of a large percentage of the pavement. With the right tools, these tasks can be automated to enhance coverage and reduce inspectors' exposure to risk.

This research employs a UAS to perform video-based remote sensing in conjunction with employing an automated feature extraction algorithm to identify and locate distresses. The mission-control software uses Python to determine vehicle operating parameters and issue navigation directions to complete the mission. Control commands are communicated to the platform using Micro Air Vehicle Link (MAVLink) protocol. The algorithm can be tweaked to carry out a simplistic function like pothole finding or to perform a comprehensive function such

as looking for pavement distresses (cracks) in addition to the simplistic pothole search. The system stores an image of the identified distress with the GPS coordinates and a timestamp of when it was found.

The research used 3DR's Solo UAS with a GoPro Hero4 Black Camera. The UAS is composed of a dual processor with a clock speed of 1 GHz and with 512 MB of random-access memory (RAM), which can fly at maximum speeds of 55 mph. The GoPro camera was installed using a gimbal with three-axis stabilization. This setup facilitates the camera's angular motion between 0 and 90 degrees, with the latter for downward recording. The video frame capture capability was 24 fps at 1080p video resolution. Python software using application programming interfaces (APIs) developed by 3DR for communication, control, software updates, and UAS application development was used. Autonomous flight missions were generated using Google Maps™ in conjunction with a custom application that extracted path coordinates from the keyhole markup language (kml) file. With the issuance of 14 C.F.R. Part 107 (Small Unmanned Aircraft Systems) in May 2016 allowing students to operate and test sUAS for research, the system was flown in Massachusetts near Cambridge and Somerville.

The system suffered from limitations of the hardware used. The processor onboard the 3DR solo was found to be incapable of performing real-time analysis. A configuration of a processor with a rated speed of 1.8GHz and at least 4GB of RAM could perform real-time analysis in 1 second compared to approximately 10 seconds for the 3DR Solo's hardware. Flight times available due to battery constraints were limited to 20 minutes with a payload sensor. The research also suffered from connectivity issues with the UAS, leading to recurrent video interruptions. The UAS had issues in connecting to the required number of satellites (9) to achieve a horizontal positioning accuracy of 5 m or less. The resulting accuracies were in the 5 to 10 m range.

With a powerful processor, which will become available in time, this system shows potential for real-time monitoring and pavement management. (Petkova, 2016)

A.3.6 European Transport Research Review: Review of Remote Sensing Methodologies for Pavement Management and Assessment (Schnebele et al., 2015)

This literature review and survey of current pavement evaluation and management techniques sought to evaluate the role of remote sensing technologies in reducing the expense, labor intensity, and time required to make assessments. In this paper, Schnebele et al. (2015) define "remote sensing" as a technique for surveying transportation infrastructure without actual contact with its surface. Remote sensing offers the potential to perform infrastructure condition assessment, with the notable benefit of increased spatial coverage. This stands in stark contrast with traditional evaluation methods that use FOG inspections limited to point observations. Such methods also suffer from the subjectivity of human inspectors, who may report different distresses and cause variability in data and, therefore, in understanding pavement condition. The integration of geospatial tools and techniques is making it possible to perform comprehensive, frequent, and safe monitoring and assessment of transportation infrastructure. Remote sensing tools provide an especially useful means to perform infrastructure assessment in the aftermath of major disasters. The paper reports that although $182 billion was spent on maintaining and improving the more than 6,000,000-km U.S. road network, the American Society of Civil

Engineers (ASCE) gave it a grade of D. With the extensive spatial spread of this large network, remote sensing presents an opportunity for assessment and improvement. The platforms evaluated in the research include vehicles, airplanes, satellites, and UAS.

This paper serves to provide a comprehensive repository of conventional and remote sensing tools for roadway evaluation for pavement managers. It includes a detailed review of available literature and promising techniques. The available literature tracks the introduction and growth in usage of remote sensing techniques by states. Schnebele et al. (2015) cites the National Cooperative Highway Research Program (NCHRP) Synthesis 203 (1994), which found that each of the 40 states sampled were using manual methods . Ten years later, of 45 agencies sampled, 28 were using automated data collection including video monitoring while 17 were still using manual data collection. By 2007, State DOTs like the Virginia Department of Transportation had developed data quality standards. A limitation to widespread adoption of these tools was the lack of systems that provided the required functionality. However, based on the rapid adoptions by states, the widespread use of remote sensing technologies is inevitable.

The authors reviewed the following remote sensing techniques through available literature:

Image Processing (Visible) is the actual method for automated detection using image processing and pattern recognition to identify surface distresses. These involve isolating the distresses and creating a binary image that is then used with segmentation algorithms for distress identification. From their literature review, the authors observed that the primary segmentation algorithms used were edge detection and thresholding. Prior research was able to identify cracks, and through texture analysis and segmentation, was also able to identify potholes. Through the use of wavelet transforms, segmentation algorithm, and thresholding, researchers were able to detect and classify longitudinal cracks, transverse cracks, alligator cracking, and block cracking in flexible pavement. The authors found that available literature documented the difficulties of crack detection using image processing. This is attributed to the typically small spatial coverage of cracks and texture and lighting that can hide distresses. The authors observe that photogrammetry is a lower-cost option that offers 3D information that can be used for pavement assessment.

Ground-Penetrating Radar utilizes electromagnetic waves and can detect changes in materials and moisture contents. GPR finds use in the measurement of pavement layer thickness (which helps avoid surface closures for destructive assessment) and identification of voids. While GPR can predict asphalt pavement thickness, it does not have similar success with PCC pavements. The composition of PCC layers results in attenuation of radar waves, and the similarity in the die-electric constants of the surface and base layers makes identification of the layers difficult. Detecting voids filled with water and air provides a way to understand pavement deterioration. Moisture between asphalt and the base causes distresses such as cracking, rutting, potholes, and raveling. Researchers have found GPR capable of detecting moisture in the subgrade of asphalt pavements and identifying cracks in asphalt layers and measuring their depths.

Infrared Thermography (IRT) overcomes the drawbacks of GPR technology, which can measure depth and thickness of surface distresses in asphalt pavements but cannot provide horizontal measurements. IRT measures the amount of radiation emitted by objects in the

infrared spectrum. The emissivity of an object is a function of its composition and temperature. As asphalt ages, its emissivity changes due to wearing away of the binder. Researchers have been able to identify distresses and areas of delamination in airport pavements by picking up temperature differences as low as 0.5 °C. However, IRT is affected by climatic conditions such as rainfall, wind, and sunlight.

LiDAR and Terrestrial Laser Scanning (TLS) both work by transmitting and recording the reflection of electromagnetic radiation in the near-infrared region. The measurement results in point clouds with precise x, y, and z position data. With its dense point clouds, LiDAR finds use in mapping and creating Digital Elevation Models (DEMs). LiDAR produces similar results during day or night, unlike other competing techniques. LiDAR can detect pavement distresses and help estimate repair quantities. TLS can provide continuous 3D pavement surveys and has been used to detect pavement distresses like rutting, shoving and potholes, cracks larger than 2 mm in asphalt pavements, and faulting of concrete panels. The data collection proceeds at highway speeds and is, therefore, safer than manual techniques. However, the high cost of TLS instrumentation and hardware are barriers for its widespread implementation. The results are consistent with standard techniques.

Hyperspectral Imagery collects spectral information that provides insight into the chemical and mineral makeup of objects. As asphalt ages and its binder wears out, its reflectance increases in the near-infrared and short-wavelength infrared (SWIR) spectrum by as much as 10% compared to new pavement. However, cracking exposes potentially unweathered material, which makes the discrimination of old and new materials complex.

The use of remote sensing techniques offers new potential for pavement managers to assess large areas, often in a short time. The authors acknowledge that, although remote sensing techniques cannot replace traditional geotechnical methods, they do provide an opportunity to reduce the number or size of areas requiring site visits or manual methods (Schnebele et al., 2015).

A.3.7 Kungliga Tekniska Högskolan Royal Institute of Technology (Millian, Julian D.R., 2019)

This study, conducted by the Kungliga Tekniska Högskolan Royal Institute of Technology (KTH), emphasizes the need for managing pavement assets because of the large spatial extent and significant cost of maintaining pavements (Millian, Julian D.R., 2019). Managing pavements requires periodic condition assessments by inspectors walking the pavements or by use of mobile vans equipped with a wide range of sensors. Using traditional methods to inspect large networks is both cost-prohibitive and labor-intensive. This study was developed jointly by KTH and Stockholm Hamn AB for managing the new deep-sea Norvik port in Sweden, which commenced operations in May 2020 as expected. The port will handle 500,000 containers and 200,000 rolling goods vehicles annually, and maintaining its pavements is a critical factor to its efficient operation. A literature review (Zakeri et al., 2016) performed by the authors found that UAS imagery outperforms that obtained through satellites and mobile vans on account of its lower cost, rapid deployment, and high safety. Other studies (Henrickson, et al., 2016) found that using UAS helped to reduce the cost and time for inspection of pavement assets. A further study (Zhang, 2008) observed that UAS imagery provided adequate detail for the extraction of pavement condition attributes.

The objective of the study was to explore the state of the art in the use of UAS for infrastructure inspection and management, evaluate operating conditions and platforms, lay out processing details, and identify additional application of the collected data (Millian, Julian D.R., 2019). In Figure A-1, Coenen and Golroo (2017) give a broad outline of the pavement management system implementation used in practice.
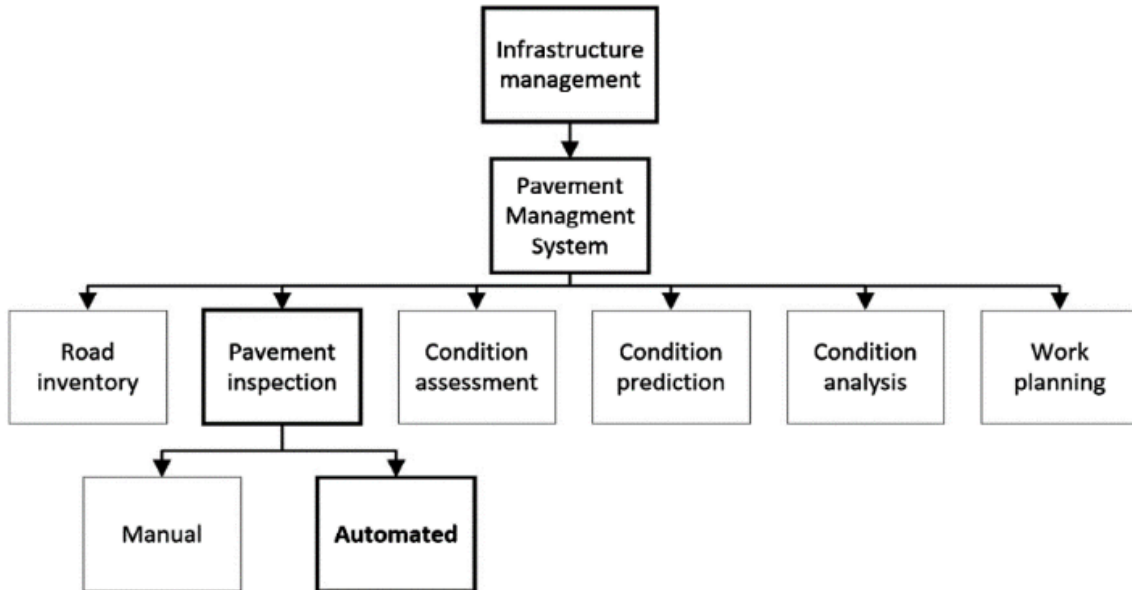
Figure A-1. Pavement Management Systems (Coenen & Golroo, 2017)

Despite the technological innovations available today, a large amount of data collection is still performed by skilled inspectors using the standard procedure in ASTM D6433. However, manual inspections face the problem of intra-inspector variability (due to subjectivity), concerns about the safety of inspectors from traffic and exposure to pollution, and high costs (including labor and time).

One improvement on manual inspections is the van-based inspection procedure, which uses sensor suites mounted inside and outside the vehicle. The sensors include cameras for capturing imagery, GPS, TLS, and illumination devices. One drawback of vehicle-based pavement inspection systems is their inability to cover the entire pavement width in one pass. Consequently, procedures to overcome this have evolved, i.e., data collection in the outermost traffic lane, which is typically loaded with the heaviest traffic. Additionally, for roadways with fewer than four lanes, data are collected in just one direction. One disadvantage of collecting data from only the heaviest loaded lane is that conditions in the other lanes can be missed, and impacts of difference pavement structures might not be captured.

Table A-7 provides a list of the various sensors and their applicability to detect the various distresses and is a very useful tool for the selection of the most appropriate sensors for specific pavement distress assessments.

Table A-7. Review of Sensors and their Applicability to Different Distress Types (Coenen & Golroo, 2017)

Distress Type	Camera	Accelero-meter	3D-Sensor	Microphone	Sonar	Pressure	Friction	Deflecto-meter
Cracking	C/P		C/P					
Patching	C/P		C					
Potholes	C/P	C/P	C/P	P	P	C/P		
Rutting	P		C/P		C			
Shoving	C	P	C/P			P		
Bleeding	P		C/P					
Polished aggregate			P	C/P				
Raveling			C/P	C				
Edge drop-off			C		C			
Water bleeding and pumping			C	C				
Additional road information								
IRI	C	C/P	C/P	C/P		C/P	C	
Skid resistance			C				C	
Substructure			C/P					C
Other	C	C	C/P	P	C			C

Note: C = Commercial Development, P = Scientific Research Papers

The use of satellite photography could overcome some of the drawbacks of vehicle-based inspection. However, it is observed that satellite imagery was not able to detect distresses like rutting and cracking. The authors state that, based on available literature, UAS sensors can cover areas measuring several kilometers and can identify details, such as pavement distresses, 1 cm in size or less. Consequently, UAS can be used for

- Traffic surveillance
- Structural inspection
- Construction inspection, progress monitoring, and safety
- Roadway condition inventory collection
- Survey

The limitations of UAS listed in the research include:

- Regulatory regime—operations close to airports and military installations are restricted.
- Impact of winds on flight trajectory
- Flight altitude control issues

- Low endurance due to battery limits
- Rapid battery drains in temperatures below 15 °C

The researchers evaluated three types of sensors and observed the following:

- Cameras: Digital photographs from inexpensive cameras (costing under $100) could provide the resolution for the level of detail required to detect pavement distresses. They found that Coenen & Golroo (2017) used a Sony Cybershot DSC-W180 camera to collect aerial imagery with satisfactory results. The authors do not provide the details of extent of overlap but state that results from photogrammetric reconstruction for common distress types like rutting (outer wheel path), alligator cracking, and transverse cracking were satisfactory.

- LiDAR: Recently, technological innovations have made it possible for LiDAR sensors to be carried by UAS. The authors observe that aerial LiDAR is cheaper than mobile LiDAR and can collect data in 60% of the time for 60% of the cost of mobile LiDAR, as reported by the Dye Management Group (2014). Although the benefits are there, point cloud densities for aerial LiDAR are lower than terrestrial LiDAR. Data quality was found to be dependent on parameters such as sensor capability, flight elevation, speed, and point density. The technology has potential and is used in conjunction with imagery collection.

- Multi- and Hyperspectral Imagery: These sensors work similarly to cameras but capture imagery outside the visible spectrum. Due to the spectral bands used, these sensors are able to provide details of the chemical and mineral properties of an object. The technique is based on the reflectivity of objects, which varies with chemical composition. In the case of asphalt pavements, as the binder material degrades with age, its reflectivity also changes. This is used to detect distressed asphalt pavement. However, pavement contamination with external materials (oil, water, patches) makes the analysis complicated.

The authors concluded from the literature review that resolution is the main challenge in automating pavement distress assessment. Resolution depends as much on the sensor's capability as on the altitude or distance from which the picture is taken. Therefore, it is observed that pixel size is inversely proportional to altitude, though the spatial coverage increases with altitude.

Processing data collected in the field is required to transform it into pavement condition data that can be input in typical pavement analysis software (PAVER or PAVEAIR) for PCI computation. The processing proceeds using traditional methods such as intensity thresholding and edge detection. However, this process can result in several false positives on account of shadows, particle texture, water ponding, or brightness. Deep Learning (DL) is helping to solve the feature extraction problem. The technique involves training the DL network with a learning set. The DL network uses this set to encode the image properties with the help of different analysis layers.

Three DL network algorithms that can be used for feature extraction are:

- Caffe, developed by the University of California at Berkeley
- TensorFlow, developed by the Google Brain Team
- Keras, a Python DL library and API that can run with TensorFlow.

The study also discusses the efficacy of various data processing for feature extraction. Figure A-2 shows the process of the deep learning crack detection mechanism.
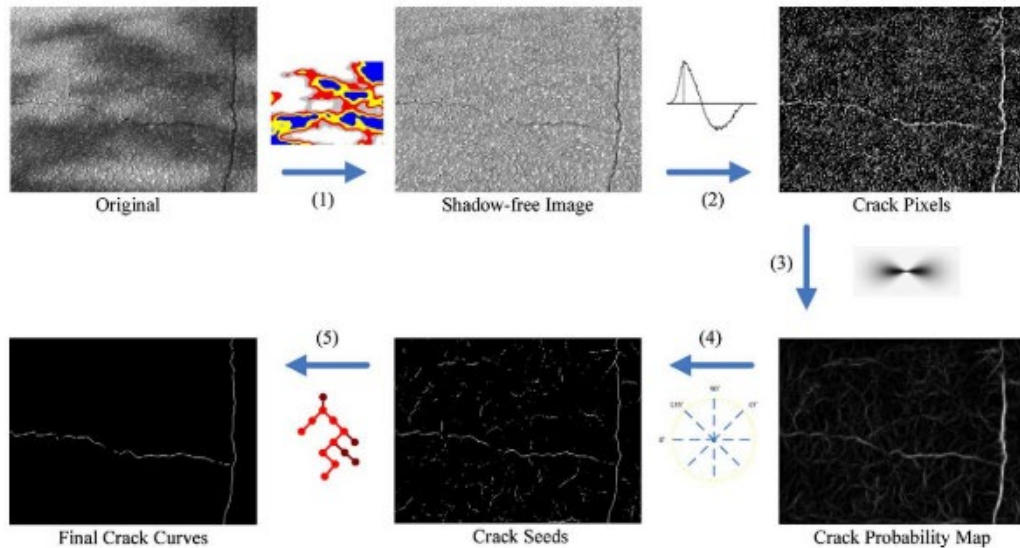
Figure A-2. CrackTree Proposed Flow Chart (Zou et al., 2012)

a.   **Machine Learning and DL Algorithms with Imagery Data.** Research by Zou et al. (2012) used convolutional neural networks (CNNs) for the feature extraction. The study used a geodesic shadow-removal algorithm and produced satisfactory results. However, they found discontinuities in the extracted features and were not able to determine crack widths, which are used to classify the severity of the distress. A later improvement on this study (Zhang et al., 2018) made computation more efficient without loss of data. Though the results were much improved, the algorithm still had issues with fine cracks and joints.

b.   **Multispectral Imagery.** The study by Pan et al. (2018) used multiple learning algorithms in addition to CNN and claimed 98.3% effectiveness in identifying cracks and potholes. The study also evaluated the influence of pixel resolution in the automatic distress identification procedure by flying UAS at different elevations and collecting imagery with different pixel resolutions. Researchers found that a number of missed distresses (cracks) greatly increased beyond a pixel size greater than 3 cm. It was determined that the pixel resolution should be selected based on expected crack widths.

c.   **Hyperspectral Imagery.** The application of this type of data has not been researched extensively.

d.   **LiDAR Data:** Guan et al. (2015) proposed a methodology using LiDAR point clouds termed ITVCrack (Iterative Tensor Voting). The pavement surface points are extracted and converted to imagery. This is then used with an edge extraction algorithm for the

feature extraction. The researchers claimed that the method outperformed other alternatives.

The research presented in Millian (2019) was part of a master's thesis. The data collection was performed on a test section using a UAS with a diverse set of parameters. The UAS and the pavement test section were provided by Stockholm Hamm AB. Data collected by the UAS was compared with traditional data collection methods including FOG and vehicle-based. The data collected will be processed using the techniques described earlier.

Sensor selection was carried out to ensure the required precision, endurance, platform stability, and cost. LiDAR sensors were of interest to the research due to their ability to acquire 3D data. Cameras can acquire 2D and 3D data, though 3D data capture requires a considerable amount of time and computational power. The selection of the right camera that is suited for photogrammetry is desired for high accuracy. Such cameras are pricey, however, with high-end ones designed for UAS—like the Phase One IXU 1000 sensor with 100 Mega Pixels resolution—costing as much as $70,000. The most important parameter to bear in mind while selecting the right camera sensor is pixel size, as discussed earlier. Pixel size is affected by other variables like lens resolution, aperture, and focal length. Additional important factors include overlap and ground control point. Tables A-8, A-9, and A-10 present these comparisons.

Table A-8. Comparison of UAS Camera Sensors

Camera	Megapixels	Sensor Size (mm)	Compatibility	Ground Sampling Distance at 120m cm/pixel	Shutter
Phantom 4	12.0	6.27x4.55	Phantom 4	5.2	Rolling
Phantom 4 Pro	20.1	12.8x9.6	Phantom 4	3.2	Mechanical
DJI Zenmuse X3	12.0	6.27x4.55	Inspire 1/M100/M600	5.2	Rolling
Canon 5Ds	50.6	36x24	M600/ALTA 8/Altura Zenith	With 35mm lens– 0.9471	Mechanical
Canon 5D Mark 3	22	36x24	M600/ALTA 8/Altura Zenith	With 35mm lens– 1.3714	Mechanical
DJI Zenmuse X5	16.0	17.3x13	Inspire 1/M100/M600	With 15mm lens–3	Rolling
DJI Zenmuse X5S	20.1	17.3x13	Inspire 2	With 15mm lens - 2.7	Rolling
DJI Zenmuse X4S	20.1	12.8x9.6	Inspire 2	3.3	Mechanical
DJI Zenmuse Z30	2.1	4.95x3.42	M100/M600	3.4–0.3	Rolling
DJI Zenmuse Z3	12.0	6.32x3.55	Inspire 1/ M100/M600	4.8–1.4	Rolling
Sony RX100 VI	20.13	13.2x8.8	M600	3.3–2.15	Mechanical

Table A-9. Comparison of UAS Flight Mission Software Based on the Developer's Information (Millian, Julian D.R., 2019)

Software	Operative System	Sensor	Flight Personalization Parameters										Compatibility
			OL	A	HT	PR	S	Alt	CR	AU	MFP	BDI	
DJI GS Pro	iOS	Camera	✓	✓	✓	✓	✓	✓			2	KMZ, SHP	DJI drones
Map Pilot for DJI	iOS	Camera	✓	✓	✓	✓	✓	✓			1		DJI drones
Pix4D capture	iOS/ Android	Camera	✓	✓	✓	✓	✓	✓	✓	✓	4		DJI, Parrot, Yuneec
UgCS	Windows/ macOS/ Linux	Camera/ LiDAR	✓	✓	✓	✓	✓	✓		✓		KML, DEM	DJI, Parrot, Yuneec, Others

Note: OL = overlap, A = angle, HT = Height, PR = Pixel Resolution, S = Speed, Alt = Altitude, CR = Check Results, AU = Auto Upload, MFP = Mission Flight Patterns, BDI = Base Data Import

Table A-10. Main Photogrammetry Software Comparison Based on the Developer's Information (Millian, Julian D.R., 2019)

Software	Proc-essing	VE	MC	AP CG	DTM-DEM	PCE	GR	V/D	RTK/ PPK	C	PLP	Output Formats
PIX4D	PC/ cloud	✓	✓	✓	✓	✓	✓	✓	✓	✓	3,990 EUR	las, shp, dxf, dgn, pdf, csv, klm, Geotiff
Agisoft Metashape	PC/ cloud	✓	✓	✓	✓	✓	✓	✓	✓	✓	3,499 USD	Geotiff, las, pdf, dxf, kmz
Reality Capture	Cloud	✓	✓	✓	✓	✓	✓	✓	✓		1,500 EUR	las, shp, dxf, dgn, pdf, csv, klm, Geotiff
Autodesk ReCAP	Cloud			✓	✓	✓	✓				310 USD/ yr	las, shp, dxf, dgn, pdf, csv, klm, Geotiff
Trimble Inpho	PC		✓	✓	✓	✓	✓	✓	✓	✓		las, shp, dxf, dgn, pdf, csv, klm, Geotiff

Note: VE = Video Extraction, MC = Multi-Camera, APCG = Automatic Point Cloud Generation, DTM-DEM = Automatic DTM-DEM Generation, PCE = Point Cloud Editing, GR = Georeferencing, V/D = Volume/Distance Measurements, RTK/PPK = RTK/PPK Support, C = Contour and Map Editing, PLP = Perpetual License Price

Using the details outlined in the preceding tables as a guide, the research team selected the DJI Inspire 2 UAS with Zenmuse X5S camera. The UAS has an endurance of 27 minutes, fast image processing, and obstacle avoidance capability. The Zenmuse X5S camera sensor has a 20.8-megapixel image capability, and a 17.3-mm focal length. The camera provides a pixel size of approximately 3 cm at a flight altitude of 120 m. The software used for mission planning was Map Pilot for DJI. The flight plan was manipulated to acquire pixel sizes ranging from 0.5 to 2

cm with a 70% overlap. With these inputs, the flight planning software made automatic adjustments to flight altitude and speed for the most appropriate data collection.

The first go-around had problems in data collection for pixel sizes other than 1 cm, and had to be repeated. The last one could not be completed by the time this report was prepared.

Post-processing steps included building the DEM and the orthophoto mosaic creation using Agisoft Metashape software. To get the distress data, elevation maps generated via AutoCAD Civil3D were used. These maps are useful in detecting settlement in pavements but not for lateral movements. Commercially available software like WiseCrax or CrackIT have the ability to automatically detect cracks from data collected by pavement survey vans. An alternative to these software programs is applying several filters to the orthophoto mosaics with Adobe® Photoshop®, as described by the following steps:

- Image was duplicated in a new layer.
- Colors were removed for the image.
- A 100% color dodge filter was applied.
- Colors were inverted in the image.
- Contrast was increased to 100%.
- RGB color levels were set to 0.25.

Next, the following steps were performed:

- Data of interest was extracted.
- Distress data in models was used.
- Decision support was attained for the most appropriate maintenance action.

The sensor selection oftentimes represents trade-offs of precision vs cost or other factors. The sensor selected for the current research was a quadcopter branded as a professional filming model, the DJI Inspire 2. Other models like the DJI Matrice 200 (a hexacopter), are branded for industrial use. The Matrice 200 offers greater flight time, more damage reliability (due to the six propellers), and higher compatibility with third-party accessories and sensors. On the other hand, the DJI inspire is a more agile model, with a major number of flight modes, some cinematic camera options, and augmented image processing and storage.

Fluctuations were observed in the picture mosaics obtained from the test flights in the Norvik port. One way to reduce the impact of wind on data collection is the use of hexacopters or octocopters, which are more stable, can better withstand wind forces, and can carry larger payloads with advanced navigation systems.

The UAS used in the current research, like typical models, was equipped with standard GPS. Such positioning systems do not provide accurate flight attitude control. Depending on the type of usage, it may be necessary to increase the number of control points or to employ alternative technologies like RTK or post-processing kinematic (PPK) localization. The current study was focused on the resolution of data and not on the relative elevation of one point compared with another and not the real x, y, z coordinates of a given point. However, this becomes important for

other projects, and, therefore, it is necessary to ensure data quality by using control points or alternative technologies to improve the accuracy given by the GPS equipped in the UAS.

It was felt that, with real-time access, data quality would be better and the requirement for repetitive flights could have been reduced. Using software that allowed real-time access to the data (like PIX4D) could have helped to reduce the necessity of repeat flights.

The imagery gathered at a resolution of 0.5 cm/pixel clearly captured the separation among blocks even for the normal scenario. At lower resolutions (1 cm/pixel or 2 cm/pixel) these separations were not so easily noticeable with the human eye. However, with the use of machine learning (ML) or DL algorithms, even images at 2 cm/pixel resolution can be used for distress extraction. It is therefore extremely important to define sensor resolutions adequately. The current research was unable to detect cracked pavement blocks because the pavement was newly constructed. For simpler tasks like construction progress monitoring and even volume calculations, resolutions of 1 to 2 cm/pixel are acceptable.

The current research was not able to use LiDAR sensors.

A.4 SMALL UNMANNED AIRCRAFT SYSTEM-DERIVED DATA PROCESSING METHODOLOGIES

The research team assessed available software and algorithms that can process the collected data for analysis. Image processing (IP) and AI tools have improved the overall performance of Pavement Management Programs (PMPs) by helping analyze big data originating from distress surveys. Pavement data analysis mainly focuses on three aspects: quantification of distresses, evaluation of the current condition, and prediction of future performance of pavements. Developments in the fields of IP and ML have substantially reduced processing time and costs associated with distress detection and quantification procedures. AI and DL are the current cutting-edge, breakthrough technologies of recent times that have been successfully used in several domains to improve the efficiency of computation. (Peraka & Biligiri, 2020)

A.4.1 Distress Detection and Quantification

The data collected from the field using automated data collection methods (digital survey vehicle [DSV] and sUAS) have to be processed to determine the condition of the pavement. Advancement in the field of computer science has enhanced the data analysis rate. Currently, IP and ML tools are being utilized for measuring severity and extent of various distresses (Coenen & Golroo, 2017).

A.4.1.1 Cracking

Major developments in the field of surface defect detection are being made towards identification and analysis of crack propagation. In imaging language, a crack can be defined as a structure composed of a linear, curve, or composite pattern. The intensity of crack is typically different from the surrounding environment. To map crack pixels of similar intensities and identify the crack patterns, several algorithms have been developed that include a combination of

pre-processing, segmentation, feature extraction, feature selection, and detection and classification. (Zakeri et al., 2016)

1. **Preprocessing:** The data collection process is significantly affected by regional climate. Even with the use of highly sophisticated equipment, the captured images will have some contrast, noise, and blurred spots. These significantly affect the edges and cause sharp peaks in image pixel intensities, which actually represent cracks in the system. In preprocessing, a set of operations are performed to restore the images by removing noise.
2. **Segmentation:** The process of extracting the region of image that is of interest. For example, the captured image might have airport markings, cracks, and potholes. The region of interest in that case would be cracks and potholes. The image would be segmented for the region so that the extent and severity can be measured.
3. **Feature extraction and selection:** This is used to find similar featured members or links in the images so they can easily be detected and classified. There is a chance that a rut area will have been affected with hairline cracks. In segmentation, the region will be selected, and in feature extraction, the noise (such as the presence of shadow regions) will be eliminated, while at the same time, the areas of rut and cracks are extracted. In feature selection, similar features will be selected, such as cracks with similar widths. Then, the detected features that have similar characteristics are classified as medium, low, or high severity.
4. **Detection and classification:** Significant research has been performed in the field of crack detection, classification, and quantification using IP and ML. Deficient real-time data processing, low quality of images, and high processing time have been found to be the major limitations in crack detection and classification.

Oliveira & Correia (2014) observed that traditional IP algorithms take a significant amount of processing time and nominal accuracy in quantification when too many distresses are present in images. Also, they occupy substantially high memory to process data and to store the processed data, thus resulting in relatively high computation costs. Therefore, ML tools, such as neural networks (NN), which mimic the behavior of (efficient) neurons in the nervous system, have been introduced to detect cracks (Oliveira & Correia, 2014).

A.4.1.2 Potholes

Data related to potholes can be obtained using imaging, sensing, and vibration applications. The near-circular shape of potholes makes it an easy process for detection using IP algorithms. Several research studies have focused on detecting potholes in a cost-effective way and have helped agencies take immediate action for their repair. Jo and Ryu (2015) conducted a study and formulated a pothole detection algorithm using a black-box camera to capture the pavement images. In the setup, the images were processed using gray scaling, histogram thresholding, and image enhancement techniques. The processed images were analyzed using a pothole detection algorithm. Loading the trained algorithm onto the black-box camera allowed potholes to be automatically detected in the image (Jo & Ryu, 2015).

A.4.1.3 Rutting

The major advancements in detecting and quantifying rutting were initiated with the inclusion of 3D imaging techniques in the pavement data collection process. Currently, research has mostly focused on 3D surface generation and detection of rutting from the 3D surfaces. Since the 3D imaging techniques are expensive, more research is required to reduce the cost of data collection and focus towards creating 3D surfaces from 2D images. (Peraka & Biligiri, 2020)

A.4.1.4 Other Distresses

Overall, current state-of-the-art technology is not geared to detect other distresses. One study conducted in 2015 (Mathavan et al., 2015) reviewed 3D technologies in the fields of pavement imaging. The study concluded that the imaging conditions, in terms of lighting, etc., are very random. For instance, measuring the volume of the pothole requires a large field of view with a reasonable spatial resolution, whereas microtexture evaluation requires very accurate imaging. Within the two extremes, there is a range of situations that require 3D imaging. The study concluded that it is possible to collect the details of all distresses—such as cracking, potholes, rutting, macro- and micro- texture, shoving, raveling, joint faulting, and spalling—if the focus depth and time-of-flight principles are efficient enough. (Mathavan et al., 2015)

A.4.2 Challenges in Incorporating Deep Learning to Distress Detection and PMPs

Careful handling of the large amount of data collected using automated systems is a critical task in terms of decision-making with respect to maintenance interventions. AI and ML techniques are effective in dealing with big data, making incorporation of soft computing techniques such as IP, AI, and ML inevitable in PMPs in the future.

There are some significant challenges in application of soft computing techniques in PMPs. For instance, selection of appropriate soft computing methods in data analysis is challenging, as it affects the performance of the entire system. In addition, assessing the reliability of the models developed using soft computing techniques is quite intricate. In training the algorithms, it is essential that the results are verified with the standard methods before implementation of the product.

Currently, there is a gap between research findings and state of practice. To verify the practicality and reliability for incorporation of ML techniques in pavement distress evaluations, soft computational technologies have to be assessed at a much larger scale. This would transform PMPs from a data-driven approach to technology-driven approach, which is a step towards achieving sustainability goals in transportation. (Peraka & Biligiri, 2020)

A.4.3 Data Processing Software

The research team evaluated the following post-processing software related to this research effort:

- Pix4D
- Bentley ContextCapture
- ESRI ArcGIS
- AutoDesk Recap, AutoCAD
- Laser crack measurement system software, if available for sUAS
- Others, as needed

A.5 SMALL UNMANNED AIRCRAFT SYSTEM-DERIVED DATA OUTPUT AND ANALYSIS

Primary deliverables from this research effort included georeferenced still photos, infrared imagery, and point cloud data of airport pavement infrastructure. These sUAS deliverables were analyzed by the research team to determine their validity for use in PMPs and for use in FAA PAVEAIR.

The research team measured accuracy by verifying sUAS data and comparing it to the following control data sources:

- Surveyed Geodetic Control
- DSV data and Mobile LiDAR
- FOG survey data

A.6 REFERENCES

Booz Allen Hamilton. (2020a). *Airports and unmanned aircraft systems, Volume 2: Incorporating UAS into airport infrastructure—Planning guidebook*. Transportation Research Board. https://doi.org/10.17226/25606

Booz Allen Hamilton. (2020b). *Airports and unmanned aircraft systems, Volume 3: Potential use of UAS by airport operators*. Transportation Research Board. https://doi.org/10.17226/25607

Brooks, C., Dobson, R., Banach, D., Oommen, T., Zhang, K., Mukherjee, A., Havens, T. C., Ahlborn, T., Escobar-Wolf, R., Bhat, C., Zhao, S., Lyu, Q., & Marion, N. (2018). *Implementation of Unmanned aerial vehicles (UAVs) for assessment of transportation infrastructure—Phase II*. Michigan Tech. https://digitalcommons.mtu.edu/michigantech-p/4

Coenen, T. B. J., & Golroo, A. (2017). A review on automated pavement distress detection methods. *Cogent Engineering*, *4*(1). https://doi.org/10.1080/23311916.2017.1374822

Dorsey, A. (2018). Using drones to monitor construction safety. *Laborers' Health & Safety Fund of North America*. https://www.lhsfna.org/using-drones-to-monitor-construction-safety-2/

DroneDeploy. (2018). *Drones raise the bar for roadway pavement inspection*. DroneDeploy's Blog. https://medium.com/aerial-acuity/drones-raise-the-bar-for-roadway-pavement-inspection-9c0079465772

Dye Management Group, Incorporated. (2014). *Monitoring highway assets with remote technology*. Michigan Department of Transportation. https://rosap.ntl.bts.gov/view/dot/27844

Guan, H., Li, J., Yu, Y., Chapman, M., Wang, H., Wang, C., & Zhai, R. (2015). Iterative tensor voting for pavement crack extraction using mobile laser scanning data. *IEEE Transactions on Geoscience and Remote Sensing*, *53*(3), 1527–1537. https://doi.org/10.1109/tgrs.2014.2344714

Henrickson, J. V., Rogers, C., Lu, H.-H., Valasek, J., & Shi, Y. (2016). Infrastructure assessment with small unmanned aircraft systems. *2016 International Conference on Unmanned Aircraft Systems (ICUAS)*, Arlington, VA, USA, 933-942. https://doi.org/10.1109/ICUAS.2016.7502652

Irizarry, J., & Johnson, E. N. (2019). *Field-test-based guideline development for the integration of unmanned aerial systems (UASs) in GDOT operations* (FHWA-GA-19-1609). Georgia Department of Transportation. https://g92018.eos-intl.net/eLibSQL14_G92018_Documents/16-09.pdf

Jagannath, M., Mitchell, A., Gustafson, J., Olsen, M.J., Parrish, C., Gillis, D., Kumpula, M., & Roe, G. (2018). *Effective use of geospatial tools in highway construction* (FHWA-HIF-19-089). U.S. Department of Transportation, Federal Highway Administration.

Jo, Y. & Ryu, S. (2015). Pothole detection system using a black-box camera. *Sensors*, *15*(11), 29316–29331. https://doi.org/10.3390/s151129316

Mathavan, S., Kamal, K., & Rahman, M. (2015). A review of three-dimensional imaging technologies for pavement distress detection and measurements. *IEEE Transactions on Intelligent Transportation Systems*, *16*(5), 2353–2362. https://doi.org/10.1109/tits.2015.2428655

Michael Baker International. (2017). *Michael Baker International pioneers drone activity at Hartsfield-Jackson Atlanta International Airport to gather runway improvement data* [Press release]. https://mbakerintl.com/press-release/michael-baker-international-pioneers-drone-activity-at-hartsfield-jackson-atlanta-international-airport-to-gather-runway-improvement-data

Millian, Julian D.R. (2019). *Towards the application of UAS for road maintenance at the Norvik Port* [Degree project, KTH Royal Institute of Technology School of Architecture and The Built Environment]. Digitala Vetenskapliga Arkivet. https://www.diva-portal.org/smash/get/diva2:1329881/FULLTEXT01.pdf

Mogawer, W. S., Xie, Y., Austerman, A. J., Dill, C., Jiang, L., & Gittings, J. E. (2019). *The application of unmanned aerial systems in surface transportation—Volume II-B: Assessment of roadway pavement condition with UAS*. Massachusetts Department of Transportation. https://www.mass.gov/doc/volume-2-task-b-assessment-of-roadway-pavement-condition-with-uas/download

Oliveira, H., & Correia, P. L. (2014). CrackIT—An image processing toolbox for crack detection and characterization. 2*014 IEEE International Conference on Image Processing (ICIP)*, Paris, France, pp. 798-802.. https://doi.org/10.1109/ICIP.2014.7025160

O'Neil-Dunne, J. P. M., & Estabrook, E. (2019). *The integration of unmanned aircraft systems to increase safety and decrease costs of transportation projects and related tasks* (FHWA-NH-RD-26962J). New Hampshire Department of Transportation. https://www.nh.gov/dot/org/projectdevelopment/materials/research/projects/documents/26962j-report.pdf

Pan, Y., Zhang, X., Cervone, G., & Yang, L. (2018). Detection of Asphalt Pavement Potholes and Cracks Based on the Unmanned Aerial Vehicle Multispectral Imagery. *IEEE Journal of Selected Topics in Applied Earth Observations and Remote Sensing*, *11*(10), 3701–3712. https://doi.org/10.1109/jstars.2018.2865528

Peraka, N. S. P. & Biligiri, K. P. (2020). Pavement asset management systems and technologies: A review. *Automation in Construction*, *119*, 103336. https://doi.org/10.1016/j.autcon.2020.103336

Petkova, M. (2016). *Deploying drones for autonomous detection of pavement distress* [Master's thesis, Michigan Institute of Technology]. Dspace.mit.edu; Massachusetts Institute of Technology. https://dspace.mit.edu/handle/1721.1/106049

Prather, C. D. (2019). *Current Landscape of Unmanned Aircraft Systems at Airports* (ACRP Synthesis 104). Transportation Research Board. https://doi.org/10.17226/25659

Propeller Aero. (2017). *What makes a good camera for drone surveys and inspections*. https://www.propelleraero.com/blog/what-makes-a-good-camera-for-drone-surveys-and-inspections/#:~:text=For%20drone%20inspections%20it%20is

Schnebele, E., Tanyu, B. F., Cervone, G., & Waters, N. (2015). Review of remote sensing methodologies for pavement management and assessment. *European Transport Research Review*, *7*(2). https://doi.org/10.1007/s12544-015-0156-6

Small Unmanned Aircraft Systems, 14 C.F.R. § 107 (2016). https://www.ecfr.gov/current/title-14/chapter-I/subchapter-F/part-107

Zakeri, H., Nejad, F. M., & Fahimifar, A. (2016). Image based techniques for crack detection, classification and quantification in asphalt pavement: A review. *Archives of Computational Methods in Engineering*, *24*, 935–977. https://doi.org/10.1007/s11831-016-9194-z

Zhang, C. (2008). An UAV-based photogrammetric mapping system for road condition assessment. *Proceedings of the 2008 International Society for Photogrammetry and Remote Sensing*. https://www.isprs.org/proceedings/XXXVII/congress/5_pdf/109.pdf

Zou, Q., Cao, Y., Li, Q., Mao, Q., & Wang, S. (2012). CrackTree: Automatic crack detection from pavement images. *Pattern Recognition Letters*, *33*(3), 227–238. https://doi.org/10.1016/j.patrec.2011.11.004

APPENDIX B—SITE VISIT: CAPE MAY COUNTY AIRPORT

Table B-1. Summary of the 2019 Pavement Condition Survey at Cape May County Airport.

Area	Location	Surface Type	Distress Code	Distress Description	Severity	2019 PCI	Comments
1A	Terminal Apron	PCC	63	Liner Cracking	L	58	
1A	Terminal Apron	PCC	66	Small Patching	L & M	58	
1A	Terminal Apron	PCC	67	Large Patching	L & M	58	
1A	Terminal Apron	PCC	71	Faulting	L, M, & H	58	
1A	Terminal Apron	PCC	73	Shrinkage Cracking	N/A	58	
1A	Terminal Apron	PCC	74	Joint Spalling	L & M	58	
1A	Terminal Apron	PCC	75	Corner Spalling	L & M	58	
1A	Terminal Apron	PCC	N/A	Replacement Slabs	N/A	58	
1A	Terminal Apron	PCC	63	Liner Cracking	L	58	
1A	Terminal Apron	PCC	66	Small Patching	L, M, & H	58	
1A	Terminal Apron	PCC	67	Large Patching	L & M	58	
1A	Terminal Apron	PCC	71	Faulting	L, M, & H	58	
1A	Terminal Apron	PCC	73	Shrinkage Cracking	N/A	58	
1A	Terminal Apron	PCC	74	Joint Spalling	L, M, & H	58	
1A	Terminal Apron	PCC	75	Corner Spalling	L, M, & H	58	
1A	Terminal Apron	PCC	N/A	Replacement Slabs	N/A	58	
1B	Taxiway G Apron	PCC	TBD	TBD	TBD	40	No Site Visit
2A	Runway 10/28	AC	48	L&T Cracking	L, M, & H	50	Old Crack Seal Applied

B-1

Area	Location	Surface Type	Distress Code	Distress Description	Severity	2019 PCI	Comments
2A	Runway 10/28	AC	57	Weathering	M	50	
2A	Runway 10/28	AC	48	L&T Cracking	L & M	71	Old Crack Seal Applied
2A	Runway 10/28	AC	57	Weathering	M	71	
2A	Runway 10/28	AC	43	Block Cracking	M	67	Old Crack Seal Applied
2A	Runway 10/28	AC	48	L&T Cracking	L & M	67	Old Crack Seal Applied
2A	Runway 10/28	AC	57	Weathering	M	67	
2B	Taxiway E	AC	41	Alligator Cracking	M	35	Old Crack Seal Applied
2B	Taxiway E	AC	48	L&T Cracking	L & M	35	Old Crack Seal Applied
2B	Taxiway E	AC	57	Weathering	M	35	
2C	Terminal Apron	AC	48	L&T Cracking	L & M	72	Crack Seal Applied
2C	Terminal Apron	AC	49	Oil Spillage	N/A	72	
2C	Terminal Apron	AC	52	Raveling	L	72	Old Surface Seal

AC = Asphalt concrete
L&T = Longitudinal and transverse
PCC = Portland cement concrete
N/A = Not applicable

L = Low severity
M = Medium severity
H = High severity
TBD = To be determined

APPENDIX C—DATA COLLECTION PARAMETERS FOR SMALL UNMANNED AIRCRAFT SYSTEMS

Table C-1. Stage 1 Data Collection Parameters for sUAS

Flight Number	Test Area	Airframe	Sensor	Data Type	Overlap (Forward / Side)	Altitude (ft)	GSD (mm)	Actual Flight Time (min)	Actual # Photos
1		M210	X7- 24mm	RGB	75/60	40.00	2	130	1,950
2		M210	X7-24mm	RGB	80/60	270.00	13.7	3	40
3		M210	X7- 16mm	RGB	80/60	344.14	25.4	1	7
4		M210	XT2- 13mm	Thermal	80/50	63.57	25.4	16	756
5		M210	X5s	RGB	74/60	30.00	2	150	2,162
6		M210	X5s	RGB	80/60	206.92	13.7	14	52
7		M210	X5s	RGB	80/60	383.85	25.4	9	14
~~8~~		~~eBee~~	~~S.O.D.A. 3D~~	~~RGB~~	~~80/60~~	~~198.80~~	~~13.7~~	~~0~~	~~0~~
~~9~~	1A	~~eBee~~	~~S.O.D.A. 3D~~	~~RGB~~	~~80/60~~	~~368.10~~	~~25.4~~	~~0~~	~~0~~
10		M2P	Mavic 2 Pro	RGB	74/60	30.37	2	130	2,111
11		M2P	Mavic 2 Pro	RGB	80/60	200.74	13.7	3	35
12		M2P	Mavic 2 Pro	RGB	80/60	371.11	25.4	2	13
~~13~~		~~M2ED~~	~~Mavic 2 Enterprise Dual~~	~~RGB~~	~~80/60~~	~~19.05~~	~~2~~	~~0~~	~~0~~
14		M2ED	Mavic 2 Enterprise Dual	RGB	80/60	128.57	13.7	6	116
15		M2ED	Mavic 2 Enterprise Dual	RGB	80/60	238.10	25.4	2	34
16		M210	X7- 24mm	RGB	75/60	40.00	2	35	480
17		M210	X7- 24mm	RGB	80/60	270.00	13.7	1	7
18		M210	X7- 16mm	RGB	80/60	344.14	25.4	0.5	4
19	2C	M210	XT2- 13mm	Thermal	80/50	63.57	25.4	5	166
20		M210	X5S	RGB	74/60	30.00	2	40	448
21		M210	X5S	RGB	80/60	206.92	13.7	1	14
22		M210	X5S	RGB	80/60	383.85	25.4	0.5	5

C-1

Flight Number	Test Area	Airframe	Sensor	Data Type	Overlap (Forward / Side)	Altitude (ft)	GSD (mm)	Actual Flight Time (min)	Actual # Photos
~~23~~		~~eBee~~	~~S.O.D.A. 3D~~	~~RGB~~	~~80/60~~	~~198.80~~	~~13.7~~	~~0~~	~~0~~
~~24~~		~~eBee~~	~~S.O.D.A. 3D~~	~~RGB~~	~~80/60~~	~~368.10~~	~~25.4~~	~~0~~	~~0~~
25	2C	M2P	M2P	RGB	74/60	30.37	2	32	486
26		M2P	M2P	RGB	80/60	200.74	13.7	0.75	6
27		M2P	M2P	RGB	80/60	371.11	25.4	0.5	4
~~28~~		~~M2ED~~	~~M2ED~~	~~RGB~~	~~80/60~~	~~19.05~~	~~2~~	~~0~~	~~0~~
29		M2ED	M2ED	RGB	80/60	128.57	13.7	2	33
30		M2ED	M2ED	RGB	80/60	238.10	25.4	0.5	5
							Total Flight Time	584.75	

Table C-2. Stage 2 Data Collection Parameters for sUAS

Flight Number	Test Area	Airframe	Sensor	Data Type	Overlap (Forward / Side)	Altitude (ft)	GSD (mm)	Actual Flight Time (min)	Actual # Photos
31		M210	X7- 24mm	RGB	80/60	97.04	4.9	10	166
32		M210	X7- 24mm	RGB	80/60	158.33	7.9	5	59
33		M210	X7- 24mm	RGB	80/60	214.51	10.8	3	33
34		M210	X5s	RGB	80/60	71.66	4.9	10	217
35	2C	M210	X5s	RGB	80/60	116.91	7.9	5	74
36		M210	X5s	RGB	80/60	158.40	10.8	3	44
37		M2P	Mavic 2 Pro	RGB	80/60	70.79	4.9	10	198
38		M2P	Mavic 2 Pro	RGB	80/60	115.50	7.9	5	76
39		M2P	Mavic 2 Pro	RGB	80/60	156.48	10.8	3	34
40		M210	X7- 35mm	RGB	75/60	59.59	2.0	35	780
41		M210	X7- 24mm	RGB	80/60	97.04	4.9	10	154
42	2B	M210	X7- 24mm	RGB	80/60	158.33	7.9	5	63
43		M210	X7 24mm	RGB	80/60	214.51	10.8	3	35
44		M210	X7 24mm	RGB	80/60	275.80	13.7	2	19

Flight Number	Test Area	Airframe	Sensor	Data Type	Overlap (Forward / Side)	Altitude (ft)	GSD (mm)	Actual Flight Time (min)	Actual # Photos
45	2B	M210	X5s	RGB	75/60	30.17	2.0	40	892
46		M210	X5s	RGB	80/60	71.66	4.9	10	183
47		M210	X5s	RGB	80/60	116.91	7.9	5	64
48		M210	X5s	RGB	80/60	158.40	10.8	3	36
49		M210	X5s	RGB	80/60	203.66	13.7	2	19
50		M2P	M2P	RGB	74/60	29.81	2.0	35	812
51		M2P	M2P	RGB	80/60	70.79	4.9	10	188
52		M2P	M2P	RGB	80/60	115.50	7.9	5	66
53		M2P	M2P	RGB	80/60	156.48	10.8	3	37
54		M2P	M2P	RGB	80/60	201.19	13.7	2	19
55		eBee	S.O.D.A. 3D	RGB	80/60	198.8	13.7	5	35
56	2A	M210	X7- 35mm	RGB	75/60	59.59	2.0	85	2,025
57		M210	X7- 24mm	RGB	80/60	97.04	4.9	20	427
58		M210	X7- 24mm	RGB	80/60	158.33	7.9	8	175
59		M210	X7- 24mm	RGB	80/60	214.51	10.8	4	79
60		M210	X7- 24mm	RGB	80/60	275.80	13.7	3	50
61		M210	X5s	RGB	75/60	30.17	2.0	101	2,392
62		M210	X5s	RGB	80/60	71.66	4.9	22	506
63		M210	X5s	RGB	80/60	116.91	7.9	8	177
64		M210	X5s	RGB	80/60	158.40	10.8	5	98
65		M210	X5s	RGB	80/60	203.66	13.7	3	51
66		M2P	M2P	RGB	74/60	29.81	2.0	94	2,168
67		M2P	M2P	RGB	80/60	70.79	4.9	20	446
68		M2P	M2P	RGB	80/60	115.50	7.9	9	182
69		M2P	M2P	RGB	80/60	156.48	10.8	5	101
70		M2P	M2P	RGB	80/60	201.19	13.7	3	53
71		eBee	S.O.D.A. 3D	RGB	80/60	198.80	13.7	6	135
72		M210	X7- 35mm	RGB	75/60	59.59	2.0	50	1,013
73*	1B	M210	X7- 24mm	RGB	80/60	97.04	4.9	11	208

Flight Number	Test Area	Airframe	Sensor	Data Type	Overlap (Forward / Side)	Altitude (ft)	GSD (mm)	Actual Flight Time (min)	Actual # Photos
73FXD**		M210	X7- 24mm	RGB	80/60	97.04	4.9	11	208
74		M210	X7- 24mm	RGB	80/60	158.33	7.9	5	73
75		M210	X7 24mm	RGB	80/60	214.51	10.8	3	41
76		M210	X7- 24mm	RGB	80/60	275.80	13.7	2	21
77		M210	X5s	RGB	75/60	30.17	2.0	0	0
78		M210	X5s	RGB	80/60	71.66	4.9	12	271
79	1B	M210	X5s	RGB	80/60	116.91	7.9	5	93
80		M210	X5s	RGB	80/60	158.40	10.8	4	55
81		M210	X5s	RGB	80/60	203.66	13.7	2	32
82		M2P	M2P	RGB	74/60	29.81	2.0	0	0
83		M2P	M2P	RGB	80/60	70.79	4.9	12	248
84		M2P	M2P	RGB	80/60	115.50	7.9	6	95
85		M2P	M2P	RGB	80/60	156.48	10.8	3	42
86		M2P	M2P	RGB	80/60	201.19	13.7	2	22
87		eBee	S.O.D.A. 3D	RGB	80/60	198.80	13.7	0	0
						Total Flight Time		753	

RGB = Red, green, blue

*Note: Two data sets were collected for Flight #73. *Shutter Priority Mode vs **Manual Mode. Shutter Priority Mode had contrast variance; Manual Mode resulted in extremely dark areas in shaded regions.*